Graphene based Nanocomposites for Mechanical Reinforcement

A THESIS SUBMITED TO THE UNIVERSITY OF LONDON FOR THE DEGREE OF DOCTOR OF PHILOSOPHY

January 2015

By

Charline Sellam

School of Engineering and Materials Science

Queen Mary University of London

Mile End Road, London E1 4NS

Statement of originality

I, Charline Sellam, confirm that the research included within this thesis is my own work or that where it has been carried out in collaboration with, or supported by others, that this is duly acknowledged below and my contribution indicated. Previously published material is also acknowledged below.

I attest that I have exercised reasonable care to ensure that the work is original, and does not to the best of my knowledge break any UK law, infringe any third party's copyright or other Intellectual Property Right, or contain any confidential material.

I accept that the College has the right to use plagiarism detection software to check the electronic version of the thesis.

I confirm that this thesis has not been previously submitted for the award of a degree by this or any other university.

The copyright of this thesis rests with the author and no quotation from it or information derived from it may be published without the prior written consent of the author.

Signature:

Date: 23/12/14

Details of collaboration:

Sellam, Charline, Zhi Zhai, Hediyeh Zahabi, Hua Deng, Emiliano Bilotti, and Ton Peijs, *Bioinspired Layer-by-Layer Poly(vinyl alcohol) - Graphene Oxide Nanocomposites.* MRS Online Proceedings Library, 2012. **1410**:

Acknowledgment

I would like to thank all the people who helped me all along my PhD. First, I would like to thanks Ton Peijs for giving me the opportunity to carry out this PhD. He was very helpful and supportive throughout the years. I would like to thank all my friends and colleges from SEMS and Nanoforce with a very special thanks to Olivier Picot, Nanayaa Bates, Zhipeng Gao, Amin Rezaienia, Emiliano Bilotti, Urszula Stachewicz and Sanam Ghaffari. Also I would like to thank some of the Master students I worked with Zhi Zhai and Hediyeh Zahabi.

I would also like to thank Krystelle Mafina, Zophia Luklinska and Rory Wilson for their expertise. I would like to thank all the technicians who helped me, with special thanks for Mike, Dougie Thomson and Chris Mole. I would like to thank Jim Kirkland, for his help and for all the coffees he offered me to cheer me up during the long days.

I would like to thank the staff in the School of Engineering and Materials as well as Nanoforce Technology Ltd. for use of their facilities. I thank the Dutch Polymer Institute for the financial support through the project #648.

Finally I would like to thank my partner and college Olivier Picot for always being supportive, helping me through the difficulties, and being patient. I also thank my lovely parents, my brother, Barbara, Pierrick and Julien for always being positive and supportive. I also thank my friends, Bullette and Ghislo. My special thank is for my son Lucas, to be such an adorable and cheerful baby.

Abstract

In this work the potential of graphene-like particles for mechanical reinforcement is investigated. Different polymer processing methods are studied from traditional ones to more advanced techniques. The potential of graphene as a reinforcement for polymer composites is addressed as a result of polymer modifications and the morphology of the graphene like particles.

First, a composites of polycarbonate (PC) and graphite nanoplatelets (GNP) are produced by a traditional melt-mixing method. The GNP composites present a low mechanical reinforcing efficiency which is believed to be due to a poor dispersion of the GNP and a weak interaction between the GNP and the matrix.

Secondly, solution cast composites of polyvinyl alcohol (PVA) with very low loadings of graphene oxide (GO) are produced. The polymer morphology undergoes some modifications after the addition of GO. A strong increase of the *Tg* is observed after the addition of GO which is the result of a reduction in polymer mobility, while a dramatic increase of the mechanical properties is seen as well. Uni-axial drawing is applied in order to align the particles. No polymer modifications are observed between the drawn PVA and the drawn nanocomposites due to the strong alignment of the polymer chains during the drawing. Mechanical reinforcement is observed after addition of the GO showing real reinforcement.

Finally, a more advanced processing method is investigated using spraying. The condition of spraying a layer of polymer and GO is studied. Finally a hierarchical composite of PVA - GO is produced by this spraying method. 150 bi-layers are deposited to create a film with improved mechanical properties at a loading of 5.4 wt.% GO. The Young's modulus and strength of these films doubled or nearly doubled which is believed to be due to the high level of structural organization of the layered nanocomposite incorporating the 2D GO nanofiller, together with hydrogen bonding between the PVA and the GO sheets.

Table of contents

List of figures

List of tables

List of acronyms

AFM	Atomic Force Microscopy
CNT	Carbon nanotube
CVD	Chemical Vapour Deposition
DMA	Dynamic Mechanical Analysis
DSC	Differential Scanning Calorimetry
E	Young'sModulus
GNP	Graphite nanoplatelets
GNR	Graphene nanoribbons
GO	Graphene oxide
HDPE	High density polyethylene
LbL	Layer-by-layer
LDPE	Low density polyethylene
MWNT	Multi wall carbon nanotube
PC	Polycarbonate
PMMA	Poly(methyl methacrylate)
PS	Polystyrene
PVA	Poly(vinyl alcohol)
PEG	Polyethylene glycol
SANS	Small-angle neutron scattering
SEM	Scanning electron microscopy
SWNT	Single wall carbon nanotube
TEM	Transmission electron microscopy
Tg	Glass transition temperature
TGA	Thermal Gravimetric Analysis
TRG	Thermally reduced graphene
WAXD	Wide angle Xray diffraction
X_c	Crystallinity

Chapter 1

General introduction

1.1. Graphene, carbon in two dimensions

Introduced by traditional newspapers as a “miracle material” [1, 2] or a “super-material” [3], graphene harbours the hope of a promising future. It is an atomically flat layer of carbon 0.34 nm thick. Its two dimensional (2D) structure has a honeycomb arrangement which is the “building block” for graphitic material [4]. When it is a sphere, it forms zero dimensional fullerenes. But rolled up, it forms a one dimensional SWNT. And if it is stacked, it forms a three dimensional graphite as presented in Figure 1.1.

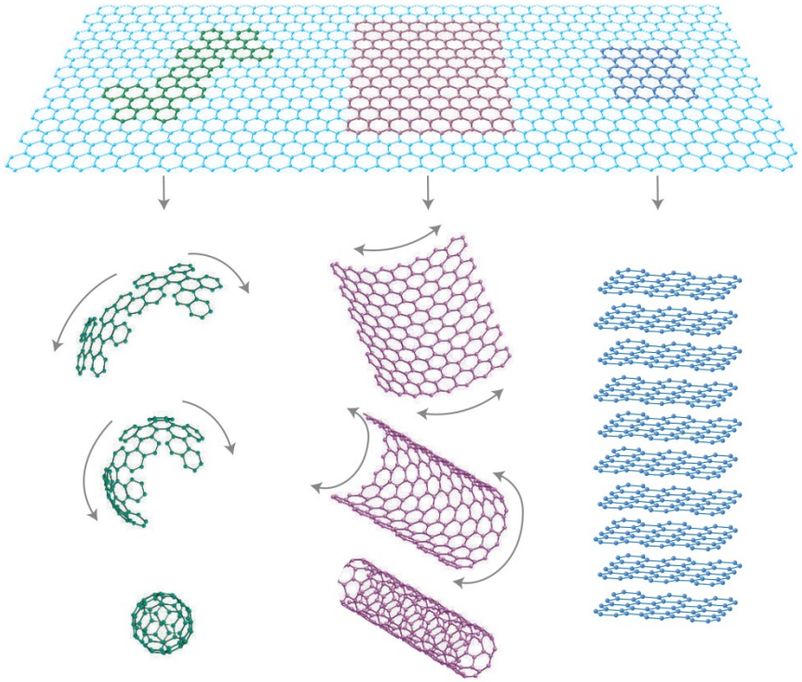

Figure 1.1: 2D graphene: wrapped to form 0D fullerene, rolled up to form a 1D single wall nanotube and stacked to form a 3D graphite [4].

In 2004, the first graphene sheet is isolated by Novoselov et al. [5] using a simple method called “scotch tape method”. This discovery allowed the intrinsic properties of the 2D crystal to be studied and led to the Nobel Prize of Physics six years later for Andre Geim and Kostya Novoselov.

This monolayer of carbon atoms, which forms a crystalline, flat, atomically thin, honeycomb lattice gives it remarkable properties [4, 6-8]. Graphene sheet is transparent [9] and has high mechanical properties; it presents a high modulus comparable to SWNT (1 TPa) and a high strength (130 GPa [10]). It has a high carrier mobility (15,000 $cm^2.V^{-1}.s^{-1}$ [5]). Graphene shows a high thermal conductivity (3.10^3 – $5.\ 10^3$ W/mK) [11] and is impermeable to standard gases, including helium [12]. All of these properties make graphene a promising filler for

multifunctional polymer composite applications. The field of application is wide, from electronic to energy through nanocomposites. To demonstrate its potential, the European Union is investing 1 billion Euros between 2013 and 2023. Also, the UK has allocated a budget of £50 million for graphene to include £ 22 million for commercialisation of graphene [3]. The number of research papers about graphene increased by a factor of 56 between 2004 and 2013 to reach more than 9 000 publications, based on Web of Knowledge. Also major multinational corporations like Samsung, BASF and Head are developing new products using graphene such as mobile devices, conductive ink and tennis rackets, respectively. To highlight the interest in graphene, the number of patents has more than tripled between 2010 and 2012 to reach a total of over 8 000 published patent applications by February 2013 [13].

The rapid growth of graphene research in academic as well as in industry shows the theoretical potential of graphene and suggests it has an optimistic economical perspective. Based on this fast development, we can expect to see graphene in consumer products soon.

1.2. Nanocomposites

The combination of two materials, a filler and a matrix, to obtain a material with superior properties is called a composite. The term “nanocomposite” is more recent and indicates that the filler has at least one of its dimensions below 100 nm. Although we have known about composites for centuries, the era of composites really started during the 1940’s with the development of the polymer industries. The first industrial composite is made of glass fibre in a polymer matrix. The glass fibres

reinforced the plastic matrix by stiffening it, so producing a strong but lightweight structure. Used first for defence applications, nowadays nanocomposites are everywhere in our daily life. From our car to the packaging of a smartphone, nanocomposites have been developed for very different applications. Nanocomposites are based on nanomaterials with very unique properties which give them the advantage of being lightweight and easily adjustable. Until recently, research very much focused on the dispersion of the nanofillers in the polymer matrix. Dispersion is key in nanocomposite research because good dispersion is necessary for nanocomposites with superior properties, while on the other hand, bad dispersion often dramatically weakens nanocomposites. Although nowadays the dispersion of the nanofiller is better understood and controlled often nanocomposites still show weak reinforcement and exhibit disappointing properties compared to what might be expected according to theory. To fully understand the potential of nanocomposites it is interesting to look at nanocomposites in nature. Indeed, Nature uses composites including nanocomposites for various purposes, from the protection of vital organisms (bones, nacre), as defence (antler), as a mean of support (trunk supports the tree) or even to catch prey (spider silk, teeth). Based on a few components including calcium phosphate, carbonates, collagen, protein, etc., biological composites differ greatly depending on the composition, the organisation of the meso, micro and nanostructure leading to a fine-tuning of the mechanical properties and the extraordinary reinforcement ability [14]. It is very interesting to note for example, that in the case of nacre, the nanocomposite (the shell) has a fracture toughness 3-9 times and a strength 3-6 times greater than the mineral itself [15-16]. The main features are: (i) nanosize particles, (ii) a bottom-up approach to

build up the composites, (iii) a highly mineralised composite and (iv) a high degree of organisation.

Antler, for instance, is a hierarchical composite as presented in Figure 1.2. It is one of the most impact resistant and energy absorbent composites. It is characterised by a highly mineralised composites with an outer layer called compact bone and an inner core called trabecular bone. The inner core is porous and anisotropic. The channels are aligned along the antler beam. On the other hand the compact bone consists of osteons. These osteons are made from concentric rings, which are made of aligned fibres with the alignment being different for each ring. Finally, each fibre is composed of collagen fibrils made of nanosize protein (tropocollagen) and mineral (hydroxypatite) [17].

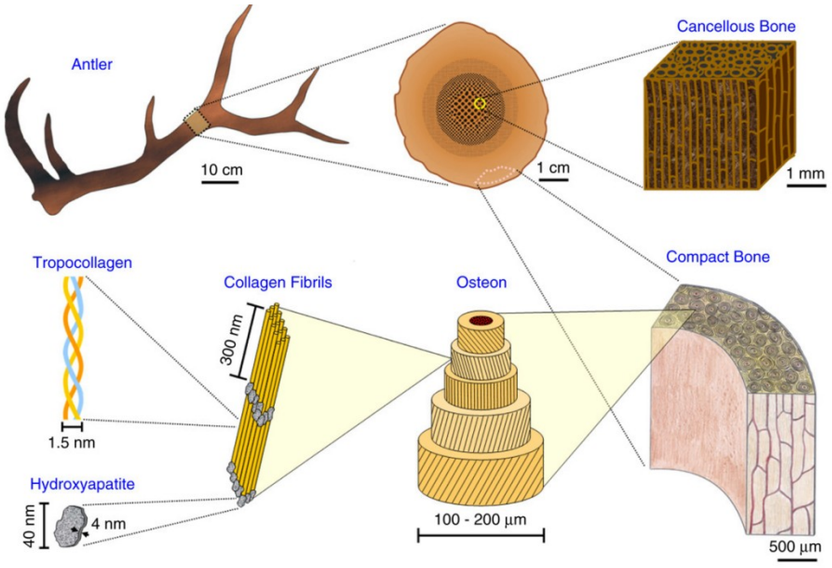

Figure 1.2: Hierarchical structure of antler from nanoscale to macroscale. The antler is composed of an outler layer (compact bone) and an inside core called trabecullar (cancellous) bone [16].

1.3. Outline of this thesis

The potential of graphene is undisputable by all its intrinsic qualities. Another advantage of graphene is that it opens the doors to a new era of atomically thin materials, and other materials in two dimensions such as boron nitride.

Based on one dimension filler, it is well known that the morphology of particles in nanocomposites can be dramatically modified by polymer processing [18]. It is important to understand the effect of processing on the morphology of graphene, and in a broader sense on atomically thin 2D particles in general, in order to optimise nanocomposites properties.

In this thesis, the mechanical reinforcement of graphene-like particles into a polymer matrix is studied as a result of processing and the effect on the morphology of these nanoplatelets. Several processing methods were studied, from traditional such as melt mixing to more advanced techniques such as layer-by-layer (LbL), but also post processing methods like uni-axial drawing, in order to get a better understanding of the effect of processing on 2D graphene-like particles.

In Chapter 2, graphene and the methods of productions are discussed. It then focuses on works based on graphene nanocomposites, highlighting the potential and the challenges of graphene when used in a polymer matrix.

Chapter 3 introduces the means to optimise the mechanical reinforcement of graphene nanocomposites. Some mechanical models are described, followed by important elements to take into consideration when introducing graphene into polymeric matrices.

In Chapters 4 and 5, traditional processing methods like melt mixing and solution casting are used to create graphene nanocomposites. Chapter 4 investigates the potential of multi-layered graphene or so-called "graphite nanoplatelets" (GNP) melt mixed in polycarbonate. Here GNP is preferred compared to graphene as they are produced mass production and more suitable for melt-compounding. In Chapter 5, solution casting as a processing method is investigated for a system based on PVA and GO.

In Chapter 6, a post-processing step involving solid state drawing is applied on these solution cast PVA-GO nanocomposites in order to improve the level of organization through the alignment of GO in these materials.

In Chapter 7, the morphology of layered nanocomposites obtained by spraying is discussed. Spraying is a recent and less traditional process for the creation of layered nanocomposites with finely controlled microstructures. This chapter provides the background for the next chapter, as it enables us to define the parameters which form the layer-by-layer PVA-GO described in the next chapter. Finally a hierarchical nanocomposite of layer-by-layer PVA-GO is obtained by finely controlling each layer (Chapter 8).

In Chapter 4 to Chapter 8, nanocomposites are produced using different methods. The mechanical reinforcement of these nanocomposites is studied and addressed depending on the polymer modifications, the nanofiller orientation and the morphology of the platelets.

1.4. References

1. H.d. Quetteville, in *The Telegraph*. 10 Jun 2013.
2. S. Blendis, CNN, 6 October 2013.
3. A. Jha, in *The Guardian*. 27 December 2012.
4. A.K. Geim and K.S. Novoselov, Nature Materials, 2007. **6**(3): p. 183-191.
5. K.S. Novoselov, A.K. Geim, S.V. Morozov, D. Jiang, Y. Zhang, S.V. Dubonos, I.V. Grigorieva, and A.A. Firsov, Science, 2004. **306**(5696): p. 666-669.
6. M.I. Katsnelson, Materials Today. **10**(1-2): p. 20-27.
7. A.K. Geim, Science, 2009. **324**(5934): p. 1530-1534.
8. Y.H. Wu, T. Yu, and Z.X. Shen, Journal of Applied Physics, 2010. **108**(7): p. 071301.
9. R.R. Nair, P. Blake, A.N. Grigorenko, K.S. Novoselov, T.J. Booth, T. Stauber, N.M.R. Peres, and A.K. Geim, Science, 2008. **320**(5881): p. 1308-1308.
10. C. Lee, X. Wei, J.W. Kysar, and J. Hone, Science, 2008. **321**(5887): p. 385-388.
11. A.A. Balandin, S. Ghosh, W. Bao, I. Calizo, D. Teweldebrhan, F. Miao, and C.N. Lau, Nano Letters, 2008. **8**(3): p. 902-907.
12. J.S. Bunch, S.S. Verbridge, J.S. Alden, A.M. van der Zande, J.M. Parpia, H.G. Craighead, and P.L. McEuen, Nano Letters, 2008. **8**(8): p. 2458-2462.
13. . March 2013, The Intellectual Property Office
14. R. Wang and H.S. Gupta, Annual Review of Materials Research, 2011. **41**(1): p. 41-73.
15. B. Ji and H. Gao, Journal of the Mechanics and Physics of Solids, 2004. **52**(9): p. 1963-1990.
16. J. Sun and B. Bhushan, RSC Advances, 2012. **2**(20): p. 7617-7632.
17. P.Y. Chen, A.Y.M. Lin, Y.S. Lin, Y. Seki, A.G. Stokes, J. Peyras, E.A. Olevsky, M.A. Meyers, and J. McKittrick, Journal of the Mechanical Behavior of Biomedical Materials, 2008. **1**(3): p. 208-226.
18. H. Deng, E. Bilotti, R. Zhang, J. Loos, and T. Peijs, Synthetic Metals, 2010. **160**(5-6): p. 337-344.

Chapter 2

2.1. Graphene based nanocomposites

2.2. Introduction

In the mid 1980s, the formation of cluster by laser vaporisation of carbon lead to the formation of carbon clusters C_n in which the number of carbon atoms is lower than a few hundred [1], which led to the discovery of fullerene [2]. Fullerene is a stable zero dimensional (0D) carbon cage composed of hexagonal and pentagonal faces in which the structure depends on the number of carbon atoms [3]. Ten years later, CNT are "re-discovered" [4, 5], followed by the synthesis of single wall nanotube [6, 7], a one dimensional (1D) carbon filler consisting of a graphene sheet rolled up into a cylinder. These CNTs present exceptional properties such as mechanical strength and stiffness, and electrical transport properties, which makes them a very promising filler for composites as reviewed by Thostenson et al. [8]. Almost 10 years later, in

2004, two dimensional (2D) graphene sheet is isolated by Novoselov et al. [9] via mechanical cleavage.

This monolayer of carbon atoms, which forms a flat, atomically thin, two dimensional honeycomb lattice has similar to CNTs also interesting physical and electrical properties which were intensively studied and reviewed in several articles [10-13]. Graphene sheet is transparent [14]. It has high mechanical [15], thermal [16] and electrical [9] properties, and it is also impermeable to standard gases, including helium [17]. All of these properties make graphene a promising filler for multifunctional nanocomposites. It can be used in a wide range of applications from use as a reinforcing agent in nanocomposites [18-20] to solar cells including sensors [21-24] and flexible displays [25, 26]. The enthusiasm for graphene and in this case graphene nanocomposite can be observed by the exponential increasing in research activity in this area as presented in

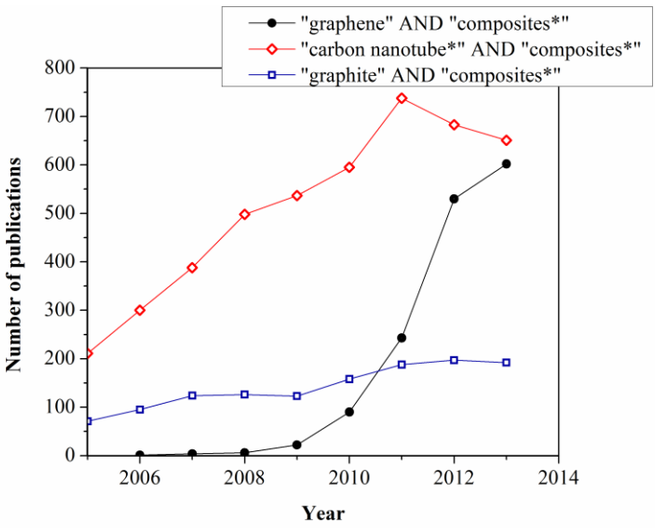

Figure 2.1: Number of citations per year of “graphene” AND “composite*”, “carbon nanotube*” AND “composite*” and “graphite” AND “composite*" as keywords in title in ISI Web of knowledge.

2.3. Graphene

Graphene is a two dimensional atomic crystal. Atomically thin, the structure is organised in a planar honeycomb structured stack in AB sequence as described in Figure 2.2 and reviewed in [27, 28]. Graphene is highly flexible due to its sp^2 hybridisation, which bonds the carbon atoms to each other. It has a lamellar structure linked by weak van der Waals interactions with an interatomic distance "*d*-spacing" of 3.35 Å. The reported thickness of graphene ranges from 0.35 nm to 1 nm depending on characterisation method [29].

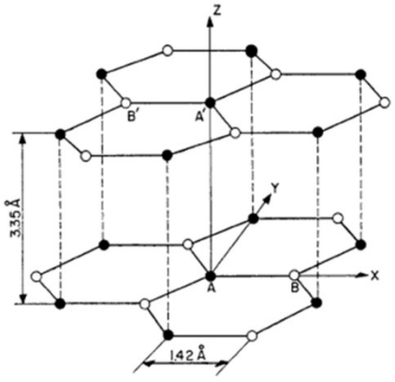

Figure 2.2: The crystal structure of graphite. The primitive unit cell is hexagonal, with dimensions a = 2.46 Å and c = 6.71 Å [27].

Different methods have been developed to characterise graphene and to obtain graphite platelets in bulk quantities through colloidal suspensions [30] or by thermal expansion [31]. Recent developments in this area have been reviewed in [32, 33]. Depending on the process, the obtained 2D carbon range from a single layer to a few stacked layers with a wide range of diameters. Although graphene is strictly a monolayer of carbon, a wide variety of two dimensional carbons can be defined in

function of their thickness and their chemical structure. A different nomenclature is important for each 2D carbons as their properties, especially electronic, can strongly differ. The editorial team of Carbon has developed a nomenclature [34] and some are summarised in Table 2.1. For example, graphene oxide microsheets will be preferred to describe monolayers of graphene oxide with a lateral size of more than 100 nm.

Table 2.1: Nomenclature of 2D carbon sheets [34].

	Chemical structure	**Thickness**	**Lateral dimensions**
Graphene layer	Hexagonal organisation of sp^2 bonded carbons	Single atom thick sheet	From several nanometers to macroscale
Bilayer graphene, trilayer graphene	Stacked graphene	2 or 3 well defined layers	Extended lateral dimension
Few layers of graphene (FLG)	Stacked graphene	From 2 to about 5 well defined layers	Extended lateral dimension
Multilayers of graphene	Stacked graphene	From 2 to about 5 well defined layers	Extended lateral dimension
GNP / nanosheets / nanoflakes	2D graphite material	< 100 nm	< 100 nm
Graphene nanosheet	Graphene layer	Single atom thick sheet	< 100 nm
Graphene microsheet	Graphene layer	Single atom thick sheet	From 100 nm to 100 µm
Graphene oxide	Chemically modified graphene by oxidation of the basal plane	Single layer	Extended lateral dimension
Reduced graphene oxide	Graphene oxide which has been reduced	Single layer	Extended lateral dimension

2.4. Production methods of graphene

Mechanical exfoliation is the most well-known processing method to obtain a monolayer of graphene. It is the method that Novoselov et al. [9] originally used to isolate the first layer of graphene which ultimately lead to the Nobel prize in Physics for Geim & Novoselov in 2010. The process consists of peeling repeatedly pyrolytic graphite apart using sticky tape and to deposit the flakes from the sticky tape on a substrate. The obtained substrate is then covered by several multilayers of graphene and hopefully a few monolayers. To help distinguishing the monolayer, a Si/SiO_2 wafer is often used as a substrate to obtain the best optical contrast, although graphene can also be seen on any arbitrary substrate [35]. Freely suspended graphene obtained with this method is not perfectly flat [36] but presents random microscopic ondulations [37]. Due to the high quality of the graphene isolated, this process is mainly used for fundamental studies as well as model studies on the behaviour of a single layer of graphene embedded in a polymer matrix.

The exfoliation of graphene by sonication and centrifugation of graphite is a way to produce non-oxidised and non-functionalised graphene in bulk quantity. The choice of the solvent is crucial in this process. According to Hernandez et al. [38] the exfoliation of the sheets is possible when the surface energy of the solvent matches with the surface energy of the graphene. The exfoliation of graphene has been demonstrated in solvents [38-40], in surfactant solutions [41, 42], in aqueous polymer solutions [43] and at the interphase of two immiscible solvents [44]. For example, by sonicating graphite in a water/sodium dodecylbenzene sulfonate (surfactant) solution, Lotya et al. [42] obtained flakes of which ~43 % are below 5 layers and ~3 % as monolayers.

The formation of monolayers of graphene with extremely high aspect ratio is also possible via epitaxial growth and by CVD. Epitaxial growth of graphene can be produced by vacuum graphitisation of silicon carbide which typically results in several layers of graphene [45, 46]. The growth of graphene on metals by CVD of hydrocarbon gases has also been reported. On nickel films [47-49], the graphene grows by segregation and will consist of multiple layers. On copper film, graphene grows by a surface-catalyzed process [50]. It gives a monolayer which is polycrystalline with different orientations of the grains [51] and covers more than 95 % of the surface [50]. Graphene growth on Ruthenium has been observed and consists of a mono-layer or bi-layers on a large area [52]. Recent work on annealing a sacrificial nickel thin film on a SiO_2/Si wafer [53] at low temperature resulted in a minimum of 75 % of monolayers. It also suggested that the formation of graphene can be obtained with unintentionally introduced carbon i.e. from the carbon-containing compounds. Usually, the graphene is released by etching the substrate and transferring it onto another substrate. The preferential method to transfer graphene is usually by polymer stamping [49, 54]. A direct transfer is also possible by interaction between amorphous carbon and graphene [55]. The potential of graphene synthesis in large quantities and its easy transfer leads to the potential of large, flexible, and transparent electrodes using LbL nanocomposites for electronic applications [56] as presented in Figure 2.3.

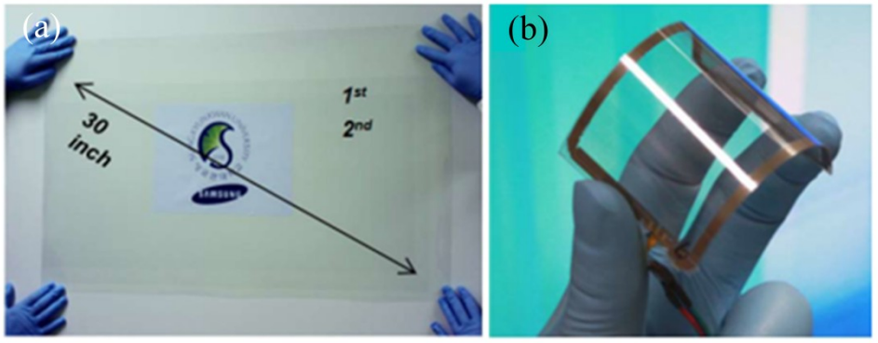

Figure 2.3: (a) A transparent ultra large area graphene made from CVD method transferred on a 35-inch PET sheet; (b) an assembled PET-graphene touch panel showing outstanding flexibility [56].

It is also possible to obtain graphene nanoribbons; the main advantage here is to have a better control on the size of the sheet (i.e. the diameter and length). GNR have been obtained by unzipping MWNTs by Ar plasma etching method [57] or by oxidation [58]. Other means of producing GNR are by lithography [59], chemical routes [60-62] and sonication [63]. However, to the best of the authors' knowledge, GNR has not been used so far in nanocomposites which can be explained by the complex processing and the very low aspect ratio of the obtained platelets.

Until now oxidation of graphite, followed by in-situ reduction is the main process to obtain graphene in bulk quantity. Graphene oxide (GO) is one of the oldest and the most studied graphite intercalated compounds (GIC). The formation of GIC is possible due to the insertion of an atomic layer or molecular layer (called intercalent) between the graphene layers (called host). The mechanism of intercalation is reviewed in several articles [64-66]. The process of intercalation is recognised to be accompanied by a charge-transfer between the intercalated compound and the graphene layers. GIC can be donor-type or acceptor-type, depending on the direction

of electron transfer. GIC is prepared either by chemical or electrochemical routes. The intercalation leads to an extension of the *d*-spacing (d_0). The increase of the distance of neighbouring graphene layers to individual values (d_1) is determined by the size of the guest. The guests accommodated within the interlayer spacing of graphite are called intercalates. The GIC is thus composed of carbon layers and intercalated layers. The degree of intercalation is called a stage. For example, a stage 2 would be two layers of carbon for one intercalated layer, as presented in Figure 2.4.

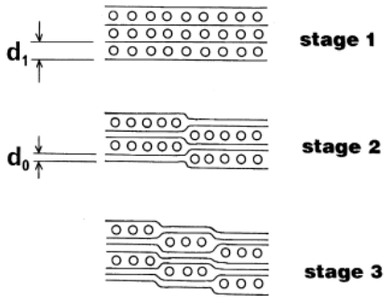

Figure 2.4: Stage 1, 2 and 3 GICs in the pleated layer model or Daumas–Herold domain model: (–) graphene layer; (•) intercalated layer [65].

The main oxidising methods are Brodie [67], Staudenmaier [68] and Hummers-Offeman [69] methods which imply the use of strong acids and oxidising agents. In the case of GO, the intercalated agent is bonded to the surface leading to break out of the sp^2 orbital in sp^3 orbital [27]. The expansion of the GO and the amount of sp^3 is related to the oxidation treatment time [70, 71]. As the oxidation occurs, the interplanar space and the BET surface areas increase as does the oxygen content until saturation at C/O ~0.47 [72]. Li et al. [73] have proposed a model of the oxidation mechanism based on the formation of epoxy groups. The structure of the GO is still not very well understood and has been discussed in several models [74-

80] and reviewed by Dreyer et al. [81]. The structure of graphene oxide is viewed as a single layer with both graphitic areas and functionalised areas with hydroxyl and epoxide groups on the surface and carboxyl and carbonyl groups on the edges [82]. The thickness of one layer GO due to its functionalised group measured with AFM is 1.6 nm and the roughness of the GO around 0.6 nm, which is assumed to be due to the oxygen bonds (sp^3 orbitals) and the ondulation from lattice distortion [83]. The aspect ratio of the GO is tuneable by modifying the reaction time and oxidants [84]. Both oxidation methods as well as the structure of GO have been reviewed in more detail in [81, 85].

A reduction step allows recovering the sp^2 hybridation; and there are two main ways to reduce graphite oxide. The first method is chemical reduction (CRG) and the other is by thermal reduction (TRG). According to the chemical structure and the intrinsic conductivity of chemically and thermally reduced GO, the thermal reduction is found more effective [86]. Besides the above method, other methods of reduction such as by photothermal heating [87], solvothermal reduction [88] exist and have been reviewed [85, 89].

Chemical methods lead to a reduction of the GO in solution and have been reviewed by Park et al [90]. Several ways to reduce GO have been studied, most of them involving mixing with hydrazine [91], hydroquinone [92, 93], dimethylhydrazine [30], sodium borohydride [93], or sodium hydrosulfite [94]. The most common way to reduce GO is by mixing with hydrazine solution. The treatment with hydrazine solution allows restoring the sp^2 orbital and thus the properties of graphene-like particles [91]. The de-oxygenation, of the GO by the hydrazine solution is still not very well understood. GO reduced by hydrazine solution and exposed to hydrogen

plasma is covered with 60 % of well crystallised graphene, which corresponds to islands from 3 to 6 nm, and isolated clustered topological defects i.e. dislocations, pentagons which are the outcomes of the oxidation-reduction process.

Thermally reduced graphene (TRG) is obtained by exfoliation of a graphene layer during heating. During heating the functionalised groups are exothermically decomposed to form CO_2 and water gases which consist of 30 % of the mass [95]. However, according to simulations [96], hydrogen and oxygen atoms are exchanged between the functional groups, which results in breaking away of the carboxyl group. The difference with the experimental data is explained as a result of a possible secondary reaction during the processing between CO and O_2. The exfoliation of GO is possible by heating to 1050 °C under argon gas. The exfoliation occurs when the pressure generated by the gases is higher than the van de Waals interactions linking the graphene sheet. This pressure is estimated around ~25 MPa to exfoliate two layers of graphene [97]. It is also possible to reduced the GO at lower temperature [98], but with reduced effectiveness [86]. TRG obtained consists of 80 % monolayer with a lateral dimension ranging from 100 nm to 2.5 µm and a highly wrinkled surface due to defects. Some functional groups remain after the treatment with a C/O ratio equivalent to 10:1. Because of this defective lattice as well as the remanant functional group, the conductivity of the compact TRG is measured in a range from 10 to 20 $S.cm^{-1}$ [95].

2.5. Production of exfoliated graphite nanoplatelets

In the literature graphite nanoplatelets have many names, ranging from foliated graphite (FG), or sonicated exfoliated graphite (S-EG) to graphite nanosheets (GNS

or GN). As described in the nomenclature, we will use the term of graphite nanoplatelets if the thickness is higher than 10 layers but smaller than 100 nm. There are different ways to obtain GNP which are summarized in Table 2.2. The main method is by intercalating a compound between the layers of graphene to form graphite intercalated compound (GIC) as presented previously.

The GIC tends to exfoliate under heating by thermal shock [99], microwave irradiation [100], or other heating systems such as plasma or flame [99]. Under heating the GIC undergoes an exfoliation due to the tendency of the intercalate in the graphite to vapourise, thus forming gas pockets which may or may not burst [27]. The graphitic layer particles undergo a significant expansion in a dimension perpendicular to the carbon layers of the GICs, forming highly porous wormlike graphite known as expanded graphite (EG), with different pore sizes as presented in Figure 2.5. The morphology of EG is strongly affected by different parameters of the synthesis e.g. donor-type or acceptor-type [101, 102], and exfoliation condition [102, 103]. For example, higher exfoliation leads to a sharp increase in the surface area and a decrease in the density [104], thus thinner platelets.

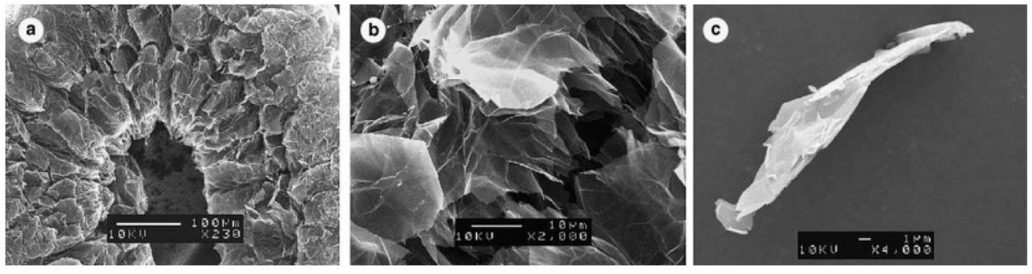

Figure 2.5: SEM photograph of (a) GIC, (b) closer view; and (c) individual GNP after sonication [105].

EG structure can break to form exfoliated thinner platelets under mechanical stress. The EG is generally fractured by milling, stirring, sonication to form GNP. GNPs present a rough surface with parallel edges which collapse and deform. The processing conditions determine the morphology of the GNP, such as the aspect ratio as well as its shape. Also the thickness can be tuned by the processing conditions such as the sonication time for example [105-107]. By changing the pulverisation process of exfoliated graphite flakes, Drzal's group tailored the platelets diameter [108]. A non-desired effect often associated with the treatment of the particles, is a reduction of the diameter and/or scrolling of the platelets sheets. Scrolling of GNP has been observed after a short period of sonication at high energy [109].

The GNPs obtained consist of stacked layers of graphene where the thickness depends on the exfoliation stage. During the acid treatment of natural graphite some carbon double bonds are oxidised, leading to the presence of oxygen-containing functional groups on exfoliated graphite [107, 110, 111]. Therefore GNP presents functional groups on the surface and pores, such as C–O–C, C–OH and –COOH, which improves their affinity with polymers, and organic compounds.

Generally, the formation of EG like GNP does not create any change on the *d*-spacing and 2θ position of the (002) peaks as can be seen in Figure 2.6. The presence of the same 2θ peak shows that the GNP, EG, and graphite are all composed of stacked parallel graphene sheets and processes such as sonication, melting, etc. do not fully exfoliate the graphene sheets. Measurement of the crystalline parameter *Lc* showed a decrease of the thickness of the individual crystallites [107, 112], which means that the formation of EG like GNP leads to the formation of defects and a reduction in crystallinity.

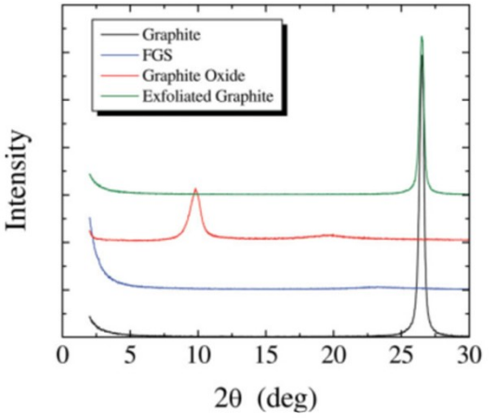

Figure 2.6: XRD patterns of graphite, thermally reduced graphene (called FGS), graphite oxide and GNP (called exfoliated graphite) [113].

An alternative route to the intercalation method has been developed by Wakabayashi et al. [114] based on solid-state shear pulverisation. This is a mechanical method that allows processing in the solid state. It relies on the application of both shear and compressive forces to reduces the size of the filler and disperse it in a polymer matrix [115]. The lateral dimensions of these fillers is between 0.3 to 5 μm with a thickness of 10 nm [114]. The main advantage of this technique is that it does not chemically modify the filler.

Table 2.2: Summary of the main processes to obtain graphene and GNP.

Method	Thickness (nm)	Diameter (µm)	Remarks	Ref
Mechanical exfoliation	0.8	Random	High purity of the flakes	[9]
Exfoliation in solution	~1.5	~1	Scale up – no oxidation	[42]
CVD	≤ 10	-	High aspect ratio - with grain boundaries	[48]
Unzipping SWNT		≥ 0.1	Low aspect ratio – defect site	[58]
Chemically reduced graphene	~2	-	Functional group, defects – bulk quantity	[91]
Thermally reduced graphene	1.75	0.1 – 2.5	Functional groups remained – defective wrinkled surface – bulk quantity	[95]
Intercalation and pulverization (sonication & milling)	~8	~20 - ~1	Oxygen group at the surface / Particles diameter can be tuned with the pulverization process	[108]
Solid-state shear pulverisation	10	0.3 to 5	High quality - no oxygen group at the surface	[114]

2.5.1 Preparation methods of graphene nanocomposite

2.5.1.1 In-situ polymerisation

In-situ polymerisation was first demonstrated by Toyota research in the early 1990s for the creation of clay nanocomposites. Here ε-caprolactam was polymerised in the interlayer of montmorillonite nanoclay [116, 117] to form a so-called nylon hybrid. The process lead to an expansion of the basal planes of montmorillonite, which highly improved the properties of the nylon [118, 119]. The process involved the dispersion of filler in a solvent followed by the addition of radicals and monomer. A

catalyst is then added to trigger the polymerisation. As the polymerisation progresses, the viscosity increases until a solid-like material is created and a high level of dispersion of the filler is achieved due to the steric effects.

In the case of GNP, it is expected that with this method the small molecules are intercalated inside the pores leading to a higher degree of exfoliation of GNP. Due to multipore structures and functionalisation, it is suggested that radicals and monomer are easily adsorbed onto the surface sheets, entering the pores and voids of the particles. However, some studies showed that higher levels of exfoliation are not necessarily achieved using this method [111, 120-123].

In-situ polymerisation can either lead to a covalent linkage between the filler and the matrix [124-126] or non-covalent linkage as in polymethacrylate [127], polyaniline [128], polyethylene [129] and epoxy [130-135]; with epoxy-graphene nanocomposites being the system most studied. By using in-situ polymerisation of aniline monomer and GNP, Wu et al. [128] obtained a PANI-GNP nanocomposite. This nanocomposite presented a very low percolation threshold of ~0.32 vol.% and a high conductivity of ~420 $S.cm^{-1}$.

2.5.1.2 Solution mixing

Solution mixing method is one of the most common processes used for graphene nanocomposites. The process consists of mixing graphene in a suitable solvent. Meanwhile, the polymer is also dissolved in a solvent. Both are then mixed together, and the solution can be further processed. The main advantage of this process is that one can obtain very well dispersed nanocomposites. However, despite a good dispersion in solution, a later (re)aggregation of the particles is possible during a slow evaporation of the solvent [136].

Mainly the level of dispersion is related to the dispersion before and during the mixing. The dispersion of graphene has been investigated in different solvents; it is found to be to related to the Hansen solubility parameters [137, 138], i.e. ~40 $mJ.m^{-2}$ and to the Hildebrand solubility parameter [137], i.e. ~23 $MPa^{1/2}$. Graphene reduced with hydrazine is found to disperse very well in various organic solvents by adjusting the ratio of mixture of organic solvent and water without the use of any stabilisers [138]. Sonication (or ultrasonication) of the filler is often used to disperse graphene in solvent and to break down the remnant aggregates [40]. As it has been observed in carbon nanotube studies, acoustic waves exfoliate the CNTs by a cavitation process but conversely it may also reduce the aspect ratio of the CNTs [139, 140].

As the reduction occurs, the aqueous suspensions of reduced graphene oxide aggregate and precipitate. This effect is attributed to the decrease of the oxygen resulting in a less hydrophilic behaviour [91] or due to a decreased repulsion of negatively charged GO [141]. There are several ways, to prevent this agglomeration, such as coating the graphene with an amphiphilic polymer [142], by functionalising the GO with potassium hydroxide [143] or with sulfonic acid [144]. Li et al. [141] demonstrated that it is possible to obtain an aqueous suspension of reduced GO by controlling the pH of the solution, in another words by maintaining the intrinsic repulsive forces on the graphene surface.

Latex technology is another way to prepare nanocomposites from an aqueous solution. This method consists of mixing a stable aqueous dispersion of graphene with polymer latex, followed by freeze-drying. The synthesis of the latex suspension can be from emulsion or another artificial way [145]. Tkalya et al. [146] synthesised

polystyrene latex and chemically reduced graphene oxide. The obtained nanocomposite presents a high ultimate conductivity ~15 $S.m^{-1}$ and low percolation threshold of ~0.6 vol.%.

2.5.1.3 Melt mixing

Melt mixing or compounding is the most common process for industrial applications of nanocomposites. This process consists of melting the polymer and then adding a nanofiller into the molten matrix for further mixing in an internal mixer or extruder. The dispersion of the filler relies on the shear forces induced by the mixing of the polymer. The operating shear forces are strongly related to the intrinsic properties of the polymer, and the process parameters. This process is the cheapest and environmentally friendliest as is does not require the use of a solvent. However, melt mixing generally leads to a poorer dispersion of the nanofiller in the matrix compared to processes based on solution mixing. It is worth noting that the viscosity of the polymer composite is also dependant on the aspect ratio or concentration of GNP [108]. When a critical concentration is reached above which a percolating network of nanofillers is present a strong increase in viscosity will occur which is not favourable to the processing of the nanocomposite.

By comparing PEN-graphite and PEN-TRG at 1 wt.%, Kim et al. [147] observed an improvement of the elastic modulus of 8 % and 15 %, respectively. It is believed that this improvement is due to an increase of the aspect ratio from 20.8 to 88.4, respectively. However, nanocomposites based on GNP with higher aspect ratio (same thickness but larger diameter) showed surprisingly less favourable mechanical properties. This is in contraction with common composite theory, which predicts higher mechanical properties with increasing aspect ratio of the reinforcing filler.

Based on morphological studies, they observed that higher aspect ratio GNPs are more susceptible to agglomeration or scrolling during mixing, effectively lowering their aspect ratio. In contrast smaller platelets, having a higher bending stiffness, are less sensitive to out of plane bending, buckling, folding or scrolling during processing and therefore maintain their initial aspect ratio. The GNPs can bend and scroll as shown in Figure 2.7, resulting in a decrease in filler efficiency due to this reduced aspect ratio [148].

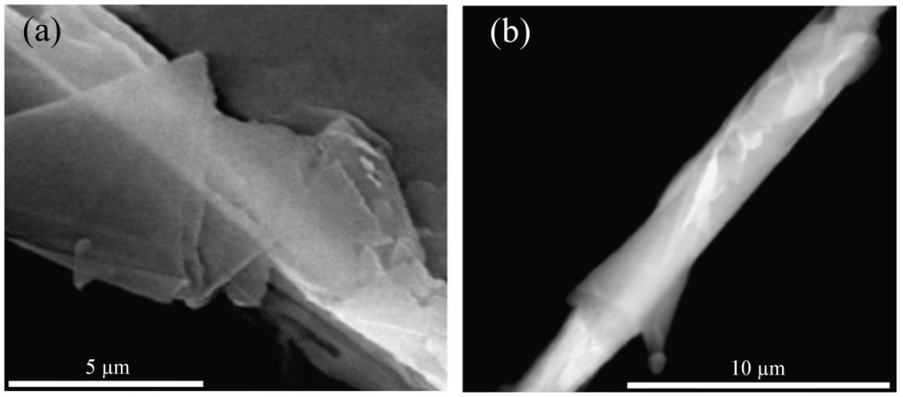

Figure 2.7: ESEM image of GNP (10 nm thickness, 15 μm diameter) (a) folded and (b) scrolled [148].

Other studies reported similar effects where again, in contrast to composite theory, the strength and modulus of melt mixed nanocomposites with high aspect ratio GNPs are found to be lower than nanocomposites with low aspect ratio GNP [148, 149]. Several studies showed that the strength can be reduced with the addition of GNP [131, 150]; the decrease being more significant for high aspect ratio GNPs [122, 150].

2.6. Structure and morphology of graphene nanocomposites

2.6.1 Morphology and alignment

In nanocomposites, the properties at macro-scale are strongly related to the structure at the nano-scale. Due to their dimensionality and their plated architecture, the dispersion of graphene based particles can be compared to clay based particles like montmorillonite. The dispersion of layered particles in a composite can be described in three states as phase separated, intercalated and exfoliated depending on how the polymer can intercalate the layered structure and disperse it [151]. The dispersion is dependent on the affinity between polymer and particles and the processing. The reader is referred for more a detailed review on the dispersion of graphene in polymeric matrix and the quantification of dispersion to Kim et al. [89].

The formation of aggregates is a common feature in nanocomposite processing and it is suspected to reduce the overall mechanical properties of the composite. Agglomeration of particles is prevented by processing, as previously described. Yasmin et al. [106] studied the effect of processing on the dispersion and exfoliation of EG in epoxy matrix. They found that the combined method of sonication and shearing obtained the best results compared to sonication, shearing or direct mixing methods. The dispersion of graphene in function of the dispersion method (i.e. melt mixing, in-situ polymerisation and solution mixing) and in function of the reduction processes of graphene (i.e. chemical reduction and thermal reduction) in polyurethane are studied by TEM and WAXD by Kim et al. [152] and presented in Figure 2.8. It is observed that melt blended PU-TRG leads to a better orientation of the flakes but with graphene stacks compared to in-situ and solution blended composites. Solution blended PU-CRG was in an intercalated state with few stacks

remaining. Interestingly, PU-GO by in-situ polymerisation presented a very well dispersed state which is associated to the higher affinity of the GO with the TPU reactive groups. The formation of agglomerates of graphene in a polycarbonate matrix was monitored with small-angle neutron scattering at different loadings (from 0.1 vol.% to 2.2 vol.%). Despite the affinity between polycarbonate and graphene, it was observed that the particles' radius was in a range of a few mm, but with loading increasing, the number of graphene sheets in the stack doubles and the graphene stack spacing is reduced by 35 %.

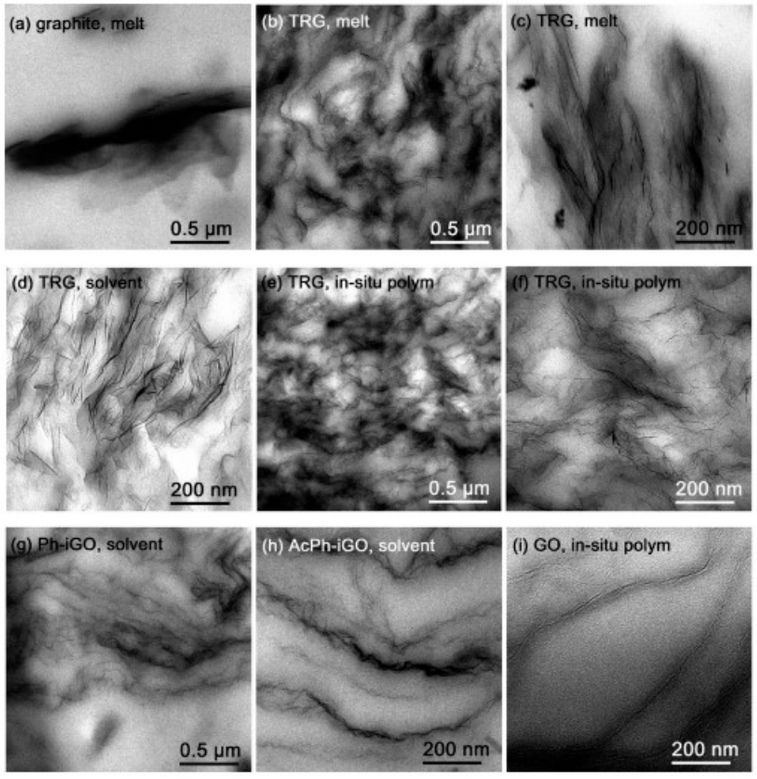

Figure 2.8: TEM micrographs of TPU with (a) melt-compound : 2.7 vol.% graphite, (b, c) melt-blended: TRG, (d) solvent-mixed: TRG, (e, f) in situ polymerized: 1.6 vol.% TRG, (g) solvent cast: 1.6 vol.% CRG with phenyl isocyanate, (h) CRG with acetylphenyl isocyanate, and (i) in situ polymerized 1.5 vol.% GO [152].

The conformation of graphene-like particles in a polymer is very sensitive to the media. For instance, pristine graphene sheets embedded in a copolymeric matrix of PMMA and methacrylic acid are found to irremediably scroll and fold when the temperature is raised above its glass transition [153]. A similar effect has been observed for pristine graphene deposited on a PMMA substrate, when the system is cooled down from above the glass temperature transition and the graphene sheet began to buckle from the edges until it folded into a stack [154]. Scrolling of graphene is found to be related to the high aspect ratio of GNP in melt compounding, as previously described. Recently, Zaman et al. [155] found that GNP with higher exfoliation levels by grafting 4,4'-methylene diphenyl diisocyanate in epoxy matrix are more able to scroll than non-treated GNP. Increasing the interaction between the polymer and the filler, however, seems to be a way for counterbalancing the scrolling effect of graphene oxide in polymer matrices, and allows the particles to adopt a more extended conformation [156].

Generally traditional processing as described above leads not to organisation. However to improve the nanocomposite properties it is crucial not only to control the dispersion of the filler but also the alignment and organisation of the filler in the matrix. Similar to CNTs, alignment can be observed by a variety of techniques such as polarised Raman, X-Ray, and by microscopy like SEM and TEM.

During in-situ polymerisation it is possible to orient the filler via driving forces such as flow or electrical/magnetic fields and to "lock-in" the structure by polymerisation. One of the main forces studied is the motion of particles by electrical forces. The alignment of the filler is possible due to the strong crystalline anisotropy of graphene

and graphite. For example, Wang et al. [157] have improved the visible light transmittance by orienting the GNP film in a polyester via an electric field.

It is also possible to orient the filler directly via processing. Spin coating [158] and filtration [159, 160] are easy ways to align the particles in a 2D manner along the surface. As it is demonstrated for CNTs [161], the alignment of graphene can also be obtained via melt processing; extrusion, injection moulding, melt spinning, electrospinning, uniaxial or biaxial solid-state drawing, etc. Kalaitzidou et al. [149] pointed out that nanocomposites with larger platelets, i.e. higher surface area, present a better alignment along the flow direction during injection moulding. However, owing to the fluid dynamics involved in this process, the alignment along the flow is often non-homogeneous. In other words the filler is more aligned along the skin than in the core due to the fountain flow behaviour.

2.7. Conclusions

Since the first isolation, graphene as well as graphene nanocomposites are a source of great expectations. The exponential increase of papers related to graphene nanocomposites shows the scientific excitement for this new topic in a wide range of domains including electrical devices, sensors, barrier properties, mechanical reinforcement, etc.. The following issues are, according to the authors, critical in order to fully understand and utilize the potential of graphene in polymer matrices:

1) The wide range of production methods offers different kinds of graphene which goes from functionalised graphene via reduced GO to pristine graphene via exfoliation in solution but also extremely high aspect ratio graphene via CVD. However, the intrinsic properties of these monolayers are highly dependent on production method, either in terms of mechanical or transport properties.

2) As with all nanoparticles, the formation of aggregates is also a common feature in graphene nanocomposites, which like with CNTs increases with nanofiller loading. More interestingly, graphene-like fillers are extremely sensitive to the media. Just increasing the temperature above the T_g of the host matrix for example, is able to irremediably scroll the embedded graphene sheets into lower aspect ratio fillers.

3) The processing history and its conditions strongly define dispersion, exfoliation and orientation of graphene platelets.

2.8. References

1. E.A. Rohlfing, D.M. Cox, and A. Kaldor, J Chem Phys, 1984. **81**(7): p. 3322-3330.
2. H.W. Kroto, J.R. Heath, S.C. O'Brien, R.F. Curl, and R.E. Smalley, Nature, 1985. **318**(6042): p. 162-163.
3. H.W. Kroto, Nature, 1987. **329**(6139): p. 529-531.
4. S. Iijima, Nature, 1991. **354**(6348): p. 56-58.
5. M. Monthioux and V.L. Kuznetsov, Carbon, 2006. **44**(9): p. 1621-1623.
6. S. Iijima and T. Ichihashi, Nature, 1993. **363**(6430): p. 603-605.
7. D.S. Bethune, C.H. Klang, M.S. de Vries, G. Gorman, R. Savoy, J. Vazquez, and R. Beyers, Nature, 1993. **363**(6430): p. 605-607.
8. E.T. Thostenson, Z. Ren, and T.-W. Chou, Composites Science and Technology, 2001. **61**(13): p. 1899-1912.
9. K.S. Novoselov, A.K. Geim, S.V. Morozov, D. Jiang, Y. Zhang, S.V. Dubonos, I.V. Grigorieva, and A.A. Firsov, Science, 2004. **306**(5696): p. 666-669.
10. A.K. Geim and K.S. Novoselov, Nature Materials, 2007. **6**(3): p. 183-191.
11. M.I. Katsnelson, Materials Today. **10**(1-2): p. 20-27.
12. A.K. Geim, Science, 2009. **324**(5934): p. 1530-1534.
13. Y.H. Wu, T. Yu, and Z.X. Shen, Journal of Applied Physics, 2010. **108**(7): p. 071301.
14. R.R. Nair, P. Blake, A.N. Grigorenko, K.S. Novoselov, T.J. Booth, T. Stauber, N.M.R. Peres, and A.K. Geim, Science, 2008. **320**(5881): p. 1308-1308.
15. C. Lee, X. Wei, J.W. Kysar, and J. Hone, Science, 2008. **321**(5887): p. 385-388.
16. A.A. Balandin, S. Ghosh, W. Bao, I. Calizo, D. Teweldebrhan, F. Miao, and C.N. Lau, Nano Letters, 2008. **8**(3): p. 902-907.
17. J.S. Bunch, S.S. Verbridge, J.S. Alden, A.M. van der Zande, J.M. Parpia, H.G. Craighead, and P.L. McEuen, Nano Letters, 2008. **8**(8): p. 2458-2462.
18. M. Fang, K. Wang, H. Lu, Y. Yang, and S. Nutt, Journal of Materials Chemistry, 2009. **19**(38): p. 7098-7105.
19. X. Zhao, Q. Zhang, D. Chen, and P. Lu, Macromolecules, 2010. **43**(5): p. 2357-2363.
20. P. Steurer, R. Wissert, R. Thomann, and R. Mülhaupt, Macromolecular Rapid Communications, 2009. **30**(4-5): p. 316-327.
21. L. Gomez De Arco, Y. Zhang, C.W. Schlenker, K. Ryu, M.E. Thompson, and C. Zhou, ACS Nano, 2010. **4**(5): p. 2865-2873.

22. W. Hong, Y. Xu, G. Lu, C. Li, and G. Shi, Electrochemistry Communications, 2008. **10**(10): p. 1555-1558.

23. S. Kim and L.T. Drzal, Solar Energy Materials and Solar Cells, 2009. **93**(1): p. 136-142.

24. X. Wang, L. Zhi, and K. Mullen, Nano Letters, 2007. **8**(1): p. 323-327.

25. D.-W. Wang, F. Li, J. Zhao, W. Ren, Z.-G. Chen, J. Tan, Z.-S. Wu, I. Gentle, G.Q. Lu, and H.-M. Cheng, ACS Nano, 2009. **3**(7): p. 1745-1752.

26. A. Yu, I. Roes, A. Davies, and Z. Chen, Applied Physics Letters, 2010. **96**(25): p. 253105.

27. D. Chung, Journal of Materials Science, 2002. **37**(8): p. 1475-1489.

28. H. Lipson and A.R. Stokes, Proceedings of the Royal Society of London. Series A, Mathematical and Physical Sciences, 1942. **181**(984): p. 101-105.

29. P. Nemes-Incze, Z. Osváth, K. Kamarás, and L.P. Biró, Carbon, 2008. **46**(11): p. 1435-1442.

30. S. Stankovich, D.A. Dikin, G.H.B. Dommett, K.M. Kohlhaas, E.J. Zimney, E.A. Stach, R.D. Piner, S.T. Nguyen, and R.S. Ruoff, Nature, 2006. **442**(7100): p. 282-286.

31. T. Ramanathan, A.A. Abdala, S. Stankovich, D.A. Dikin, M. Herrera-Alonso, R.D. Piner, D.H. Adamson, H.C. Schniepp, X. Chen, R.S. Ruoff, S.T. Nguyen, I.A. Aksay, R.K. Prud'homme, and L.C. Brinson, Nature Nanotechnology, 2008. **3**(6): p. 327-331.

32. M.J. Allen, V.C. Tung, and R.B. Kaner, Chemical Reviews, 2009. **110**(1): p. 132-145.

33. C. Soldano, A. Mahmood, and E. Dujardin, Carbon, 2010. **48**(8): p. 2127-2150.

34. A. Bianco, H.-M. Cheng, T. Enoki, Y. Gogotsi, R.H. Hurt, N. Koratkar, T. Kyotani, M. Monthioux, C.R. Park, J.M.D. Tascon, and J. Zhang, Carbon, 2013. **65**(0): p. 1-6.

35. X. Wang, M. Zhao, and D.D. Nolte, Applied Physics Letters, 2009. **95**(8): p. 081102.

36. J.C. Meyer, A.K. Geim, M.I. Katsnelson, K.S. Novoselov, T.J. Booth, and S. Roth, Nature, 2007. **446**(7131): p. 60-63.

37. J.C. Meyer, A.K. Geim, M.I. Katsnelson, K.S. Novoselov, D. Obergfell, S. Roth, C. Girit, and A. Zettl, Solid State Communications, 2007. **143**(1-2): p. 101-109.

38. Y. Hernandez, V. Nicolosi, M. Lotya, F.M. Blighe, Z.Y. Sun, S. De, I.T. McGovern, B. Holland, M. Byrne, Y.K. Gun'ko, J.J. Boland, P. Niraj, G. Duesberg, S. Krishnamurthy, R. Goodhue, J. Hutchison, V. Scardaci, A.C. Ferrari, and J.N. Coleman, Nature Nanotechnology, 2008. **3**(9): p. 563-568.

39. C.E. Hamilton, J.R. Lomeda, Z. Sun, J.M. Tour, and A.R. Barron, Nano Letters, 2009. **9**(10): p. 3460-3462.

40. U. Khan, A. O'Neill, M. Lotya, S. De, and J.N. Coleman, SMALL, 2010. **6**(7): p. 864-871.

41. S. Vadukumpully, J. Paul, and S. Valiyaveettil, Carbon, 2009. **47**(14): p. 3288-3294.

42. M. Lotya, Y. Hernandez, P.J. King, R.J. Smith, V. Nicolosi, L.S. Karlsson, F.M. Blighe, S. De, Z.M. Wang, I.T. McGovern, G.S. Duesberg, and J.N. Coleman, Journal of the American Chemical Society, 2009. **131**(10): p. 3611-3620.

43. A.B. Bourlinos, V. Georgakilas, R. Zboril, T.A. Steriotis, A.K. Stubos, and C. Trapalis, Solid State Communications, 2009. **149**(47-48): p. 2172-2176.

44. S. Biswas and L.T. Drzal, Nano Letters, 2008. **9**(1): p. 167-172.

45. C. Berger, Z. Song, T. Li, X. Li, A.Y. Ogbazghi, R. Feng, Z. Dai, A.N. Marchenkov, E.H. Conrad, P.N. First, and W.A. de Heer, The Journal of Physical Chemistry B, 2004. **108**(52): p. 19912-19916.

46. W.A. de Heer, C. Berger, X. Wu, P.N. First, E.H. Conrad, X. Li, T. Li, M. Sprinkle, J. Hass, M.L. Sadowski, M. Potemski, and G. Martinez, Solid State Communications, 2007. **143**(1-2): p. 92-100.

47. Q. Yu, J. Lian, S. Siriponglert, H. Li, Y.P. Chen, and S.-S. Pei, Applied Physics Letters, 2008. **93**(11): p. 113103.

48. A. Reina, X. Jia, J. Ho, D. Nezich, H. Son, V. Bulovic, M.S. Dresselhaus, and J. Kong*, Nano Letters, 2009. **9**(8): p. 3087-3087.

49. K.S. Kim, Y. Zhao, H. Jang, S.Y. Lee, J.M. Kim, K.S. Kim, J.-H. Ahn, P. Kim, J.-Y. Choi, and B.H. Hong, Nature, 2009. **457**(7230): p. 706-710.

50. X. Li, W. Cai, J. An, S. Kim, J. Nah, D. Yang, R. Piner, A. Velamakanni, I. Jung, E. Tutuc, S.K. Banerjee, L. Colombo, and R.S. Ruoff, Science, 2009. **324**(5932): p. 1312-1314.

51. P.Y. Huang, C.S. Ruiz-Vargas, A.M. van der Zande, W.S. Whitney, M.P. Levendorf, J.W. Kevek, S. Garg, J.S. Alden, C.J. Hustedt, Y. Zhu, J. Park, P.L. McEuen, and D.A. Muller, Nature, 2011. **469**(7330): p. 389-392.

52. P.W. Sutter, J.-I. Flege, and E.A. Sutter, Nature Materials, 2008. **7**(5): p. 406-411.

53. A.J. Pollard, R.R. Nair, S.N. Sabki, C.R. Staddon, L.M.A. Perdigao, C.H. Hsu, J.M. Garfitt, S. Gangopadhyay, H.F. Gleeson, A.K. Geim, and P.H. Beton, The Journal of Physical Chemistry C, 2009. **113**(38): p. 16565-16567.

54. A. Reina, H. Son, L. Jiao, B. Fan, M.S. Dresselhaus, Z. Liu, and J. Kong, The Journal of Physical Chemistry C, 2008. **112**(46): p. 17741-17744.

55. W. Regan, N. Alem, B. Aleman, B. Geng, C. Girit, L. Maserati, F. Wang, M. Crommie, and A. Zettl, Applied Physics Letters, 2010. **96**(11): p. 113102.

56. S. Bae, H. Kim, Y. Lee, X. Xu, J.-S. Park, Y. Zheng, J. Balakrishnan, T. Lei, H. Ri Kim, Y.I. Song, Y.-J. Kim, K.S. Kim, B. Ozyilmaz, J.-H. Ahn, B.H. Hong, and S. Iijima, Nat Nano, 2010. **5**(8): p. 574-578.

57. L. Jiao, L. Zhang, X. Wang, G. Diankov, and H. Dai, Nature, 2009. **458**(7240): p. 877-880.

58. D.V. Kosynkin, A.L. Higginbotham, A. Sinitskii, J.R. Lomeda, A. Dimiev, B.K. Price, and J.M. Tour, Nature, 2009. **458**(7240): p. 872-876.

59. Z. Chen, Y.-M. Lin, M.J. Rooks, and P. Avouris, Physica E: Low-dimensional Systems and Nanostructures, 2007. **40**(2): p. 228-232.

60. X. Li, X. Wang, L. Zhang, S. Lee, and H. Dai, Science, 2008. **319**(5867): p. 1229-1232.

61. S.S. Datta, D.R. Strachan, S.M. Khamis, and A.T.C. Johnson, Nano Letters, 2008. **8**(7): p. 1912-1915.

62. J. Campos-Delgado, J.M. Romo-Herrera, X. Jia, D.A. Cullen, H. Muramatsu, Y.A. Kim, T. Hayashi, Z. Ren, D.J. Smith, Y. Okuno, T. Ohba, H. Kanoh, K. Kaneko, M. Endo, H. Terrones, M.S. Dresselhaus, and M. Terrones, Nano Letters, 2008. **8**(9): p. 2773-2778.

63. M.-F. Yu, M.J. Dyer, and R.S. Ruoff, Journal of Applied Physics, 2001. **89**(8): p. 4554-4557.

64. L.B. Ebert, Annu. Rev. Mater. Sci., 1976. **6**: p. 181-211.

65. H. Shioyama, Synthetic Metals, 2000. **114**(1): p. 1-15.

66. M.S. Dresselhaus and G. Dresselhaus, Advances in Physics, 2002. **51**(1): p. 1 - 186.

67. B.C. Brodie, Philosophical Transactions of the Royal Society of London, 1859. **149**(ArticleType: research-article / Full publication date: 1859 / Copyright © 1859 The Royal Society): p. 249-259.

68. L. Staudenmaier, Berichte der deutschen chemischen Gesellschaft, 1898. **31**(2): p. 1481-1487.

69. W.S. Hummers and R.E. Offeman, Journal of the American Chemical Society, 1958. **80**(6): p. 1339-1339.

70. H.K. Jeong and et al., Journal of Physics D: Applied Physics, 2009. **42**(6): p. 065418.

71. C. Hontoria-Lucas, A.J. López-Peinado, J.d.D. López-González, M.L. Rojas-Cervantes, and R.M. Martín-Aranda, Carbon, 1995. **33**(11): p. 1585-1592.

72. H. Wang and Y.H. Hu, Industrial & Engineering Chemistry Research, 2011. **50**(10): p. 6132-6137.

73. J.-L. Li, K.N. Kudin, M.J. McAllister, R.K. Prud'homme, I.A. Aksay, and R. Car, Physical Review Letters, 2006. **96**(17): p. 176101.

74. U. Hofmann and R. Holst, Berichte der deutschen chemischen Gesellschaft (A and B Series), 1939. **72**(4): p. 754-771.

75. G. Ruess, Monatshefte für Chemie, 1947. **76**: p. 381-417.

76. W. Scholz and H.P. Boehm, Zeitschrift für anorganische und allgemeine Chemie, 1969. **369**(3-6): p. 327-340.

77. T. Nakajima, A. Mabuchi, and R. Hagiwara, Carbon, 1988. **26**(3): p. 357-361.

78. T. Szabó, O. Berkesi, P. Forgó, K. Josepovits, Y. Sanakis, D. Petridis, and I. Dékány, Chemistry of Materials, 2006. **18**(11): p. 2740-2749.

79. A. Lerf, H. He, M. Forster, and J. Klinowski, The Journal of Physical Chemistry B, 1998. **102**(23): p. 4477-4482.

80. K. Erickson, R. Erni, Z. Lee, N. Alem, W. Gannett, and A. Zettl, Advanced Materials, 2010. **22**(40): p. 4467-4472.

81. D.R. Dreyer, S. Park, C.W. Bielawski, and R.S. Ruoff, Chemical Society Reviews, 2010. **39**(1): p. 228-240.

82. S. Stankovich, R.D. Piner, S.T. Nguyen, and R.S. Ruoff, Carbon, 2006. **44**(15): p. 3342-3347.

83. K.A. Mkhoyan, A.W. Contryman, J. Silcox, D.A. Stewart, G. Eda, C. Mattevi, S. Miller, and M. Chhowalla, Nano Letters, 2009. **9**(3): p. 1058-1063.

84. L. Zhang, J.J. Liang, Y. Huang, Y.F. Ma, Y. Wang, and Y.S. Chen, Carbon, 2009. **47**(14): p. 3365-3368.

85. O.C. Compton and S.T. Nguyen, SMALL, 2010. **6**(6): p. 711-723.

86. D. Yang, A. Velamakanni, G. Bozoklu, S. Park, M. Stoller, R.D. Piner, S. Stankovich, I. Jung, D.A. Field, C.A. Ventrice Jr, and R.S. Ruoff, Carbon, 2009. **47**(1): p. 145-152.

87. L.J. Cote, R. Cruz-Silva, and J. Huang, Journal of the American Chemical Society, 2009. **131**(31): p. 11027-11032.

88. H. Wang, J.T. Robinson, X. Li, and H. Dai, Journal of the American Chemical Society, 2009. **131**(29): p. 9910-9911.

89. H. Kim, A.A. Abdala, and C.W. Macosko, Macromolecules, 2010. **43**(16): p. 6515-6530.

90. S. Park and R.S. Ruoff, Nat Nano, 2009. **4**(4): p. 217-224.

91. S. Stankovich, D.A. Dikin, R.D. Piner, K.A. Kohlhaas, A. Kleinhammes, Y. Jia, Y. Wu, S.T. Nguyen, and R.S. Ruoff, Carbon, 2007. **45**(7): p. 1558-1565.

92. G. Wang, J. Yang, J. Park, X. Gou, B. Wang, H. Liu, and J. Yao, The Journal of Physical Chemistry C, 2008. **112**(22): p. 8192-8195.

93. A.B. Bourlinos, D. Gournis, D. Petridis, T. Szabó, A. Szeri, and I. Dékány, Langmuir, 2003. **19**(15): p. 6050-6055.

94. T. Zhou, F. Chen, C. Tang, H. Bai, Q. Zhang, H. Deng, and Q. Fu, Composites Science and Technology, 2011. **71**(9): p. 1266-1270.

95. H.C. Schniepp, J.-L. Li, M.J. McAllister, H. Sai, M. Herrera-Alonso, D.H. Adamson, R.K. Prud'homme, R. Car, D.A. Saville, and I.A. Aksay, The Journal of Physical Chemistry B, 2006. **110**(17): p. 8535-8539.

96. J.T. Paci, T. Belytschko, and G.C. Schatz, Journal of Physical Chemistry C, 2007. **111**(49): p. 18099-18111.

97. M.J. McAllister, J.-L. Li, D.H. Adamson, H.C. Schniepp, A.A. Abdala, J. Liu, M. Herrera-Alonso, D.L. Milius, R. Car, R.K. Prud'homme, and I.A. Aksay, Chemistry of Materials, 2007. **19**(18): p. 4396-4404.

98. W. Chen and L. Yan, Nanoscale, 2010. **2**(4): p. 559-563.

99. D.D.L. Chung, Journal of Materials Science, 1987. **22**(12): p. 4190-4198.

100. B. Tryba, A.W. Morawski, and M. Inagaki, Carbon, 2005. **43**(11): p. 2417-2419.

101. A. Yoshida, Y. Hishiyama, and M. Inagaki, Carbon, 1991. **29**(8): p. 1227-1231.

102. F. Kang, T.-Y. Zhang, and Y. Leng, Journal of Physics and Chemistry of Solids, 1996. **57**(6-8): p. 883-888.

103. F. Kang, Y.-P. Zheng, H.-N. Wang, Y. Nishi, and M. Inagaki, Carbon, 2002. **40**(9): p. 1575-1581.

104. P. Ramesh and S. Sampath, Analytical Chemistry, 2003. **75**(24): p. 6949-6957.

105. J. Li, J.-K. Kim, and M. Lung Sham, Scripta Materialia, 2005. **53**(2): p. 235-240.

106. A. Yasmin, J.-J. Luo, and I.M. Daniel, Composites Science and Technology, 2006. **66**(9): p. 1182-1189.

107. G.H. Chen, W.G. Weng, D.J. Wu, C.L. Wu, J.R. Lu, P.P. Wang, and X.F. Chen, Carbon, 2004. **42**(4): p. 753-759.

108. K. Kalaitzidou, H. Fukushima, and L.T. Drzal, Carbon, 2007. **45**(7): p. 1446-1452.

109. L.M. Viculis, J.J. Mack, and R.B. Kaner, Science, 2003. **299**(5611): p. 1361-.

110. Y. She, G. Chen, and D. Wu, Polymer International, 2007. **56**(5): p. 679-685.

111. R.K. Goyal, P.A. Jagadalle, and U.P. Mulik, Journal of Applied Polymer Science, 2009. **111**(4): p. 2071-2077.

112. T. Ramanathan, S. Stankovich, D.A. Dikin, H. Liu, H. Shen, S.T. Nguyen, and L.C. Brinson, Journal of Polymer Science Part B: Polymer Physics, 2007. **45**(15): p. 2097-2112.

113. S. Ansari and E.P. Giannelis, Journal of Polymer Science Part B-Polymer Physics, 2009. **47**(9): p. 888-897.

114. K. Wakabayashi, C. Pierre, D.A. Dikin, R.S. Ruoff, T. Ramanathan, L.C. Brinson, and J.M. Torkelson, Macromolecules, 2008. **41**(6): p. 1905-1908.

115. N. Furgiuele, A.H. Lebovitz, K. Khait, and J.M. Torkelson, Polymer Engineering & Science, 2000. **40**(6): p. 1447-1457.

116. A. Usuki, M. Kawasumi, Y. Kojima, A. Okada, T. Kurauchi, and O. Kamigaito, Journal Materials Research, 1993. **8**(5): p. 1174-1178.

117. A. Usuki, Y. Kojima, M. Kawasumi, A. Okada, Y. Fukushima, T. Kurauchi, and O. Kamigaito, Journal of Materials Research, 1993. **8**: p. 1179-1184.

118. Y. Kojima, A. Usuki, M. Kawasumi, A. Okada, T. Kurauchi, and O. Kamigaito, Journal of Applied Polymer Science, 1993. **49**(7): p. 1259-1264.

119. Y. Kojima, A. Usuki, M. Kawasumi, A. Okada, Y. Fukushima, T. Kurauchi, and O. Kamigaito, Journal of Materials Research, 1993. **8,**: p. 1185-1189.

120. G.-H. Chen, D.-J. Wu, W.-G. Weng, B. He, and W.-l. Yan, Polymer International, 2001. **50**(9): p. 980-985.

121. N.K. Srivastava and R.M. Mehra, Journal of Applied Polymer Science, 2008. **109**(6): p. 3991-3999.

122. L.N. Song, M. Xiao, and Y.Z. Meng, Composites Science and Technology, 2006. **66**(13): p. 2156-2162.

123. G.H. Chen, W.G. Weng, D.J. Wu, and C.L. Wu, European Polymer Journal, 2003. **39**(12): p. 2329-2335.

124. L. Kan, Z. Xu, and C. Gao, Macromolecules, 2010. **44**(3): p. 444-452.

125. H. Hu, X. Wang, J. Wang, L. Wan, F. Liu, H. Zheng, R. Chen, and C. Xu, Chemical Physics Letters, 2010. **484**(4-6): p. 247-253.

126. S.H. Lee, D.R. Dreyer, J. An, A. Velamakanni, R.D. Piner, S. Park, Y. Zhu, S.O. Kim, C.W. Bielawski, and R.S. Ruoff, Macromolecular Rapid Communications, 2010. **31**(3): p. 281-288.

127. J.Y. Jang, H.M. Jeong, and B.K. Kim, Macromolecular Research, 2009. **17**(8): p. 626-628.

128. X. Wu, S. Qi, J. He, and G. Duan, Journal of Materials Science, 2010. **45**(2): p. 483-489.

129. F.d.C. Fim, J.M. Guterres, N.R.S. Basso, and G.B. Galland, Journal of Polymer Science Part A: Polymer Chemistry, 2010. **48**(3): p. 692-698.

130. M.A. Rafiee, J. Rafiee, Z. Wang, H. Song, Z.-Z. Yu, and N. Koratkar, ACS Nano, 2009. **3**(12): p. 3884-3890.

131. J. Li, M.L. Sham, J.-K. Kim, and G. Marom, Composites Science and Technology, 2007. **67**(2): p. 296-305.

132. A. Yu, P. Ramesh, M.E. Itkis, E. Bekyarova, and R.C. Haddon, The Journal of Physical Chemistry C, 2007. **111**(21): p. 7565-7569.

133. A. Yu, P. Ramesh, X. Sun, E. Bekyarova, M.E. Itkis, and R.C. Haddon, Advanced Materials, 2008. **20**(24): p. 4740-4744.

134. L.M. Veca, M.J. Meziani, W. Wang, X. Wang, F. Lu, P. Zhang, Y. Lin, R. Fee, J.W. Connell, and Y.-P. Sun, Advanced Materials, 2009. **21**(20): p. 2088-2092.

135. M.A. Rafiee, J. Rafiee, Z.-Z. Yu, and N. Koratkar, Applied Physics Letters, 2009. **95**(22): p. 223103.

136. M. Moniruzzaman and K.I. Winey, Macromolecules, 2006. **39**(16): p. 5194-5205.

137. Y. Hernandez, M. Lotya, D. Rickard, S.D. Bergin, and J.N. Coleman, Langmuir, 2009. **26**(5): p. 3208-3213.

138. S. Park, J. An, I. Jung, R.D. Piner, S.J. An, X. Li, A. Velamakanni, and R.S. Ruoff, Nano Letters, 2009. **9**(4): p. 1593-1597.

139. A. Lucas, C.c. Zakri, M. Maugey, M. Pasquali, P.v.d. Schoot, and P. Poulin, The Journal of Physical Chemistry C, 2009. **113**(48): p. 20599-20605.

140. F. Hennrich, R. Krupke, K. Arnold, J.A. Rojas Stutz, S. Lebedkin, T. Koch, T. Schimmel, and M.M. Kappes, The Journal of Physical Chemistry B, 2007. **111**(8): p. 1932-1937.

141. D. Li, M.B. Muller, S. Gilje, R.B. Kaner, and G.G. Wallace, Nat Nano, 2008. **3**(2): p. 101-105.

142. S. Stankovich, R.D. Piner, X.Q. Chen, N.Q. Wu, S.T. Nguyen, and R.S. Ruoff, Journal of Materials Chemistry, 2006. **16**(2): p. 155-158.

143. S. Park, J. An, R.D. Piner, I. Jung, D. Yang, A. Velamakanni, S.T. Nguyen, and R.S. Ruoff, Chemistry of Materials, 2008. **20**(21): p. 6592-6594.

144. Y. Si and E.T. Samulski, Nano Letters, 2008. **8**(6): p. 1679-1682.

145. N. Grossiord, J. Loos, O. Regev, and C.E. Koning, Chemistry of Materials, 2006. **18**(5): p. 1089-1099.

146. E. Tkalya, M. Ghislandi, A. Alekseev, C. Koning, and J. Loos, Journal of Materials Chemistry, 2010. **20**(15): p. 3035-3039.

147. H. Kim and C.W. Macosko, Macromolecules, 2008. **41**(9): p. 3317-3327.

148. K. Kalaitzidou, H. Fukushima, and L.T. Drzal, Composites Part a-Applied Science and Manufacturing, 2007. **38**(7): p. 1675-1682.

149. K. Kalaitzidou, H. Fukushima, H. Miyagawa, and L.T. Drzal, Polymer Engineering & Science, 2007. **47**(11): p. 1796-1803.

150. Y.F. Zhao, M. Xiao, S.J. Wang, X.C. Ge, and Y.Z. Meng, Composites Science and Technology, 2007. **67**(11-12): p. 2528-2534.

151. M. Alexandre and P. Dubois, Materials Science and Engineering: R: Reports, 2000. **28**(1-2): p. 1-63.

152. H. Kim, Y. Miura, and C.W. Macosko, Chemistry of Materials, 2010. **22**(11): p. 3441-3450.

153. Q. Li, Z. Li, M. Chen, and Y. Fang, Nano Letters, 2009. **9**(5): p. 2129-2132.

154. Z.J. Li, Z.G. Cheng, R. Wang, Q. Li, and Y. Fang, Nano Letters, 2009. **9**(10): p. 3599-3602.

155. I. Zaman, T.T. Phan, H.-C. Kuan, Q. Meng, L.T. Bao La, L. Luong, O. Youssf, and J. Ma, Polymer, 2011. **52**(7): p. 1603-1611.

156. M. Hirata, T. Gotou, S. Horiuchi, M. Fujiwara, and M. Ohba, Carbon, 2004. **42**(14): p. 2929-2937.

157. H.Q. Wang, H.Y. Zhang, W.F. Zhao, W. Zhang, and G.H. Chen, Composites Science and Technology, 2008. **68**(1): p. 238-243.

158. G. Eda, H.E. Unalan, N. Rupesinghe, G.A.J. Amaratunga, and M. Chhowalla, Applied Physics Letters, 2008. **93**(23): p. -.

159. G. Eda, Y.Y. Lin, S. Miller, C.W. Chen, W.F. Su, and M. Chhowalla, Applied Physics Letters, 2008. **92**(23): p. -.

160. D.A. Dikin, S. Stankovich, E.J. Zimney, R.D. Piner, G.H.B. Dommett, G. Evmenenko, S.T. Nguyen, and R.S. Ruoff, Nature, 2007. **448**(7152): p. 457-460.

161. Z. Wang, P. Ciselli, and T Peijs, Nanotechnology, 2007. **18**(45): p. 455709.

Chapter 3

Graphene for mechanical reinforcement: potential & challenges

3.1. Introduction

Since the discovery of polymer nanocomposites, mechanical reinforcement has been studied. Due to its chemical structure, the mechanical properties of graphene composite compared to CNT composite reveal some similarities. Indeed, good dispersion, alignment, and stress transfer are some important parameters to fully exploit the potential of the nanofiller [1]. But due to its 2D dimensionality, graphene nanocomposites reveal several differences. Despite the fact it has a similar Young's modulus, due to its dimensionality graphene can outperform SWNT in composite applications. For instance, a similar length of graphene has a higher surface in contact with the polymer which can transfer the load more effectively since it has both its sides in contact with the polymer. On the contrary, hollow SWNTs can only transfer the stress through their outer surface.

However, its dimensionality also creates new challenges for mechanical reinforcement. For example, graphene's ability to fold in a stack or to crumble and scroll makes it very sensitive to processing. In the case of carbon nanotubes a disordered (random) state of nanotubes can be transferred into an ordered (aligned) state through stretching or drawing. Wang et al. [2], for example, report a high degree of alignment of SWNTs in their composite after solid-state drawing. It remains to be seen if this is also possible with disordered 2D graphene nanosheets.

A brief overview of the mechanical properties of graphene composites is given in order to fully exploit the potential of graphene and to overcome the challenges posed by the 2D character of graphene.

3.2. Mechanical models

In the literature, there are several mechanical models to predict the mechanical behaviour of composites. For 2D particles, it includes models such as the rule of mixture [3] and Halpin-Tsai model [4], which will be discussed in the next paragraphs. Other model can also be used including the derived Mori-Tanaka model by Eshelby [5] which is a theoretical model well suited for platelets fillers, or the Tandon-Weng model, a derived Mori-Tanaka model for isotropic particle in an isotropic matrix [6]. In addition, the shear-lag theory [7] can be used to predict the stress distribution as well as the stress transfer between the particle and the matrix.

3.2.1 Rule of mixture

The rule of mixture is a generic model to predict composite properties. The model considers unidirectionnally oriented fibres. It is a simple model where the properties

of the composites are equivalent to the average between the matrix and the filler properties depending on their loading. The mains assumptions are that the fibres are continuous (i) and that there is a perfect stress transfer between the fibre and the matrix (ii).

The model consists of calculating the properties of the composite along the fibre direction (Voigt model for upper bound modulus) and perpendicular to the fibre direction (Reuss model for lower bound modulus).

The *upper bound,* (modulus along the fibre direction), and *lower bound* (modulus transverse to the fibre direction) models are defined by Equation 3.1 and 3.2 respectively [3]:

$$E_c = E_m(1 - \varphi_f) + E_f\varphi_f \qquad 3.1$$

$$\frac{1}{E_c} = \frac{\varphi_f}{E_f} + \frac{(1-\varphi_f)}{E_m} \qquad 3.2$$

Where E_c and E_m are the composite and matrix Young's modulus, respectively and φ_f is the volume fraction of the reinforcing filler. It is often assumed that the Young's modulus of composites lies in between the upper and the lower bound, depending on filler aspect ratio and fibre orientation.

3.2.2 Halpin-Tsai model

Halpin–Tsai model is a model used to evaluate the stiffness of composites based on aligned but discontinuous fibres [4]. This model predicts the elastic constants of composite materials and is one of the most commonly used models for short fibre

composites as it is based on a simple set of equations that predict all the elastic constants. The equation takes into account, as in the rule of mixture, the volume fraction of the phases and their elastic constants. But it also considers the aspect ratio of the filler. The aspect ratio of a 2D particle is defined as the ratio between the width over the thickness whereas for 1D particle it is the ratio between the length over the diameter. Two main assumptions of this model are that there is perfect stress transfer between the filler and the polymer (i) and that all particles sizes are equal (ii).

The equation can be written as:

$$\frac{E_c}{E_m} = \frac{1+\zeta\eta\varphi_f}{1-\eta\varphi_f} \qquad 3.3$$

with

$$\eta = \frac{\left(\frac{E_f}{E_m} - 1\right)}{\left(\frac{E_f}{E_m} + \zeta\right)} \qquad 3.4$$

where E_c, E_f and E_m are the composite, filler and matrix Young's modulus respectively. And where φ_f is the volume fraction of the filler and ζ is a shape factor.

The shape factor can be defined by the geometry of the particle and by the modulus calculated. It is defined as follow in Table 3.1:

Table 3.1: Value of the shape factor ζ in function of the particle geometry and the modulus calculated and described in Figure 3.1.

	1D	**2D**
$\mathbf{E_{11}}$	2	2/3 l/t *
$\mathbf{E_{22}}$	2	2/3 l/t *

$\mathbf{E_{33}}$	2 l/d	2

* Traditionally [4], in the case of *unidirectionally oriented platelets*, ζ is taken as 2 *l/t* (length / thickness). However, this factor leads to an overestimation. The shape factor is therefore corrected and defined as $\zeta = \frac{2}{3}\frac{l}{t}$ [8].

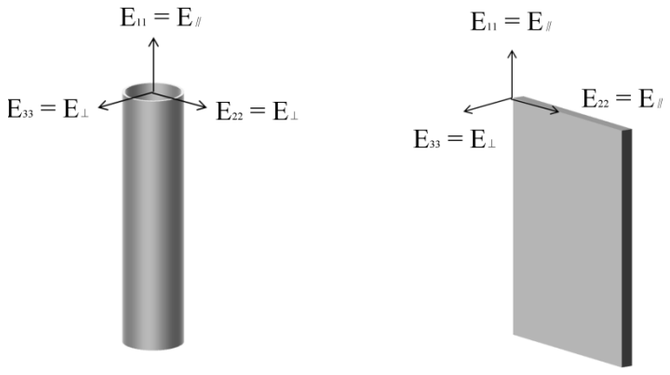

Figure 3.1: Conventional planes for 1D tube and 2D platelet.

In the case of *unidirectionally oriented fillers,* the Young's modulus is defined as:

$$E = E_{11} \qquad 3.5$$

However, the elastic properties of a non-aligned composite can be estimated by simple approximations [8].

In the case of *2D randomly oriented fillers*, i.e. the particles are randomly oriented in the plane of the sheet, the Young's modulus is defined as:

$$E_{2D\ random} = 0.375\ E_{\parallel} + 0.625\ E_{\perp} \qquad 3.6$$

Whereas, in the case of *3D randomly oriented fillers*, the Young's modulus is defined as:

$$E_{3D\ random\ fibre} = 0.184\ E_{\parallel} + 0.816\ E_{\perp} \qquad 3.7$$

or

$$E_{3D\ random\ platelets} = 0.49\ E_{\parallel} + 0.51\ E_{\perp} \quad 3.8$$

$E_{\parallel}$ corresponds to the modulus of the composite parallel to the particles plan i.e. E_{11} for fibres and E_{11} or E_{22} for platelets. Whereas $E_{\perp}$ corresponds to the modulus perpendicular to the particles plan i.e E_{22} or E_{33} for fibres and E_{33} for platelets.

3.3. Graphene for mechanical reinforcement of nanocomposites

3.3.1 Mechanical properties of graphenes

As with SWNTs, graphene sheets exhibit exceptional mechanical properties. The modulus measured by bending test is 1.0 TPa [9], which fits with theoretical simulations [10] and is in the same range as SWNTs. The intrinsic strength has been measured in bending at around 130 GPa, with a breaking strength of ~40 N.m $^{-1}$ [9]. However, experimentally the strength of graphene obtained by common production methods, i.e. by reduction, CVD, etc, is weaker than that of pristine graphene. The modulus of suspended chemically reduced graphene, for example, has been measured to be only ~250 GPa for reduced GO [11]. Mechanical modelling of GO has suggested that oxidation processes could lead to stiffening of the graphene structure compared to a reduced graphene sheet by oxygen bridges between the carbon-atoms and a local rigidification of the C-C bond [12]. However, AFM study found the Young's modulus of GO to be ~207 GPa only [13]. Also, the fracture load of graphene obtained by CVD is found to be an order of magnitude lower than for pristine graphene. This reduction is associated to grain boundaries which weaken CVD graphene flakes [14].

As observed in Table 3.2, the Young's modulus measured for graphene can dramatically vary in relation to the number of layers or functionalisation of the sheets. Indeed, it is worth noting that the Young's modulus of GO or reduced GO more resembles the Young's modulus of clay (~200 GPa) [15], rather than the Young's modulus of single layer graphene (~1000 GPa). The same remark can be made for single layer graphene versus several layers graphene.

Table 3.2: Experimental Young's modulus of different graphene platelets.

	Production method	**Young's modulus (GPa)**	**Measurement method**	**Ref**
Graphene layer	Mechanical cleavage	1 000 ± 100	Indentation	[9]
Graphene layer	Mechanical cleavage	~ 1 000	Raman	[16]
Bi-layers	-	~ 1 000	-	[16]
Tri-layers	-	~ 850	-	[16]
> 7 layers	-	~ 500	-	[16]
< 5 layers	Mechanical cleavage	~ 500	Indentation	[17]
Graphene Oxide	Hummers method	208 ± 23	-	[13]
Bi-layers GO	-	224 ± 18	-	[13]
Tri-layers GO	-	229 ± 27	-	[13]
Reduced GO	Chemically reduced	250 ± 150	Indentation	[11]

3.3.2 Mechanical properties of graphene nanocomposites

In general the tensile properties of nanocomposites are improved with filler loading, dispersion, alignment, aspect ratio and the ration of filler to matrix mechanical properties. Table 3.3 shows some mechanical improvements reported for nanocomposites depending on the aspect ratio, functionalisation, processing and dimensionality of the filler. The effective modulus of the graphene based nanofillers is the modulus of the graphene platelets back-calculated from Equation 3.3 based on experimental data. In case the effective modulus equals the intrinsic modulus (Table 3.2), the reinforcing efficiency of the nanofiller in the composite is very high at 100%. On the other hand if the effective modulus is lowered, it indicates that the platelets are not fully reinforcing the nanocomposite.

To achieve good mechanical reinforcement, graphene nanocomposites like other nanocomposites need to exhibit good dispersion [1] but also good stress transfer between the graphene and the polymer matrix to transfer the load to the filler. Typically, stress transfer between polymers and graphene is found to be relatively weak. For instance, the interfacial shear stress measured at low strains is only ~2 MPa [18], while it drops down to 0.25 MPa at higher strains [19], which is indicative of poor interfacial adhesion at the graphene/polymer interface. From molecular simulations the shear strength between CNT and polyethylene is estimated at 2 MPa in the case of van der Waals bonding only [20]. Experimentally reported shear strengths for nanocomposites possessing poor polymer/filler interactions are below 10 MPa as in the case of polyethylene/MWNT nanocomposites [21]. From molecular simulations, it is also found that the interfacial shear strength of graphene

based nanocomposites is comparable with experimentally measured values for CNT based nanocomposites [22].

Surface functionalisation of graphene sheets with functional groups is one way to enhance the shear strength of the graphene/polymer interface [23]. By covalently bonding PS to graphene, for example, Fang et al. [24] showed an improvement of the Young's modulus of 57 % for very low aspect ratio platelets (20 to 40 nm). The H-bonding between the reduced GO and the polar groups of the polymer matrix also highly improved stress transfer and hence mechanical properties.

An improvement of 940 % in Young's modulus and 150 % in tensile strength has been obtained for solution mixed PVA/reduced GO followed by the reduction of GO via hydrazine solution [25]. Ramanathan et al. [26] obtained an improvement of 33 % in Young's modulus for PMMA/FGS nanocomposite at 0.01 wt.%. This value is much higher than the expected value based on composite theory which predicted only a 5 % increase in stiffness. By mixing reduced GO and epoxy, Rafiee et al. [27] observed that the mechanical properties of these reduced GO/epoxy nanocomposites out-performed those of CNT, as presented in Table 3.3. Interestingly they also demonstrated that reduced GO is the only filler whose properties outperform predictions made by the Halpin-Tsai model. Unfortunately, such an increase in stiffness is often associated with an embrittlement effect [28, 29], as shows in Figure 3.2

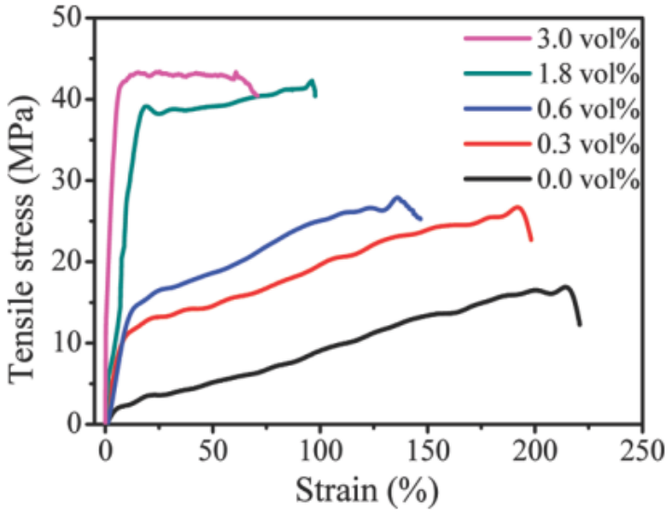

Figure 3.2: Stress–strain curves of PVA / reduced GO [25]

However, by functionalising the GNP with sodium dodecyl benzene sulfonate (SDBS) for HDPE nanocomposite, Wang et al. [30] observed an increase of up to 290 % in elongation at break at a loading at 10 wt.% of GNP. Nevertheless, also this system showed a reduction in elongation at break when this loading was further increased.

The toughness, impact strength and fatigue behaviour of graphene based nanocomposites can also be improved with 2D graphene [27, 31-39]. Nanocomposite toughness based on 2D fillers, for example, could be expected to outperform other dimensionalities because 2D particles enhance the tortuosity when a crack propagates. Addition of graphene at a very low loading (less than 1 wt.%, in general) can significantly improve the toughness of graphene nanocomposites [27, 34, 35]. For example, the fracture toughness of graphene nanocomposites was increased by nearly 100 % at 0.6 wt.% loading by covalently bonded long amine chains [35]. Crack propagation of graphene nanocomposites is also found to improve compared to CNT nanocomposites especially at high stress intensity factor amplitudes [27].

The toughness mechanism is attributed to crack deflection instead of crack bridging as in the case of CNTs. However, a reduction in toughness is observed at higher graphene content [31, 34, 37] due to the associated agglomeration effect of nanoparticles at higher loadings. Fatigue life of composites was also improved by the addition of GO [40] and graphene [27, 33, 41] and outperforming CNT [27, 33]. This outstanding performance is believed to be due to the two dimensional geometry, and crack deflection mechanism [41].

Table 3.3: Mechanical properties of graphene based nanocomposites; the effective modulus is back-calculated using the Halpin-Tsai model [4] and in accordance with [8].

	Processing	**Loading (vol. %)**	**Aspect ratio (l/t)**	**Experimental Young's Modulus (GPa)**	**Effective Modulus Random (E_{33} Graphene) (GPa)**	**Effective Modulus Aligned (E_{11} Graphene) (GPa)**	**Ref**
Epoxy-TRG	In-situ Pol.	0.11	1670	3.74	3450	1090	[27]
PVA-CRG	Solution	1.8	1880	1.04	660	88	[25]
PEN-TRG	Melt mixing	0.6	280	2.70	1100	120	[42]
PEN-GNP	Melt mixing	0.6	14	2.54	Ab. Calc.	Ab. Calc.	[42]
PC-TRG	Melt mixing	0.53	452	2.22	100	38	[43]
PC-GNP	Melt mixing	0.5	4	2.16	150	34	[43]
PS-CRG	Covalent bonding	0.43	60	2.28	Ab. Calc.	Ab. Calc.	[24]
Epoxy-Graphene	In-Situ Pol.	1.3	2940	3.35	101	54	[32]
PP latex-CRG	Melt mixing	0.42	1340	1.76	587	220	[44]
PS-CRG	Solution	0.34	460	2.26	655	205	[45]
PVA-GO	Solution	0.41	3125	3.45	764	350	[46]

PVA-CRG	Solution	0.7	1000	5.8	590	272	[47]
PP-GNP	Melt mixing	0.5	1000	4.5	Ab. Calc	290	[48]
PP-GNP	Melt mixing	0.5	1500	3.9	120	50	[48]
PP-GNP	Melt mixing	1	2500	1.87	Ab. Calc.	255	[49]

3.3.3 1D versus 2D, the effect of the dimensionality

Despite the fact that intrinsic properties of a pristine single graphene sheet are similar to a SWNT, it might out-perform them in nanocomposite applications because the surface in contact with the polymer is higher i.e. the matrix interacts with both graphene surfaces in the case of graphene while only with the outer surface in the case of hollow SWNTs.

Stress transfer in CNT or graphene based nanocomposite can be related to the stress transfer at the polymer/wall interface or in the case of multilayers stress transfer at the wall/wall interface. Raman spectroscopy can be used to monitor the level of stress transfer in CNTs or graphene sheets [50]. Recent works have studied the mechanical behaviour of a single layer of graphene sheet embedded in a polymer matrix. A permanent wrinkling as a (residual) “compressive” pre-strain has been observed in deposited flakes embedded in a polymer matrix [51, 52]. When the sheet is subjected to tension, the initial strain leads to a straightening of the sheet. Upon further loading the sheet is then loaded in tension [51].

Based on bending experiments on an embedded flake which introduced a compressive stress into a graphene sheet, Frank et al. [52] showed that at a constant compressive strain (-0.3 %), this strain leads to a non-uniform strain distribution along the embedded sheet. This non-uniformity is associated to the permanent wrinkles of graphene and its environment (close to graphite flake). However, upon applying a tensile load on the embedded graphene sheet, the strain along the flake appears initially to be uniform at low strains but non-uniform at higher strains (> 0.8 %) [18, 19]. This is an indication that the graphene/polymer interface breaks down at higher strain, and after relaxing the flake, the strain distribution even at low strains remains non-uniform [19], as shown in Figure 3.3.

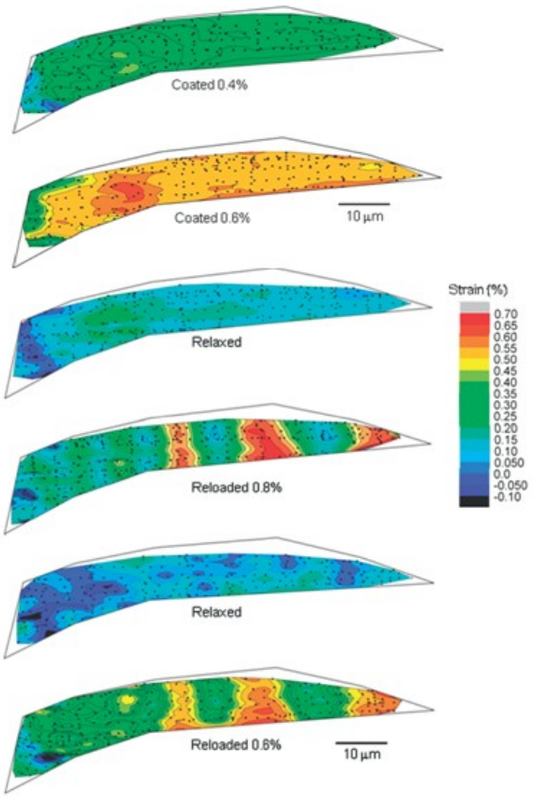

Figure 3.3: Strain maps of a coated graphene flake after tensile cyclic loading at different level of loading, at 0.4 %, 0.6 % strain, in relaxed state, and reloaded at 0.8 % and 0.6 % strain [19].

To better understand the advantages of graphene (2D) compared to CNT (1D) as reinforcement for polymer composites, the effective modulus (E_c/E_m) against the filler aspect ratio is plotted, in Figure 3.4, for a random state (a) and an aligned state (b). The expected Young's modulus of the nanocomposites is calculated using the Halpin-Tsai model, Equation 3.3, and in accordance with [8], for a polymer with a Young's modulus of 1 GPa filled with 1 vol.% of circular platelets or fibres with an intrinsic modulus of 1TPa.

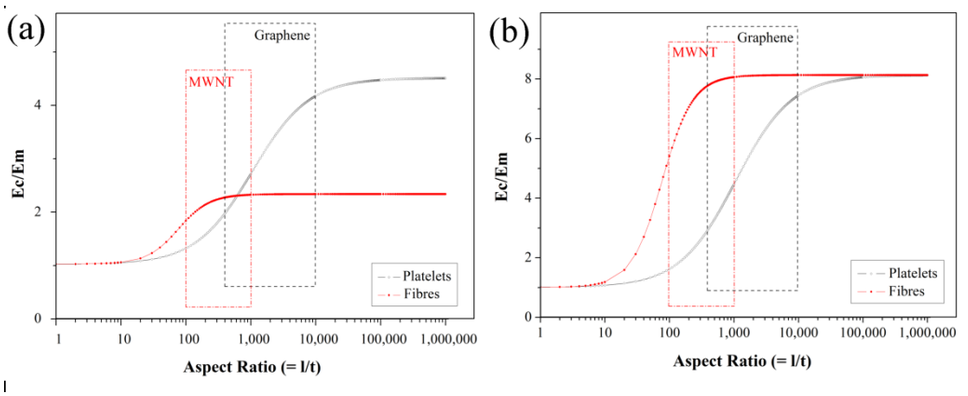

Figure 3.4: Theoretical reinforcement of 1 vol.% of fibre-like and circular platelet-like fillers: (a) unidirectionally oriented and (b) randomly oriented according to the Halpin-Tsai model [4]. The boxes indicate the values expected for graphene (black) and MWNTs (red).

It is interesting to note that in both cases, random and aligned state and for both particles, 2D or 1D, the reinforcement is strongly related to the aspect ratio of the particles. There is a minimum aspect ratio needed for both types of particles to reinforce the nanocomposite. Below this minimum the particles do not participate in the reinforcement. Above this minimum, the reinforcement increases together with the aspect ratio until finally reaching a plateau. This plateau, in the case of aligned nanocomposites corresponds to the Voigt-type rule of mixture prediction.

In Figure 3.4 a, the Young's modulus is compared for both fillers, when they are randomly aligned along the loading direction. As observed, the maximum reinforcement of platelet-like fillers is considerably higher than for fibre-like fillers. However, interestingly fibre-like filler reaches the plateau at lower aspect ratio. Hence, it can be concluded that platelet-like fillers are favourable for ultimate properties in randomly oriented nanocomposites, which is the most common orientation in traditional polymer processes like injection moulding. However, it is

worth noting that maximum reinforcement for 2D platelets is obtained at an aspect ratio ~100 000. This means that if we consider platelets of 1 nm thick, the minimum diameter needed to achieve maximum reinforcement is about ~100 μm. This aspect ratio is much higher than typical aspect ratios for traditionally produced graphene as is highlighted by the black box in Figure 3.4.

The reinforcement template is quite different when the particles are unidirectionally aligned along the loading direction (Figure 3.4 b). Despite ultimate reinforcement for both fillers is similar, it is interesting to note that fibre-like fillers reaches their maximum reinforcement at a much lower aspect ratio, i.e. ~1 000 compared to ~100 000 for 2D filler. Hence, fibres appear to be much more effective reinforcements than platelets when aligned.

3.4. Optimisation of the mechanical reinforcement

Increasing the loading percentage is one of the simplest ways in theory to increase the mechanical properties of a composite. Based on the rule of mixture, Equation 3.1 the Young's modulus increases linearly with the volume fraction of the filler. From this, it is interesting to note that nanocomposites typically are based on very low nanofiller loadings, often below 1 vol.%. The reason for this being that increasing filler loadings lead to agglomeration and a reduced dispersion, which is often associated with a drop of the overall mechanical properties.

To illustrate this phenomenon, the contribution of the graphene to the mechanical properties of various nanocomposites reported in the literature is plotted as a function of loading in Figure 3.5 and summarized in Table 3.3. For this the effective

graphene modulus contributions in the nanocomposites are back-calculated using the Halpin-Tsai model [4]. As expected and similar to most CNT or nanoclay based nanocomposites, the contribution of any graphene-like particle is greater at low volume fractions as it reduces the formation of agglomerates (which effectively lowers their aspect ratio as well as their intrinsic mechanical properties). Interestingly, if the effective reinforcement of GO and reduced GO is plotted, there is no obvious effect of the level of interactions. As reported previously, reduced GO [53, 54] have some functional groups on the graphene sheet which could improve interfacial interactions, potentially leading to better stress transfer.

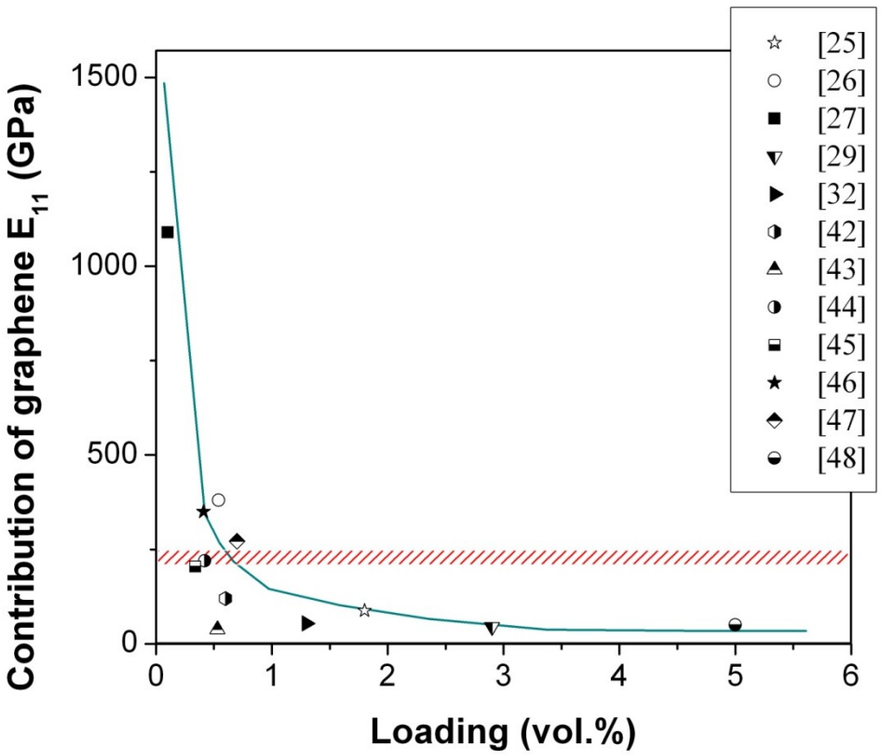

Figure 3.5: Contribution of graphene in assumed aligned state as a function of graphene loading [25-27, 29, 32, 42-48]. The red sparse bar represents the intrinsic Young's modulus of GO and r-GO filler (Ef_{theo} of GO = 250 MPa [11] and Ef_{theo} of r-GO = 207MPa [13], while the blue solid line represent the data trend line.

It is interesting to note that several studies [26, 27, 46, 47] present a filler contribution which is greater than the intrinsic Young's modulus of the filler itself. This means that the overall composite reinforcement is the result of the addition of GO particles but also due to an additional matrix contribution as a result from a change in the polymer morphology. Smaller aspect ratio nanoplatelets can potentially nucleate a polymer matrix and/or orient the polymer crystal, and alter the crystallinity of the matrix. Since nanocomposite are mainly composed of polymeric matrix, a relatively small change in polymer structure and its intrinsic mechanical properties will strongly affect the nanocomposite's response [1]. Clearly, these matrix effects can lead to erroneous values for back calculated nano-platelet stiffness values.

One of the advantages of 2D graphene compared to 1D CNT, is that graphene cannot be entangled due to its dimensionality. Hence the loading can be increased toward higher values without dramatically increasing the polymer viscosity [55]. This could be beneficial in achieving nanocomposites with higher filler loadings. However, in nanocomposites based on nano-platelets, there is a physical limit of packing. This limit is dependent on the size of the polymer coils and the aspect ratio of the particles and decreases as the aspect ratio increases. According to Drzal's group [56] (Figure 3.6) the maximum packing of graphene in a polymer matrix for 1 nm platelets with a lateral size around 200 μm is only ~9 vol.% in the case of an average polymer coil diameter of 10 nm. On the other hand, under the same conditions but with a platelets of 10 nm thick, the maximum packing rises to ~49 vol.%.

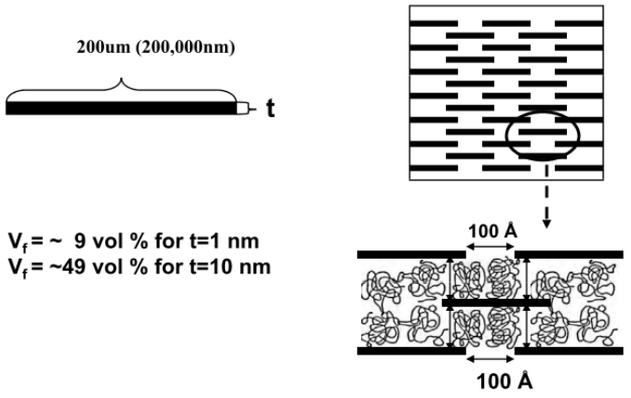

Figure 3.6: Maximum packing of graphene sheets with different platelet thicknesses [56].

At an equivalent width, however, increasing the thickness leads automatically to a reduction of the aspect ratio. By comparing graphite composites with GNP, the mechanical properties of the GNP nanocomposite are found to be higher than those based on graphite filler. For example, an improvement of 105 % in Young's modulus at a loading of 2.5 wt.% is reported for PP-GNP nanocomposites; whereas for PP-graphite composites the improvement is only 43 % at 2.8 wt.% [49]. This is in accordance with composite theories such as Halpin-Tsai model [4] and Mori-Tanaka model [57], which predict that Young's modulus increases with loading and with aspect ratio.

Increasing the thickness of the graphene nanofiller means having a stack of graphene layers. Despite its high intrinsic mechanical properties, graphene sheets are also well known for their self-lubricating behaviour as the basal-plane shear modulus of graphite is low [58]. This effect allows graphene layers to slide in the case of multiple sheets, which - similar to MWNTs - can significantly reduce the stress transfer and nanotube efficiency in nanocomposites. Based on double walled carbon nanotube studies [59], it is shown that the inner wall in these tubes carries less stress

than the outer wall during both compression and tensile loading. This effect points out the poor stress transfer at the wall/wall interface of graphitic nanomaterials like MWNTs and thus also the limits of the reinforcement efficiency of other multilayer carbon based nanocomposites [59, 60]. The stress transfer (or the effective Young's modulus) between mono to a few layer of graphene coated in epoxy resin is studied by Gong et al. [16] by measuring the stress-induced Raman band shift during the deformation and presented in Figure 3.7 a). They found that the stress transfer for a bi-layer is equivalent to a mono-layer, while it decreases by 15 % for a tri-layer. With more than 7 layers, the stress transfer is already effectively halfed. In this study the maximum volume packing is also calculated according to the polymer thickness. Based on these results, they predicted the maximum achievable reinforcement according to the number of layer of graphene, the effective Young's modulus as well as the volume packing as shown in Figure 3.7 b).

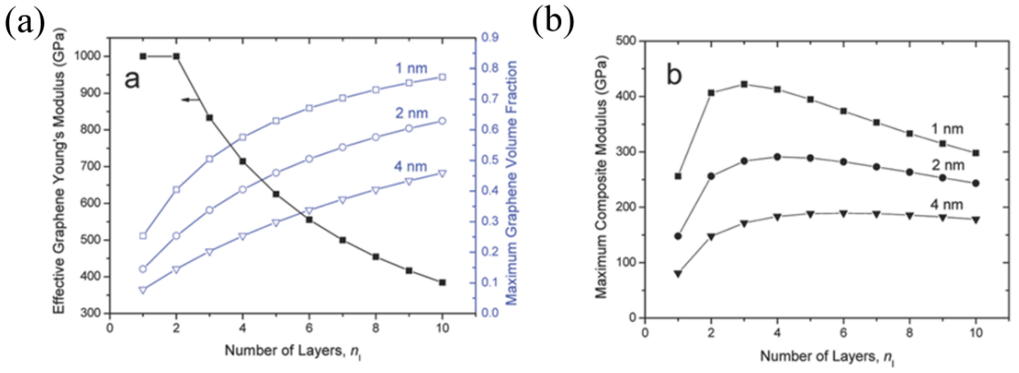

Figure 3.7: (a) Evolution of the effective Young's modulus and maximum packing for a polymer of 1 to 4 nm thick according to the number of graphene layers. (b) Prediction of the maximum nanocomposites modulus based on the number of graphene layers [16].

For instance, if the polymer coil thickness is 1 nm, the "ideal" thickness for an optimal mechanical reinforcement is 3 layers. However if the polymer thickness is 4 nm, the "ideal" thickness is 4 layers and above. It is important to note that this is based on the stress transfer during the elastic behaviour which might be different during plastic behaviour. Also it assumes that the platelets are infinitely long.

A question arises: how long graphene platelets need to be to effectively reinforce a nanocomposite? From a stress-transfer point of view, Gong et al. [18] proposed a critical length of 30 μm for a monolayer to achieve efficient stress transfer based on Raman measurement. However, as pointed out, the diameter of exfoliated graphene in practice hardly exceeds a few microns indicating ineffective reinforcement for the majority of sheets. On another hand, in compression, a higher critical buckling strain is obtained for the shorter monolayers [52]. Also from a stiffness point of view, and as discussed previously based on the Halpin-Tsai model, bigger (longer) platelets have a higher aspect ratio which leads to a better reinforcement.

A disadvantage of very high aspect ratio graphene sheets can be their flexibility. Graphene is a very flexible sheet [61, 62] and several studies report that graphene adapts its morphology to the substrate texture [63-65]. The polymer mobility can also modify the graphene morphology. For example, in a model study, Li et al. [66, 67] showed that polymer mobility lead to modifying the graphene morphology from a single layer into folded layers. By comparing melt-compounded GNP nanocomposites with the same platelet thickness (~10 nm) but with two different diameters, i.e. 1 and 15 μm, Kalaitzidou et al. [48, 68] showed that higher aspect ratio particles could lead to a lower mechanical reinforcement, which contradicts traditional composite theories. For instance, at 3 vol.%, melt-mixed PP-GNP

nanocomposites, exhibited a Young's modulus of ~1.4 GPa and ~1.8 GPa for GNPs with an diameter of 15 and 1 μm, respectively [68]. They observed that high aspect ratio GNPs fold and scroll as shown in Figure 2.7, resulting in a decrease in filler efficiency due to this reduced aspect ratio [68]. It's worth noting that GNPs are platelets of more than 10 layers of graphene. The effect previously described might be even more amplified for single layer graphene.

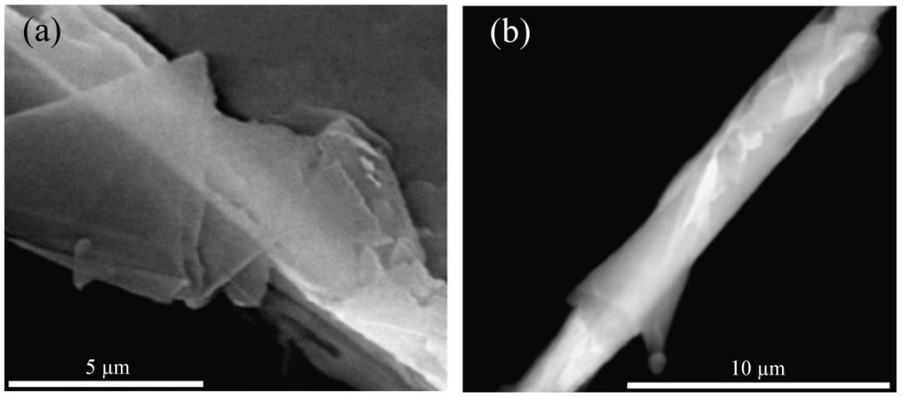

Figure 3.8: ESEM image of GNP (10 nm thickness, 15 μm diameter) (a) folded and (b) scrolled [68].

As mentioned earlier, the maximum volume fraction, aspect ratio, orientation, surface functionalization, number of layers, and the width or diameter are all parameters that can either promote or inhibit the reinforcement efficiency of nanoplatelets. However, in order to insure good reinforcement the structure of nanocomposites needs to be controlled during processing, filler loading needs to increased while avoiding any agglomeration as well any buckling, scrolling or other changes in the graphene structure which could reduce their aspect ratio. Finally, in order to achieve good stress transfer the filler needs to have a surface chemistry compatible with that of the polymer matrix.

3.5. Hierarchical nanocomposites

The intrinsic limit to nanoplatelet loading in polymer nanocomposites emphasises the need for polymer chains to be absorbed onto these surfaces and manufacturing techniques to create high volume fraction nanocomposites with good control of the nanosheet morphology.

The layer-by-layer technique is a bottom-up approach leading to highly hierarchical structured nanocomposites. These bio-inspired systems are often compared to nacre and are expected to improve the tensile strength and ductility of highly loaded nanocomposites. The most well-known process used is dip coating. This process consists of dipping a substrate repeatedly into two solutions (polymer & filler). The layers are maintained on the substrate by strong attractive forces. The first successful LbL nanocomposite was produced by Podsiadlo et al. [69] and was made of 200 bi-layers of PVA-clay. Cross-linked, the LbL composites had its strength improved by a factor of 10 and its Young's modulus comparable to Kevlar, i.e. ~106 GPa. GO LbL was also produced by dip-coating where GO layer was deposited on polyelectrolyte followed by in-situ reduction [70]. They observed that the conductivity was related to the roughness of the substrate by reducing the in-plane contact between the GO. Another method implies the functionalization of graphene surfaces with polyelectolyte. Here, the wafer is alternatively coated with positively and negatively grafted polyelectolyte [71]. The deposition of layer-by-layer of polymer-GO is also possible with weaker bonding such as H-bonding. For example, a layer-by-layer PVA-GO nanocomposite constituting of 300 bi-layers by dip coating was fabricated and showed an increase of the Young's modulus and hardness of 99 % and 240 %, respectively [72].

The deposition of a monolayer of reduced graphene can also be achieved by spraying [73] or by Langmuir-Blodgett deposition [74, 75]. Highly filled PVA-GO nanocomposites are also obtained by a vacuum filtration method [76]. The concentration of the GO reached 72 wt.% and lead to a 10 fold increase in Young's modulus. An alignment of the filler is observed perpendicular to the flow axis, similar to GO bucky paper [77]. Flexible and free-standing films are fabricated by vacuum filtration of graphene to obtain graphene bucky paper followed by in-situ electropolymerisation of aniline. These PANI-TRG nanocomposites had a layer-by-layer structure with enhanced mechanical strength by 47 % and electrochemical capacitance by 58 % [78].

Recently Kotov et al. [79] has systematically compared PVA-rGO nanocomposites made from two assembly methods: the LbL via dip-coating and vacuum filtration method. While both methods present a layered structure, LbL showed a better alignment of the reduced GO sheets, a smaller basal spacing and a more effective epitaxial templating of the PVA crystals. These structural modifications lead to improved thermal and electrical properties, while it had no impact on the mechanical properties.

A recent method based on freeze casting of ceramic nanoparticles followed by sintering resulted in homogeneous, layered and porous ceramics [80]. As the ice crystals grow, the ceramic nanoparticles are positioned in the excluded volume created between the ice-crystals. By infiltrating PMMA into these layered ceramics followed by hot-pressing, Munch et al. [81] obtained highly ordered composites with a lamellar structure or brick and mortar structure, respectively as presented in Figure 3.9.

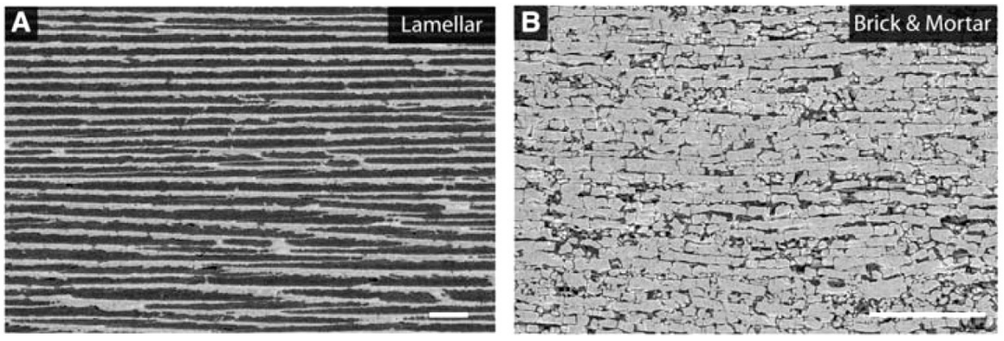

Figure 3.9: Ice-templating of PMMA-Al_2O_3 nanocomposite with (a) a lamellar and (b) a brick and mortar structure [81].

Applied to polymer nanocomposites, a nanocomposite of PVA-rGO with a sponge-like macroporous scaffold was obtained by Vickery et al. [82]. A solution of PVA-rGO was immersed in a liquid Nitrogen bath and a macroporous structure was obtained by a combination of phase separation between the solvent and the nanocomposite associated with the ice crystal growth which positions the polymer and the particles at the boundaries of the crystals.

Several studies showed that nanocomposites based on solution casting of PVA-GO and PVA-rGO can also present a layered structure [25, 83, 84]. For instance, Li et al. [84] made solution cast nanocomposites of PVA-GO with loadings up to 95 wt.%. These nanocomposites present an organised layered structure with improved mechanical properties. This solution casting method presents significant advantages as it is simple and relatively fast compared to other LbL methods.

Post-processing is another method to control filler morphology. For example, Wang et al. [2] showed that solution cast PVA-SWNT films can be drawn into oriented tapes with very high mechanical reinforcement. Here the drawing process allowed the SWNT to align in the polymer matrix, increasing their efficiency. The addition of

0.1 wt% led to an increase of 200 % in tensile strength, which corresponded to a contribution of the SWNT to the nanocomposite strength equivalent to 88 GPa. A bi-component tape with improved mechanical and electrical properties was obtained by controlling the percolating MWNT network [85]. Here, post processing consisted of first drawing the polymer composite, followed by an annealing step as described in the sketch in Figure 3.10. The polymer drawing resulted in the alignment of the MWNT in the polymer matrix, while the annealing step gave the ability for the MWNTs to relax, resulting in an increased local lateral contact between the MWNTs and as a result an increase in electrical conductivity.

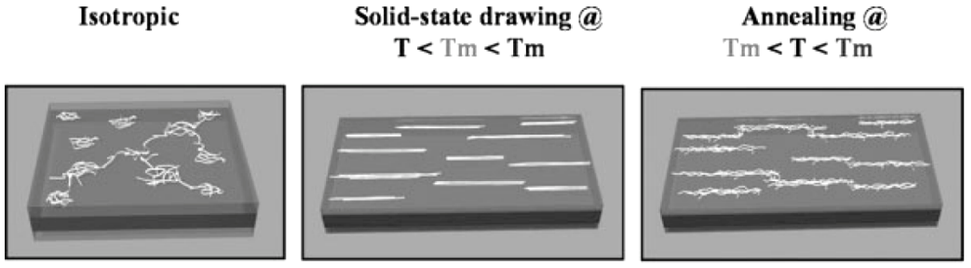

Figure 3.10: Sketch representing the control of the MWNT network through two post processing. Isotropic network of MWNT after melt compounding followed by cold drawing step to align the MWNT bundles and an annealing step to allow dynamic percolation creating contacts between the MWNT bundles [85].

3.6. Conclusions

An overview of the mechanical reinforcement potential of graphene is given. In order to fully exploit graphene for mechanical reinforcement a number of issues need to be addressed:

1. The intrinsic Young's modulus of graphene is highly dependent on the functionalisation and the number of layers. The Young's modulus of graphene is 1 TPa while it drops below 500 GPa for a graphene multilayers of 7 layers or more and 200 GPa for graphene oxide which is comparable to the Young's modulus of clays.
2. The functionalisation of graphene is a way to improve the stress transfer between the polymer and the sheets as the interfacial shear stress between graphene and polymer is typically very weak.
3. To optimise the mechanical reinforcement of nanocomposites, the filler volume fraction needs to be maximized. However, this should be not at the expense of re-agglomeration and there exists a physical limit of the maximum nanoplatelet packing based on the thickness of the platelets and the thickness of the polymer layer.
4. The mechanical properties of nanocomposites are dependent on (i) the aspect ratio of the particles, (ii) the number of layers, (iii) the width, (iv) the volume fraction, (iiv) surface functionalisation and (iiiv) orientation. However many of these parameters counterbalance each other. For instance, if the diameter of the platelets increases, the aspect ratio increases which will improve the reinforcing potential. However it also makes the sheets more flexible, and thus more sensitive to the media. The sheets can be deformed more easily and this will reduce their aspect ratio. On the other hand, if the thickness increases the maximum volume packing increase, the sheets are less flexible, but their intrinsic modulus will be reduced, as well as their aspect ratio, which in turn will reduce their reinforcing potential

5. The ability of the graphene sheets to wrinkle, fold or scroll, due to their flexibility, highly reduces the efficiency of graphene sheets in nanocomposites. Recent works point out that graphene embedded in a polymer is under residual strain. During mechanical loading, the initial strain will straighten the sheet followed by tensioning of the sheet. It is also noticed that during melt mixing or compounding high aspect ratio platelets are susceptible to buckling or scrolling as a result of their high flexibility, leading to an effective reduction in aspect ratio and mechanical reinforcement efficiency. Both of these examples show how much the morphology of graphene flakes (and thus, nanocomposite properties) is sensitive to processing. Therefore other methods than melt mixing based on self-assembly such as layer-by-layer, ice templating, casting, spraying are of interest as a way to create hierarchical and highly organized structures in which the graphene morphology will be preserved. Besides the use of such bottom-up approaches, more traditional polymer processes such as the use of high shear or elongational flow fields should also be exploited to create highly organised well aligned platelet based nanocomposites. Post-processing processes such as uniaxial or biaxial stretching of film should be investigated as a way to create highly structured graphene nanocomposites.

To conclude, graphene based nanocomposites are a source of great expectations. Recent studies are very promising and show great improvements especially at low loadings. However, graphene also offers great challenges especially in the area of processing, as these flat 2D nanofillers of high aspect ratio need to be organised similar to hierarchical biocomposites as found in Nature.

3.7. References

1. Ciselli, P., Wang, Z., and Peijs, T., Materials Technology, 2007. **22**: p. 10-21.
2. Wang, Z., Ciselli, P., and Peijs, T., Nanotechnology, 2007. **18**(45).
3. I.M. Ward, D.W. Hadley, ed. J.W. Sons. 1993.
4. Halpin, J.C. and Kardos, J.L. , Polymer Engineering and Science, 1976. **16**(5): p. 344 - 352.
5. Eshelby, J. D. Vol. 241. 1957. 376-396.
6. Tandon, G. P. and Weng, G. J., Polymer Composites, 1984. **5**(4): p. 327-333.
7. Kelly, A. ; Macmillan, N.H. 1986: Oxford : Clarendon.
8. Van Es, M, Technology University Delft, 2001
9. Lee, Changgu, Wei, Xiaoding, Kysar, Jeffrey W., and Hone, James, Science, 2008. **321**(5887): p. 385-388.
10. Sakhaee-Pour, A., Solid State Communications, 2009. **149**(1-2): p. 91-95.
11. Gómez-Navarro, Cristina, Burghard, Marko, and Kern, Klaus, Nano Letters, 2008. **8**(7): p. 2045-2049.
12. Incze, Andrei, Pasturel, Alain, and Peyla, Philippe, Physical Review B, 2004. **70**(21): p. 212103.
13. Suk, Ji Won, Piner, Richard D., An, Jinho, and Ruoff, Rodney S., ACS Nano, 2010. **4**(11): p. 6557-6564.
14. Huang, Pinshane Y., Ruiz-Vargas, Carlos S., van der Zande, Arend M., Whitney, William S., Levendorf, Mark P., Kevek, Joshua W., Garg, Shivank, Alden, Jonathan S., Hustedt, Caleb J., Zhu, Ye, Park, Jiwoong, McEuen, Paul L., and Muller, David A., Nature, 2011. **469**(7330): p. 389-392.
15. Bilotti, Emiliano, School of Engineering and Materials Science, Queen Mary, University of London, 2009
16. Gong, Lei, Young, Robert J., Kinloch, Ian A., Riaz, Ibtsam, Jalil, Rashid, and Novoselov, Kostya S., ACS Nano, 2012. **6**(3): p. 2086-2095.
17. Frank, I. W., Tanenbaum, D. M., Zande, A. M. van der, and McEuen, P. L. *Mechanical properties of suspended graphene sheets*. 2007: AVS.
18. Gong, L., Kinloch, I. A., Young, R. J., Riaz, I., Jalil, R., and Novoselov, K. S., Advanced Materials, 2010. **22**(24): p. 2694-2697.
19. Young, Robert J., Gong, Lei, Kinloch, Ian A., Riaz, Ibtsam, Jalil, Rashed, and Novoselov, Kostya S., ACS Nano, 2011. **5**(4): p. 3079-3084.
20. Frankland, S. J. V., Caglar, A., Brenner, D. W., and Griebel, M., The Journal of Physical Chemistry B, 2002. **106**(12): p. 3046-3048.
21. Barber, Asa H., Cohen, Sidney R., and Wagner, H. Daniel, Applied Physics Letters, 2003. **82**(23): p. 4140-4142.
22. Amnaya, P. Awasthi and et al., Modelling and Simulation in Materials Science and Engineering, 2009. **17**(1): p. 015002.

23. Lv, Cheng, Xue, Qingzhong, Xia, Dan, Ma, Ming, Xie, Jie, and Chen, Huijuan, The Journal of Physical Chemistry C, 2010. **114**(14): p. 6588-6594.
24. Fang, Ming, Wang, Kaigang, Lu, Hongbin, Yang, Yuliang, and Nutt, Steven, Journal of Materials Chemistry, 2009. **19**(38): p. 7098-7105.
25. Zhao, Xin, Zhang, Qinghua, Chen, Dajun, and Lu, Ping, Macromolecules, 2010. **43**(5): p. 2357-2363.
26. Ramanathan, T., Abdala, A. A., Stankovich, S., Dikin, D. A., Herrera-Alonso, M., Piner, R. D., Adamson, D. H., Schniepp, H. C., Chen, X., Ruoff, R. S., Nguyen, S. T., Aksay, I. A., Prud'homme, R. K., and Brinson, L. C., Nature Nanotechnology, 2008. **3**(6): p. 327-331.
27. Rafiee, Mohammad A., Rafiee, Javad, Wang, Zhou, Song, Huaihe, Yu, Zhong-Zhen, and Koratkar, Nikhil, ACS Nano, 2009. **3**(12): p. 3884-3890.
28. Zheng, W., Lu, X. H., and Wong, S. C., Journal of Applied Polymer Science, 2004. **91**(5): p. 2781-2788.
29. Kim, Il-Hwan and Jeong, Young Gyu, Journal of Polymer Science Part B: Polymer Physics, 2010. **48**(8): p. 850-858.
30. Wang, Liwei and Chen, Guohua, Journal of Applied Polymer Science, 2010. **116**(4): p. 2029-2034.
31. Rafiq, Rehman, Cai, Dongyu, Jin, Jie, and Song, Mo, Carbon, 2010. **48**(15): p. 4309-4314.
32. Zaman, Izzuddin, Phan, Tam Thanh, Kuan, Hsu-Chiang, Meng, Qingshi, Bao La, Ly Truc, Luong, Lee, Youssf, Osama, and Ma, Jun, Polymer, 2011. **52**(7): p. 1603-1611.
33. Yavari, F., Rafiee, M. A., Rafiee, J., Yu, Z. Z., and Koratkar, N., ACS Applied Materials & Interfaces, 2010. **2**(10): p. 2738-2743.
34. Rafiee, M. A., Rafiee, J., Yu, Z. Z., and Koratkar, N., Applied Physics Letters, 2009. **95**(22): p. 223103-3.
35. Fang, Ming, Zhang, Zhen, Li, Jianfeng, Zhang, Hongdong, Lu, Hongbin, and Yang, Yuliang, Journal of Materials Chemistry, 2010. **20**(43): p. 9635-9643.
36. Qiu, Jingjing and Wang, Shiren, Journal of Applied Polymer Science, 2011. **119**(6): p. 3670-3674.
37. Khan, Umar, May, Peter, O'Neill, Arlene, and Coleman, Jonathan N., Carbon, 2010. **48**(14): p. 4035-4041.
38. Liu, Qinghong, Zhou, Xufeng, Fan, Xinyu, Zhu, Chunyang, Yao, Xiayin, and Liu, Zhaoping, Polymer-Plastics Technology and Engineering, 2012. **51**(3): p. 251-256.
39. Abdullah, Shivan Ismael and Ansari, M. N. M., HBRC Journal, (0).
40. Bortz, Daniel R., Heras, Erika Garcia, and Martin-Gullon, Ignacio, Macromolecules, 2012. **45**(1): p. 238-245.
41. Rafiee, Mohammed A., Rafiee, Javad, Srivastava, Iti, Wang, Zhou, Song, Huaihe, Yu, Zhong-Zhen, and Koratkar, Nikhil, SMALL, 2010. **6**(2): p. 179-183.

42. Kim, H. and Macosko, C. W., Macromolecules, 2008. **41**(9): p. 3317-3327.

43. Kim, Hyunwoo and Macosko, Christopher W., Polymer, 2009. **50**(15): p. 3797-3809.

44. Song, Pingan, Cao, Zhenhu, Cai, Yuanzheng, Zhao, Liping, Fang, Zhengping, and Fu, Shenyuan, Polymer, 2011. **52**(18): p. 4001-4010.

45. Ren, Peng-Gang, Yan, Ding-Xiang, Chen, Tao, Zeng, Bao-Qing, and Li, Zhong-Ming, Journal of Applied Polymer Science, 2011. **121**(6): p. 3167-3174.

46. Liang, J. J., Huang, Y., Zhang, L., Wang, Y., Ma, Y. F., Guo, T. Y., and Chen, Y. S., Advanced Functional Materials, 2009. **19**(14): p. 2297-2302.

47. Zhou, Tiannan, Chen, Feng, Tang, Changyu, Bai, Hongwei, Zhang, Qin, Deng, Hua, and Fu, Qiang, Composites Science and Technology, 2011. **71**(9): p. 1266-1270.

48. Kalaitzidou, Kyriaki, Fukushima, Hiroyuki, Miyagawa, Hiroaki, and Drzal, Lawrence T., Polymer Engineering & Science, 2007. **47**(11): p. 1796-1803.

49. Wakabayashi, K., Pierre, C., Dikin, D. A., Ruoff, R. S., Ramanathan, T., Brinson, L. C., and Torkelson, J. M., Macromolecules, 2008. **41**(6): p. 1905-1908.

50. Ferralis, Nicola, Journal of Materials Science, 2010. **45**(19): p. 5135-5149.

51. Tsoukleri, Georgia, Parthenios, John , Papagelis, Konstantinos , Jalil, R., Ferrari, A. C., Geim, A. K., Novoselov, Kostya S. , and Galiotis, C., SMALL, 2009. **5**(21): p. 2397-2402

52. Frank, Otakar, Tsoukleri, Georgia, Parthenios, John, Papagelis, Konstantinos, Riaz, Ibtsam, Jalil, Rashid, Novoselov, Kostya S., and Galiotis, Costas, ACS Nano, 2010. **4**(6): p. 3131-3138.

53. Stankovich, S., Dikin, D. A., Piner, R. D., Kohlhaas, K. A., Kleinhammes, A., Jia, Y., Wu, Y., Nguyen, S. T., and Ruoff, R. S., Carbon, 2007. **45**(7): p. 1558-1565.

54. Schniepp, Hannes C., Li, Je-Luen, McAllister, Michael J., Sai, Hiroaki, Herrera-Alonso, Margarita, Adamson, Douglas H., Prud'homme, Robert K., Car, Roberto, Saville, Dudley A., and Aksay, Ilhan A., The Journal of Physical Chemistry B, 2006. **110**(17): p. 8535-8539.

55. Kalaitzidou, K., Fukushima, H., and Drzal, L. T., Carbon, 2007. **45**(7): p. 1446-1452.

56. XGSciences. http://www.xgsciences.com.

57. Cho, J., Luo, J. J., and Daniel, I. M., Composites Science and Technology, 2007. **67**(11-12): p. 2399-2407.

58. Soule, D. E. and Nezbeda, C. W., Journal of Applied Physics, 1968. **39**(11): p. 5122-5139.

59. Cui, Shuang, Kinloch, Ian A., Young, Robert J., Noé, Laure, and Monthioux, Marc, Advanced Materials, 2009. **21**(35): p. 3591-3595.

60. Zalamea, Luis, Kim, Hyonny, and Pipes, R. Byron, Composites Science and Technology, 2007. **67**(15-16): p. 3425-3433.

61. Meyer, Jannik C., Geim, A. K., Katsnelson, M. I., Novoselov, K. S., Booth, T. J., and Roth, S., Nature, 2007. **446**(7131): p. 60-63.

62. Mkhoyan, K. A., Contryman, A. W., Silcox, J., Stewart, D. A., Eda, G., Mattevi, C., Miller, S., and Chhowalla, M., Nano Letters, 2009. **9**(3): p. 1058-1063.

63. Stoberl, U., Wurstbauer, U., Wegscheider, W., Weiss, D., and Eroms, J., Applied Physics Letters, 2008. **93**(5): p. -.

64. Scharfenberg, Scott, Rocklin, D. Z., Chialvo, Cesar, Weaver, Richard L., Goldbart, Paul M., and Mason, Nadya, Applied Physics Letters, 2011. **98**(9): p. 091908.

65. Lui, Chun Hung, Liu, Li, Mak, Kin Fai, Flynn, George W., and Heinz, Tony F., Nature, 2009. **462**(7271): p. 339-341.

66. Li, Qiang, Li, Zhongjun, Chen, Moran, and Fang, Ying, Nano Letters, 2009. **9**(5): p. 2129-2132.

67. Li, Z. J., Cheng, Z. G., Wang, R., Li, Q., and Fang, Y., Nano Letters, 2009. **9**(10): p. 3599-3602.

68. Kalaitzidou, K., Fukushima, H., and Drzal, L. T., Composites Part a-Applied Science and Manufacturing, 2007. **38**(7): p. 1675-1682.

69. Podsiadlo, Paul, Kaushik, Amit K., Arruda, Ellen M., Waas, Anthony M., Shim, Bong Sup, Xu, Jiadi, Nandivada, Himabindu, Pumplin, Benjamin G., Lahann, Joerg, Ramamoorthy, Ayyalusamy, and Kotov, Nicholas A., Science, 2007. **318**(5847): p. 80-83.

70. Kotov, Nicholas A., Dékány, Imre, and Fendler, Janos H., Advanced Materials, 1996. **8**(8): p. 637-641.

71. Shen, Jianfeng, Hu, Yizhe, Li, Chen, Qin, Chen, Shi, Min, and Ye, Mingxin, Langmuir, 2009. **25**(11): p. 6122-6128.

72. Zhao, Xin, Zhang, Qinghua, Hao, Yanping, Li, Yingzhi, Fang, Ying, and Chen, Dajun, Macromolecules, 2010. **43**(22): p. 9411-9416.

73. Gilje, Scott, Han, Song, Wang, Minsheng, Wang, Kang L., and Kaner, Richard B., Nano Letters, 2007. **7**(11): p. 3394-3398.

74. Cote, Laura J., Kim, Franklin, and Huang, Jiaxing, Journal of the American Chemical Society, 2008. **131**(3): p. 1043-1049.

75. Li, Xiaolin, Zhang, Guangyu, Bai, Xuedong, Sun, Xiaoming, Wang, Xinran, Wang, Enge, and Dai, Hongjie, Nat Nano, 2008. **3**(9): p. 538-542.

76. Putz, Karl W., Compton, Owen C., Palmeri, Marc J., Nguyen, SonBinh T., and Brinson, L. Catherine, Advanced Functional Materials, 2010. **20**(19): p. 3322-3329.

77. Dikin, Dmitriy A., Stankovich, Sasha, Zimney, Eric J., Piner, Richard D., Dommett, Geoffrey H. B., Evmenenko, Guennadi, Nguyen, SonBinh T., and Ruoff, Rodney S., Nature, 2007. **448**(7152): p. 457-460.

78. Wang, Da-Wei, Li, Feng, Zhao, Jinping, Ren, Wencai, Chen, Zhi-Gang, Tan, Jun, Wu, Zhong-Shuai, Gentle, Ian, Lu, Gao Qing, and Cheng, Hui-Ming, ACS Nano, 2009. **3**(7): p. 1745-1752.

79. Zhu, Jian, Zhang, Huanan, and Kotov, Nicholas A., ACS Nano, 2013. **7**(6): p. 4818-4829.

80. Deville, Sylvain, Saiz, Eduardo, Nalla, Ravi K., and Tomsia, Antoni P., Science, 2006. **311**(5760): p. 515-518.

81. Munch, E., Launey, M. E., Alsem, D. H., Saiz, E., Tomsia, A. P., and Ritchie, R. O., Science, 2008. **322**(5907): p. 1516-1520.

82. Vickery, Jemma L., Patil, Avinash J., and Mann, Stephen, Advanced Materials, 2009. **21**(21): p. 2180-2184.

83. Xu, Yuxi, Hong, Wenjing, Bai, Hua, Li, Chun, and Shi, Gaoquan, Carbon, 2009. **47**(15): p. 3538-3543.

84. Li, Yuan-Qing, Yu, Ting, Yang, Tian-Yi, Zheng, Lian-Xi, and Liao, Kin, Advanced Materials, 2012. **24**(25): p. 3426-3431.

85. Deng, H., Zhang, R., Reynolds, C. T., Bilotti, E., and Peijs, T., Macromolecular Materials and Engineering, 2009. **294**(11): p. 749-755.

Chapter 4

PC-GNP nanocomposites by melt mixing

4.1. Introduction

Melt compounding is a traditional polymer processing method commonly used in industry. Melt compounding consists of heating the polymer above the melting temperature and mixing under shear. Nanocomposites are produced by mixing the polymer melt with the nanofiller, where dispersion of the filler is obtained by the high shearing forces. This process is the method of choice for industry as it is environmentally friendly, cheap and scalable.

Melt compounding compared to other traditional method to make nanocomposites like solution casting is however often less effective in dispersing nanoparticles [1]. Kim et al. [2] has studied the morphology of graphene sheets into polyurethane matrix under different processing methods by TEM and WAXD. The study reveals that graphene in melt

compounded material consists of oriented sheets with some agglomerates while in solution cast and in in-situ polymerised materials, the graphene sheets consist of randomly oriented "curved thin sheets".

Several studies revealed that the flow during the extrusion process induces orientation of graphene [2, 3], GNP [4, 5] and also CNT [6, 7]. Flow induced orientation of graphene during polymer extrusion is studied by Kim et al. [3]. The study showed that particles start to disorient as soon as the flow stops and is dependent on loading. In diluted systems, the particles disorient easily since there is no contact between the particles, creating an isotropic nanocomposites. As the loading increases, a percolated network is formed. The disorientation is restricted by the particles contact and/or polymer bridging creating oriented nanocomposites.

The advantages of melt compounding graphene nanocomposites compared to CNT based nanocomposites are noticeable. In melt-compounded CNT nanocomposites the loading is dramatically restricted by the CNT entanglements and the high viscosity associated [8]. Entanglement of graphene is not possible due to its dimensionality which allows compounding of nanocomposites with much higher filler concentrations. For instance, Kalaitzidou et al [4] showed that in PP melt-compounded nanocomposites, the maximum loading for carbon nanofibre is reached at 3 – 5 vol.%, while for GNP, a maximum loading could be achieved of 10 vol.%.

As it is discussed in the previous chapter, graphene particles in nanocomposites are promising for mechanical reinforcement. Its chemical structure as well as its dimensionality makes graphene a great candidate, albeit with some challenges. From a mechanical point of view, high aspect ratio fillers are needed to maximise reinforcing efficiency. However, several studies pointed out that in melt compounding high aspect ratio fillers can lead to the lowest

reinforcing efficiency [9, 10]. The 2D structure of high aspect ratio graphene sheets makes them very flexible, leading to folding, scrolling or buckling of the sheets during shear mixing lowering their effective aspect ratio. Thicker particles, like GNP may be less flexible. However, thicker platelets have a lower intrinsic Young's modulus. Gong et al. [11] measured the Young's modulus of multi-layers of graphene and showed that while the Young's modulus of a bi-layer is 1 TPa, the Young's modulus decreases significantly with the number of layers. The Young's modulus of 4 layers and 10 layers, for instance, are measured at around 700 GPa and 400 GPa, respectively.

In this work, polycarbonate nanocomposites filled with GNP are produced. Polycarbonate is selected since it is an amorphous thermoplastic and has excellent mechanical properties, thermal resistance as well as optical transparency. Its high thermal stability prevents from degradation during prolonged melt processing. In addition, PC has a very good compatibility with carbon based particles like graphene. Nanocomposites of 0.5, 1, 2, 3 wt.% GNP are melt compounded by a twin-screw extrusion process. Thermal and mechanical properties are studied and addressed as a function of particle morphology and polymer modification.

4.2. Experimental

4.2.1 Materials

The polymer used in this study is a commercially available polycarbonate, Makrolon OD2015 (Bayer) with a melt volume-flow rate of 16.5 cm^3/10 min at 250 °C and a bulk density of 1.19 g/cm^3. GNPs with an average thickness of 8 nm and diameter < 2 μm are purchased from Cheaptubes (Grade 3).

4.2.2 Preparation

PC pellets and GNP are dried overnight at 80 °C. A 10 wt.% GNP-PC masterbatch is first prepared by melt compounding at 290 °C under nitrogen atmosphere using a DSM 15cc micro compounder. Compounding is performed for 5 min with a screw speed of 100 rpm. Nanocomposite blends are then obtained by diluting this masterbatch with pure PC pellets in different ratios to produce final GNP concentrations of 0.5 wt.%, 1 wt.%, 2 wt.% and 3 wt.%. Compounding is done under the same conditions as for the masterbatch. After melt processing, the extruded blends are stored in a desiccator to prevent moisture absorption. Nanocomposite films are produced by hot-pressing the compounds at 290 °C under 80 bar using a Dr Collin hydraulic press.

4.2.3 Characterization

The glass transition temperature is determined using differential scanning calorimetry characterization (Mettler DSC 822e) using a heating and cooling rate of 10 °C.min^{-1} and 5 ^{o}C.min^{-1}, respectively.

Thermal degradation of the nanocomposites is characterised by thermal gravimetric analysis using a TA Instrument Q500. Samples are heated from 25 ^{o}C to 1000 °C at a rate of 10 °C.min^{-1}. Tests are performed in air-N_2 (60 and 40 mL.min^{-1}, respectively) and nitrogen atmosphere.

Mechanical behaviour is studied by performing tensile tests on the films using an Instron 5586 equipped with a load cell of 1 kN. Samples are prepared and tested according ASTM D882 standard. Parallel strips are cut to the following dimension 70x5mm. A 30 mm gauge length and 20 mm.min^{-1} strain rate are used to perform the tests.

The microstructure is observed using a FEI Inspector-F scanning electron microscope. Samples are observed at a working distance of 10mm and at 5kV. Prior to the measurement the samples are gold coated.

4.3. Results and discussion

4.3.1 Dispersion

The overall properties of nanocomposites are mainly determined by the quality of the dispersion of the particles in the matrix. The dispersion and the quality of the compounds are attested by SEM micrography, as presented in Figure 4.1.

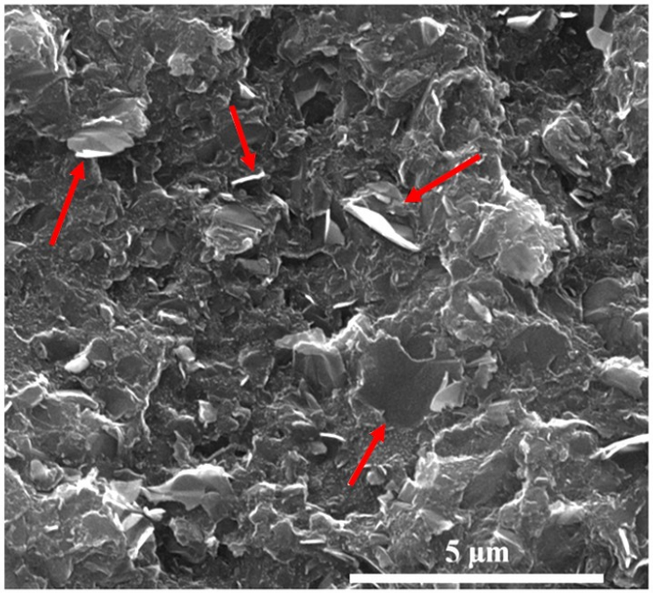

Figure 4.1: GNP dispersed in PC by melt compounding at a loading of 3 wt.% highlighting the random orientation of the GNPs. The arrows point out some GNP particles.

As observed in Figure 4.1, the GNP particles are randomly dispersed in the PC matrix (see arrows). Several studies showed an alignment of graphene particles in melt compounding [3-

5] especially at high loading [3]. Our nanocomposite films are hot-pressed and it is expected that the hot-pressing step probably disrupted any GNP orientation obtained during melt mixing [12, 13]. The morphology of GNP particles is investigated by SEM and presented in Figure 4.2.

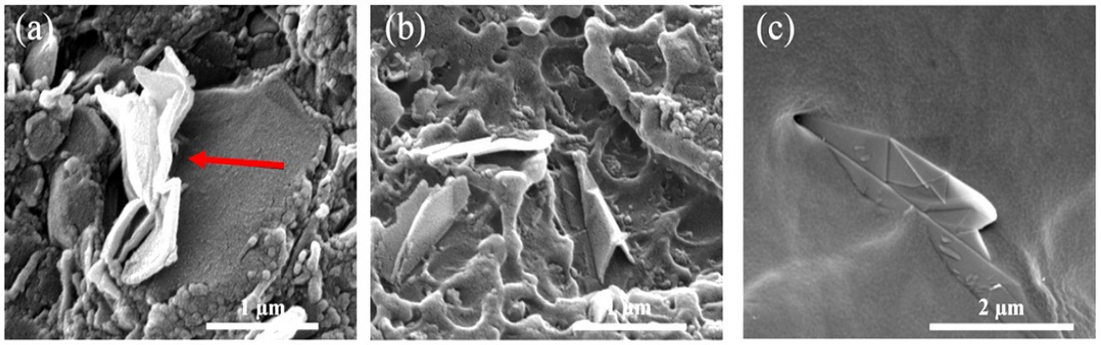

Figure 4.2: Morphology of (a) buckled GNP agglomerates highlighted by the red arrow, (b) bend, and (c) folded GNP particles in melt mixed PC compounds.

Firstly, agglomerates are observed in the PC matrix (see Figure 4.2 a, the red arrow) which demonstrates the challenging dispersion of GNP in PC matrix using melt mixing processes. The GNP particles are thicker than expected, based on the manufacturer, i.e. ~ 8 nm. Actual GNP particles thickness is measured between 20 to 100 nm, by measuring the thickness of the platelets perpendicular to the observed surface. By assuming a constant width of the GNP at 2 µm, the aspect ratio of the GNP is between 100 and 20. Secondly, the 2D morphology is disrupted after melt mixing. For instance Figure 4.2 b, two GNP particles are folded in two, reducing their aspect ratio by half. It seems fairly clear that the shear flow during the melt compounding process has disrupted the GNP morphology, which is in agreement with previous observations reported in literature [5, 9].

Finally, it is also observed that the PC matrix does not coat the GNP particles. This is well highlighted in Figure 4.2 c, where a GNP with folded layers is observed without any polymer coating.

4.3.2 Thermal properties

The addition of nanoparticles in polymeric matrix modifies the polymer chain dynamics. The particles create a interphase zone where the polymer chain dynamic is modified by the contact with the nanoparticle [14]. The change in chain dynamics is reflected in the change in *Tg*, where a shift of the *Tg* toward higher temperatures indicates a reduction in chain mobility and inversely a shift toward cooler temperatures shows enhanced mobility. In nanocomposites, chain mobility is affected by several parameters such as the ability of the polymer to "wet" the particle [15], the interaction between the polymer and the particle [16], the inter-particle distance [17], the size and the dispersion of the particles [14, 18].

The glass transition of the PC nanocomposites is measured by DSC, Figure 4.3. As summarised in Table 4.1, the *Tg* of neat PC is measured at 144 °C. The addition of GNP does not shift the *Tg*, indicating no change in polymer mobility which in turn could be due to the non-wetting of GNPs by the PC as observed with SEM. Previous studies also indicated no change in *Tg* with the addition of GNP to PC [19]. However, Yoonessi et al. [20] measured a slight increases of the *Tg* with the addition of reduced graphene in solution cast PC followed by a drop at 2.2 vol.%.

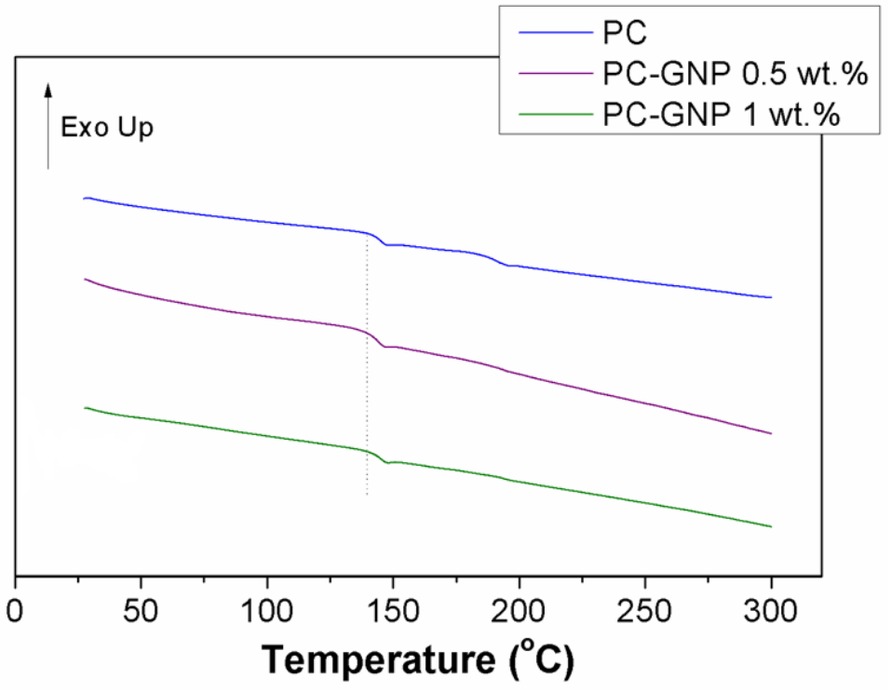

Figure 4.3 : First heating curve of pure PC, PC-GNP 0.5 wt.% and PC-GNP 1 wt.%. The dotted line represents the *Tg* onset.

Thermal stability is generally believed to increase with the addition of graphene nanoparticles. Generally, a shift of the degradation temperature to higher temperatures is reported with the addition of graphene [21-23]. Similar to layered nanoclays, 2D graphene particles increase the tortuous path creating a physical barrier that delays the volatile gases from the degradation process [24, 25]. The thermal stability study of the PC nanocomposites is performed by TGA in Nitrogen. The weight loss and the derivative weight change versus temperature are plotted in Figure 4.4, and the degradation temperature is summarised in Table 4.1.

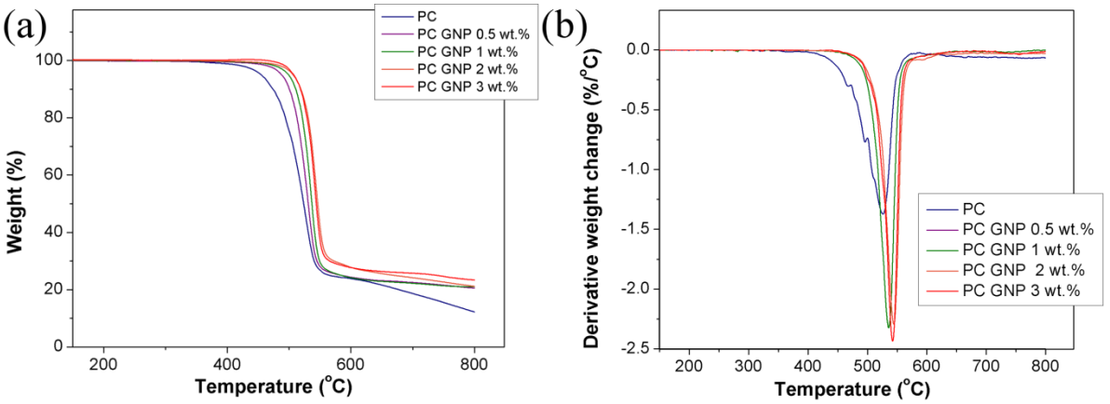

Figure 4.4: TGA results of PC nanocomposites under N_2 atmosphere; (a) represents the variation of the weight and (b) the variation of the derivative weight change with temperature.

In nitrogen atmosphere, the thermal stability is highly enhanced with the addition of GNP as shown in Figure 4.4 a. The temperature degradation is shifted toward higher temperatures with the addition of GNP. The derivative weight change (Figure 4.4 b), shows that the maximum degradation temperature increases with the addition of GNP. Decomposition of neat PC occurs in one step with a maximum degradation at 526 °C. The decomposition mainly consists of chain scission of iso-propylidene bonds and alcoholysis / hydrolysis of carbonate bonds [26]. After addition of GNP, all the nanocomposites present one main decomposition step. The temperature at the maximum rate of mass loss increases up to 544 °C after addition of 2 wt.% GNP, i.e. an improvement of 18 °C. Above 2 wt.% GNP, no further improvement in thermal stability is observed. The residue after 600 °C corresponds well with the char yield of PC and the GNP loading, i.e. ~ 27 wt.% + loading [26]. However, these results are rather disappointing, Gedler et al. [23] showed an increase of the maximum decomposition rate of 63 °C with the addition of only 0.5 wt.% of GNP with an aspect ratio of ~1800. These rather disappointing results can be explained by the random orientation of the flakes, the formation of agglomerates, but also by the very low aspect ratio of the GNP

used. The importance of aspect ratio is shown in a study on PMMA nanocomposites where the thermal stability is compared as a function of filler aspect ratio. These results showed a shift towards higher onset temperatures of degradation as filler aspect ratio increased [27].

The decomposition of PC nanocomposites is also studied in oxidative atmosphere; see in Figure 4.5 and Table 4.1.

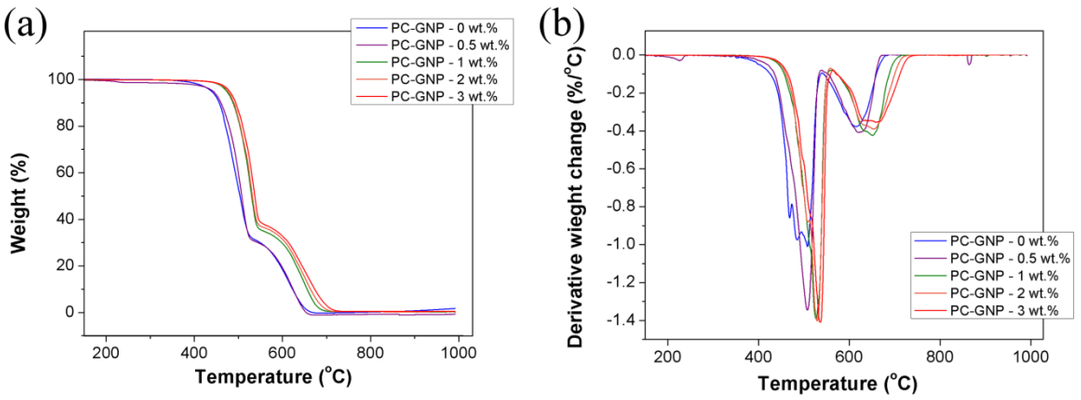

Figure 4.5: TGA results of PC nanocomposites under oxidative atmosphere; (a) represents the variation of the weight and (b) the variation of the derivative weight change with temperature.

For all neat polymer and nanocomposite samples, degradation consists of a two step process. The first step corresponds to thermo-oxidative decomposition of PC. This step is situated between 400 °C and 560 °C (Figure 4.5 b). This step mainly consists of chain scission of iso-propylidene bonds and alcoholysis / hydrolysis of carbonate bonds, similar to the nitrogen atmosphere [28]. During this step, a char layer is formed at the surface. This layer acts as an insulator layer, which reduces the air in contact with un-burnt PC and leads to a reduction in decomposition rate. The second step, after 560 °C in Figure b, is the decomposition of the remaining PC and the char layer as well as char oxidation [23].

The thermal stability in an oxidative atmosphere is highly improved with the addition of GNP. The addition of 2 wt.% GNP increases the temperature at the maximum rate of mass loss to 527 °C which is 20 °C higher than for neat PC. Similar to under nitrogen atmosphere, this shift is also rather disappointing, since an increase of 47 °C in oxidative atmosphere has been observed with the addition of 0.5 wt.% of GNP [23] which again is believed to be due to the random orientation and low aspect ratio of the GNP.

Table 4.1: Summarised data of the thermal properties of PC nanocomposites.

	Tg ***(°C)***	***Td* in N_2** ***(°C)***	***Td* in air-N_2** ***(°C)***
PC	144	526	507
0.5 wt.% GNP	144	530	507
1 wt.% GNP	144	536	525
2 wt.% GNP	144	544	527
3 wt.% GNP	-	542	535

4.3.3 Mechanical properties

The mechanical properties are measured by tensile tests. The Young's modulus of the nanocomposites is plotted in function of GNP loading and presented in Figure 4.6. The Young's modulus increases slightly with GNP loading. For instance, at 1 wt.% the Young's modulus increases by 10 %. Similar reinforcement is reported in literature. For instance, Kim et al [3] observed an increases of the Young's modulus of 3 and 7 % for 1 wt.% of graphite and reduced graphene in PC matrix, respectively.

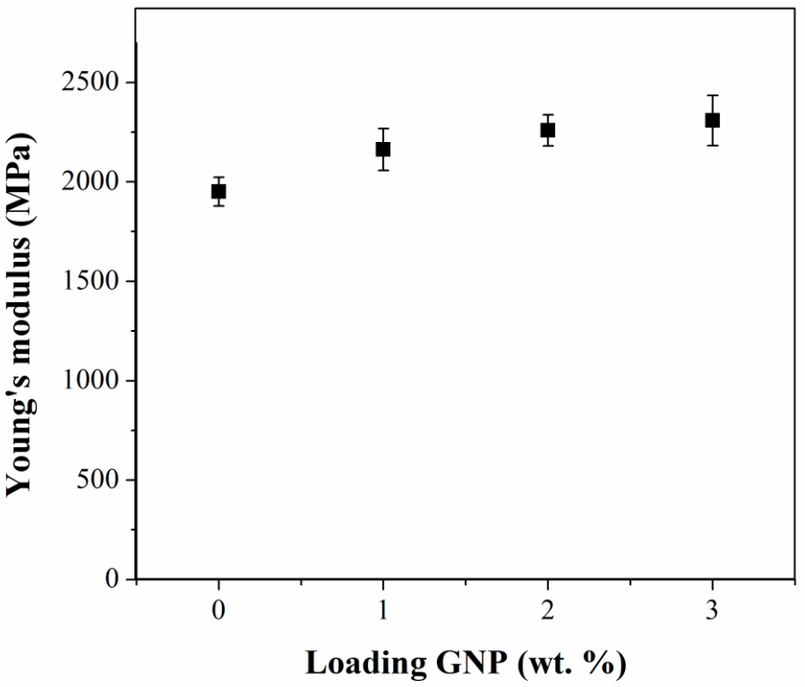

Figure 4.6: Variation of the nanocomposites' Young's modulus with the addition of GNP.

In order to evaluate the efficiency of the GNP in reinforcing the nanocomposites, the Young's modulus of the nanocomposites is analysed using the Halpin-Tsai's model, as described previously in the section 3.2.2. Based on our experimental Young's modulus, the contribution of GNP can be back-calculated using this model (Equation 4.1). This back-calculated modulus contribution for GNP is a good indicator for the efficiency of the filler to reinforce the nanocomposites. If the effective modulus contribution is equivalent to the intrinsic Young's modulus of the GNP, the particles highly reinforce the nanocomposite. Inversely, if the contribution is lower, the particles do not fully reinforce the nanocomposites. In addition, if the contribution is greater than the intrinsic Young's modulus, the reinforcement is obtained through a synergic matrix effect of particles changing the polymer morphology.

The Young's modulus of the PC matrix (E_m) is 1.8 GPa, and the Young's modulus of the nanocomposite filled with 3 wt.% (E_c) is 2.4 GPa. The GNP has a thickness of 8 nm and a diameter is 1 µm. The volume fraction (φ_f) is calculated as followed

$$\varphi_f = \frac{w_{GO} \times \rho_{matrix}}{\left((1-w_{filler}) \times \rho_{filler}\right)+(w_{filler} \times \rho_{matrix})} \quad 4.2$$

Where w_{filler} is the loading in weight; ρ_{matrix} and ρ_{filler} are the density of the PC and the GNP, respectively. Here, the density of PC and GNP are 1.19 g.cm^{-3} and 2.2 g.cm^{-3}, respectively.

The contribution of GNP to the composite modulus is calculated for GNP in the PC matrix. Based on SEM, we assume that the particles are randomly oriented in the matrix. The addition of GNP leads to an effective GNP modulus of only 80 GPa at 2 wt.%, which is significantly below the Young's modulus of multi-layer graphene with an estimated stiffness of around 400 GPa [11]. Hence, the contribution of the GNP to the nanocomposite properties is rather disappointing which is explained by the formation of particles with lower aspect ratios due to agglomeration and/or folded flakes and/or the poor interaction between polymer and filler.

4.4. Conclusions

In the present work, the addition of GNP in PC matrix is investigated. Nanocomposites of 0.5, 1, 2 and 3 wt.% are produced by a traditional melt blending process. A relatively poor dispersion of GNP particles in PC matrix is observed. The platelets are rather thick, with a thickness between 20 to 100 nm and are randomly oriented. Shearing of the melt during compounding has disrupted the GNP morphology, and leads to the formation of folded flakes.

The glass transition temperature is studied using DSC and shows no changes with addition of GNP, which indicates a poor interaction between the polymer and the GNP particles.

The thermal stability of PC nanocomposites is studied under non-oxidative and oxidative atmosphere. In both non-oxidative and oxidative atmosphere the addition of GNP improves the thermal stability. The addition of 2 wt.% GNP increases the maximum degradation temperature of PC by 20 and 18 °C, respectively. It is believed that this is due to a barrier effect of the two dimensional GNP which increases the tortuous path way and delays the out-gasing- during degradation. However, these results are rather disappointing comparing to the literature which is believed to be due to the random orientation of the GNP and their low aspect ratio.

The mechanical study shows an increase of the composite stiffness with the addition of GNP. For instance, the addition of 2 wt.% GNP leads to an increase of the Young's modulus of 16 %. Based on the Halpin-Tsai model, the contribution of the GNP to the composite properties is estimated. At 2 wt.% the contribution of the GNP is about 80 GPa which is well below the estimated intrinsic modulus of 10 layers of graphene, i.e. ~400 GPa. This poor reinforcing efficiency is believed to be due a poor polymer-particle interaction and a reduction of the GNP aspect ratio by agglomeration and/or folding.

In short, melt blending does not appear to be an efficient process to break down agglomerates of GNP particles and contributes to the formation of folded and randomly organised flakes in the polymer matrix, leading to inefficient reinforcement.

4.5. References

1. M. Moniruzzaman and K.I. Winey, Macromolecules, 2006. **39**(16): p. 5194-5205.
2. H. Kim, Y. Miura, and C.W. Macosko, Chemistry of Materials, 2010. **22**(11): p. 3441-3450.
3. H. Kim and C.W. Macosko, Polymer, 2009. **50**(15): p. 3797-3809.
4. K. Kalaitzidou, H. Fukushima, and L.T. Drzal, Carbon, 2007. **45**(7): p. 1446-1452.
5. K. Kalaitzidou, H. Fukushima, and L.T. Drzal, Composites Science and Technology, 2007. **67**(10): p. 2045-2051.
6. Abu Bakar Sulong and J. Park, Journal of Composite Materials, 2011. **45**(8): p. 931-941.
7. S. Abbasi, P.J. Carreau, and A. Derdouri, Polymer, 2010. **51**(4): p. 922-935.
8. B. Fiedler, F.H. Gojny, M.H.G. Wichmann, M.C.M. Nolte, and K. Schulte, Composites Science and Technology, 2006. **66**(16): p. 3115-3125.
9. K. Kalaitzidou, H. Fukushima, and L.T. Drzal, Composites Part a-Applied Science and Manufacturing, 2007. **38**(7): p. 1675-1682.
10. K. Kalaitzidou, H. Fukushima, H. Miyagawa, and L.T. Drzal, Polymer Engineering & Science, 2007. **47**(11): p. 1796-1803.
11. L. Gong, R.J. Young, I.A. Kinloch, I. Riaz, R. Jalil, and K.S. Novoselov, ACS Nano, 2012. **6**(3): p. 2086-2095.
12. H. Deng, R. Zhang, C.T. Reynolds, E. Bilotti, and T. Peijs, Macromolecular Materials and Engineering, 2009. **294**(11): p. 749-755.
13. H. Deng, E. Bilotti, R. Zhang, J. Loos, and T. Peijs, Synthetic Metals, 2010. **160**(5-6): p. 337-344.
14. B.J. Ash, R.W. Siegel, and L.S. Schadler, Macromolecules, 2004. **37**(4): p. 1358-1369.
15. A. Bansal, H. Yang, C. Li, B.C. Benicewicz, S.K. Kumar, and L.S. Schadler, Journal of Polymer Science Part B: Polymer Physics, 2006. **44**(20): p. 2944-2950.
16. F.W. Starr, T.B. Schrøder, and S.C. Glotzer, Macromolecules, 2002. **35**(11): p. 4481-4492.
17. B.J. Ash, L.S. Schadler, and R.W. Siegel, Materials Letters, 2002. **55**(1-2): p. 83-87.
18. H. Oh and P.F. Green, Nature Materials, 2009. **8**(2): p. 139-143.
19. J.R. Potts, S. Murali, Y. Zhu, X. Zhao, and R.S. Ruoff, Macromolecules, 2011. **44**(16): p. 6488-6495.
20. M. Yoonessi and J.R. Gaier, ACS Nano, 2010. **4**(12): p. 7211-7220.
21. R. Verdejo, F. Barroso-Bujans, M.A. Rodriguez-Perez, J.A. de Saja, and M.A. Lopez-Manchado, Journal of Materials Chemistry, 2008. **18**(19): p. 2221-2226.
22. H.J. Salavagione, G. Martinez, and M.A. Gomez, Journal of Materials Chemistry, 2009. **19**(28): p. 5027-5032.

23. G. Gedler, M. Antunes, V. Realinho, and J.I. Velasco, Polymer Degradation and Stability, 2012. **97**(8): p. 1297-1304.

24. J.W. Gilman, Applied Clay Science, 1999. **15**(1–2): p. 31-49.

25. X. Wang, H. Yang, L. Song, Y. Hu, W. Xing, and H. Lu, Composites Science and Technology, 2011. **72**(1): p. 1-6.

26. B.N. Jang and C.A. Wilkie, Polymer Degradation and Stability, 2004. **86**(3): p. 419-430.

27. T. Ramanathan, S. Stankovich, D.A. Dikin, H. Liu, H. Shen, S.T. Nguyen, and L.C. Brinson, Journal of Polymer Science Part B: Polymer Physics, 2007. **45**(15): p. 2097-2112.

28. B.N. Jang and C.A. Wilkie, Thermochimica Acta, 2005. **426**(1–2): p. 73-84.

Chapter 5

PVA-GO nanocomposites by solution casting

5.1. Introduction

Polymer processing strongly affects the quality of nanocomposites and the efficiency of nanofillers to reinforce these composites. To effectively mechanically reinforce a nanocomposite, several studies indicate that good dispersion, exfoliation, surface compatibilization and alignment of the nanofiller are all necessary [1-3]. All these factors are influenced by polymer processing. Melt compounding is the industrial process of choice to make nanocomposites but it is often also an ineffective process to well disperse GNP particle in polymer matrices, leading to nanocomposites with weak mechanical reinforcement. For instance, it was shown in the previous chapter that the addition of 2 wt.% lead to an increase of only 16 % for the Young's modulus, which translates to a modest contribution of the GNP to the composite stiffness of around 80 GPa. The melt processing is found to be inefficient in breaking

down GNP agglomerates, necessary for increasing the aspect ratio of the particles. At the same time it also promoted buckling of the nanosheets due to strong shearing, effectively lowering their reinforcement efficiency.

Solution casting on the other hand is a mild model processing method where often a good dispersion of the particles in the matrix can be achieved. It is a traditional method where particles are dispersed in solution prior to the mixing with a dissolved polymer. Good dispersion of the particles is usually obtained by sonication which breaks down agglomerates. The process involves mild processing conditions with low shear forces due to the low viscosity of the system and the subsequent casting and drying process. However, slow drying can lead to re-agglomeration of particles [4].

The orientation of the particles is strongly affected by both processing and loading. In solution casting, for instance, the orientation of GO platelets is dependent on the filler loading. Recently, Li et al [5] produced solution cast PVA-GO nanocomposites with a loading of 80 wt.% of GO. These nanocomposites presented a layer-by-layer structure, while at lower loading, i.e. 1.8 vol.%, the particles showed no alignment in the PVA matrix [6].

Graphene oxide (GO) is atomically flat. It is issued to the strong oxidation of the graphite to form intercalated graphite. Sonication is usually used to break the graphite into graphene oxide. Although the chemistry of GO is still being debated [7-13], it is often described as a single layer with both graphitic areas and functionalised areas with hydroxyl and epoxide groups on the surface and carboxyl and carbonyl groups at the edges [14]. These functionalities allows the GO to disperse well in aqueous solvents [15] but also weakens the graphitic sheet. While the Young's

modulus of single layer graphene is 1 TPa [16], the Young's modulus of a single layer of GO is reduced by a factor of 5, reaching values of only 208 GPa [17], i.e. similar to nanoclays or standard grade carbon fibre.

Several studies reported a very good dispersion of GO or reduced GO in solution cast PVA nanocomposites [6, 18, 19]. This is due to the good exfoliation of the particles and the good interaction between polymer and GO [20]. Due to the good dispersion, as well as the interaction between the PVA and the GO, the mechanical properties of PVA-GO are expected to be good. Several studies have presented very promising mechanical reinforcement of PVA filled with GO [19, 21, 22]. For instance, solution cast PVA-GO nanocomposites showed an increase of the tensile strength and Young's modulus by 76 % and 62 % with the addition of only 0.7 wt.% GO. Interestingly, the experimental data showed a reinforcement that is superior to the expected moduli data based on Halpin-Tsai's model [19] which is described as a consequence of a good dispersion, a perfect load transfer and a rigidification of the polymeric chains.

In this study, a traditional solution cast nanocomposite of PVA filled with GO is produced. Nanocomposites with filler loadings of 0.05, 0.1 and 0.5 wt.% are made. The thermal and mechanical properties of these nanocomposites are studied and addressed in function of the alignment of the particles and their effect on the polymer morphology.

5.2. Experimental

5.2.1 Materials

The poly(vinyl alcohol) is supplied by Sigma Aldrich (Mw ~85,000 - 124,000 $g.mol^{-1}$, 98-99 % hydrolyzed). The graphite oxide is obtained by Hummer's method and kindly provided by Sichuan University.

5.2.2 Preparation

PVA is dissolved in deionised water at 90°C and continuously stirred for 4 hrs, to give a solution at 10 wt.%. The PVA solution is then cooled to room temperature.

Graphene oxide solution is obtained by dispersing the GO in deionised water at 1 $mg.mL^{-1}$ using a high-power ultrasonication tip (Sonics VCX 500) (amplitude of sonication is set to 20 %, the pulser to 2 sec on / 2 sec off and the energy time is modified in function of the experiment). GO suspension is left aside for at least 12 hrs to let thicker graphite aggregates to precipitate.

The right volume of GO solution is then dropwise added to PVA solution and stirred for 4 hrs at room temperature. The solution is left aside for 12 hrs to allow the solution to degas and then the solution is cast in a PS petri-dish and dried under ambient conditions for 5 days in a fume-hood. All the samples are stored in desiccator to prevent the water uptake by PVA films.

5.2.3 Characterization

UV-Vis is performed by a Perkin Elmer 950 and ran from 800 to 200 nm. For this the GO suspension obtained after sonication is diluted to 0.01 $mg.mL^{-1}$ and measurements are done with 3 mL of the suspension dropped in a quartz cuvette.

Atomic Force Microscopy is performed using a NT-MDT in tapping mode. GO exfoliated by sonication is here diluted to 0.1 $mg.mL^{-1}$ and then sprayed onto a freshly cleaved mica sheet. AFM is performed in tapping mode using a three-points head.

Scanning Electron Microscopy is performed using a FEI Inspector-F scanning electron microscope. Samples were observed at a working distance of 10 mm and at 5 kV. Prior to the observation all samples are gold coated.

Dynamic Mechanical Analysis is performed by a DMA Q800 V7.5. The DMA is performed in tension mode (1 Hz) at a temperature range from – 50 °C to 240 °C at 3 $°C.min^{-1}$.

Differential Scanning Calorimetry is performed using a Mettler DSC 822e differential scanning calorimeter. 6 – 7 mg of material is used for each experiment. The method consists of two heating and two cooling scans. The two heating scans are from 20 °C to 235 °C at a rate of 10 $°C.min^{-1}$ and the two cooling scans are from 235 °C to 20 °C at 30 $°C.min^{-1}$.

Wide Angle X-Ray Diffraction data are obtained using a Panalytical Xpert Pro diffractometer with a Cu-Kα source at a distance of 8 mm and at a wavelength of 1.54 Å. The reference sample used is aluminium oxide. The number of pixel

detectors is 4096*4096 with a size of 15.137 μm. The 2D data are transformed into 1D data using the software FIT2D.

Tensile tests are performed using an Instron 5586 at room temperature, equipped with a load cell of 1 kN at a test speed of 10 $mm.min^{-1}$ and a 20 mm gauge length. Test samples are tapes of ~4 mm wide with a thickness between 0.1 and 0.2 mm.

5.3. Results and discussion

5.3.1 Dispersion of Graphene Oxide

Graphene oxide is obtained by Hummers's method [23]. It is a layered material which can be easily exfoliated and dispersed in water due to its highly functionalise surface with hydroxyl groups [15]. To allow the exfoliation of GO in de-ionised water, ultrasound sonication is used. The exfoliation of GO, consisted of breaking down the graphite oxide, providing monolayers of GO with high aspect ratios. To monitor the exfoliation of GO in DI Water, UV-Vis spectroscopy is used. UV-Vis spectroscopy has been presented as a simple and fast tool to monitor the exfoliation of MWCNT [24] and rGO [25] in aqueous surfactant solution. The absorbance peak between 200 to 300 nm is monitored and is characteristic to individual particles.

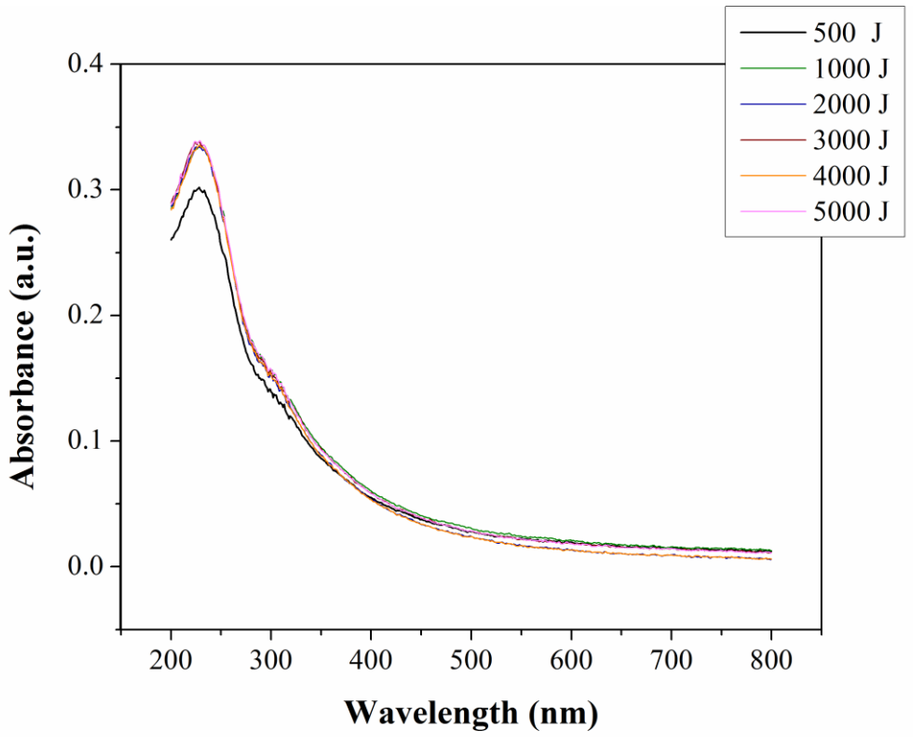

Figure 5.1: UV-Vis spectroscopy of GO in DI water in function of sonication energy.

The evolution of the exfoliation during sonication by UV-Vis is plotted in Figure 5.1. As expected an absorbance peak is observed in the mid-UV range, reaching a maximum at 228 nm, which is attributed to $\pi \rightarrow \pi^*$ conjugations of C=C bonds [26]. As the sonication energy increases, the absorbance peak is increased to higher value. This increase being characteristic of individual sheets and demonstrates the positive effect of sonication to exfoliate GO. After a certain energy, the absorbance peak does not increase any further but remains stable. To highlight this phenomenon, the absorbance at 228 nm is plotted in function of the sonication energy and presented in Figure 5.2.

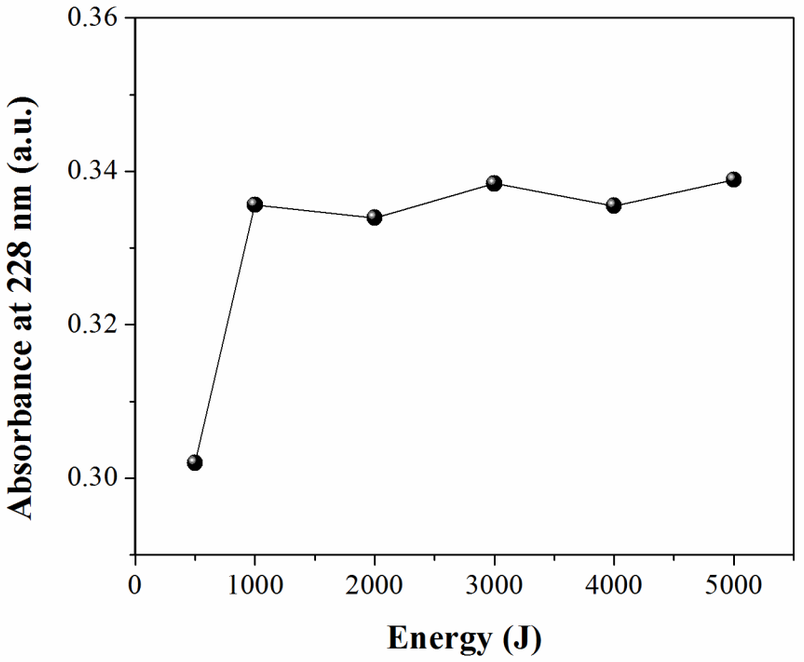

Figure 5.2: Absorbance of the 228 nm peak in function of sonication energy as measured by UV-Vis spectroscopy.

As shown in Figure 5.2, a strong increase of the absorbance peak is observed from 500 to 1 000 Joules which describes the exfoliation of GO. However, after 1 000 Joules of sonication, the absorbance peak reaches a plateau. This plateau demonstrates that GO is fully exfoliated. To observe the effect of sonication on the GO morphology, AFM is used as this allows a full characterization of the GO topography, i.e. thickness and length.

The thickness of GO sonicated at 1 000 Joules is studied and presented in Figure 5.3.

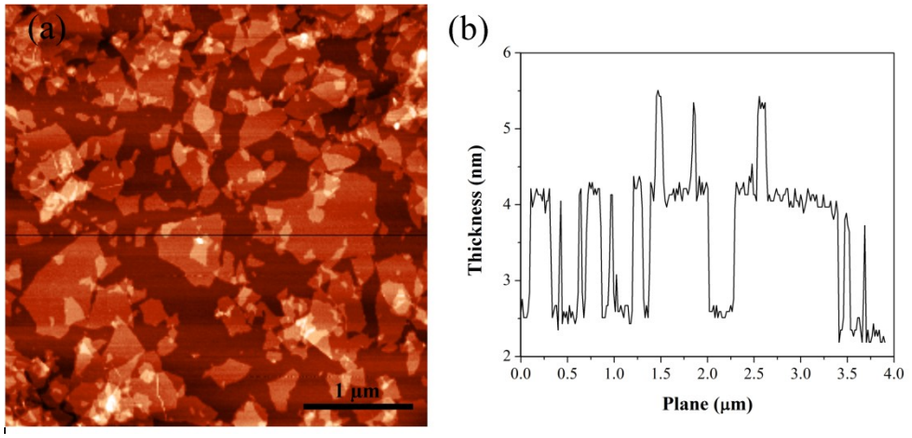

Figure 5.3: Surface topograpy of GO sprayed onto mica sheet. (a) AFM height image of GO and (b) thickness profile of the central black line in image (a).

The AFM picture in Figure 5.3a, shows a homogeneous dispersion of the GO. It is interesting to note that GO sheets have different shapes and also a very large range of widths/diameters going from several microns to a few nanometres. Surface topography is conducted along the mid-section as indicated by the black line (Figure 5.3b). The platelets have a measured thickness of around 1.6 nm. This thickness is in agreement with a study from Mkhoyan et al. [27], who measured the thickness of GO by AFM at about 1.6, 2.6 and 3.6 nm for a monolayer, bi and tri-layers. Our suspension of GO after only 1 000 Joules of sonication consisted mainly of monolayers, which shows the efficiency of sonication to fully exfoliate GO in DI water.

As observed previously, the range of diameters of GO sheets in the suspension is very wide. In order to obtain the optimum sonication time for high aspect ratio GO sheets, the morphology of the flakes is compared in function of sonication energy. Based on AFM pictures of 100 particles, a histogram is plotted showing the width or diameter profile of GO in function of sonication energy (Figure 5.4).

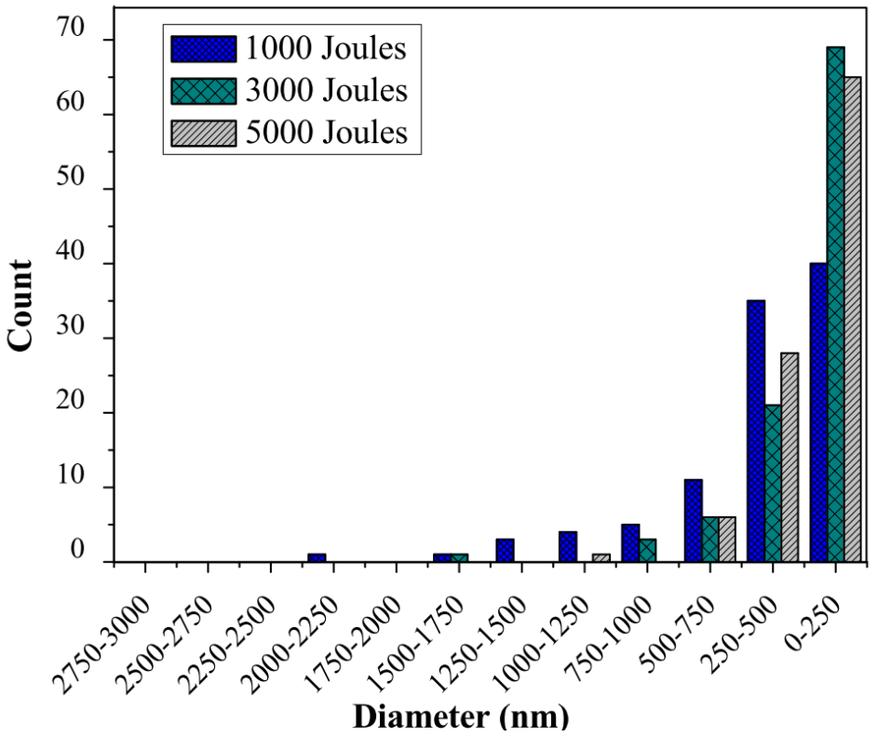

Figure 5.4: Histogram of diameter profile of GO in function of sonication energy, based on 100 particles.

As observed in Figure 5.4, sonication although very efficient in exfoliating GO, also breaks down the sheets into very small particles, i.e. < 500 nm. The lowest sonication energy shows however a wider range of diameters, i.e. from a few nanometres to 2.5 μm compared to the other sonication energies.

To summarize, sonication between 500 and 1 000 Joules allows the graphite oxide to fully exfoliate in water to obtain monolayers of GO by breaking the bonds between the GO sheets. However, with increasing sonication energy, this energy also increasingly breaks the sheet into smaller fragments. This effect is probably more dominant for bigger sheet due to their greater flexibility. Hence, over-exposure of GO to ultrasound is not recommended as this will damage the sheets, effectively lowering their aspect ratio and efficiency.

In order to obtain GO with the highest aspect ratio, sonication is employed to exfoliate graphite oxide in water at 1 000 Joules only. This suspension consists of monolayers with a very wide range of diameters from a few nanometres to several microns. The average sheet width or diameter, based on 100 particles is ~400 nm, giving an aspect ratio of 300.

5.3.2 Dispersion of GO in PVA

A good dispersion of GO in the PVA matrix is the first condition for effective reinforcement. To control this, the samples are first observed optically and then at the micro- or nanoscale using SEM. By adding GO to PVA, the PVA which is naturally transparent turns to a yellow-brown colour. As more GO is added this colour gets darker as shown in Figure 5.5. The dispersion of GO in PVA, based on optical observations, is homogeneous. Neither phase separation, nor big clusters are observed. Low loading samples are fairly transparent with the transparency decreasing with increasing loading. The good transparency demonstrates a good dispersion and exfoliation of the GO [28]. By increasing the loading more light is scattered and/or absorbed thereby leading to a decrease in transparency [29].

Figure 5.5: Picture of PVA nanocomposite strips. From left to right; neat PVA, PVA-GO 0.05 wt.%, PVA-GO 0.1 wt.% and PVA-GO 0.5 wt.%.

To further investigate the dispersion of GO in PVA, SEM microscopy is used. Here the cross sections of the samples are studied.

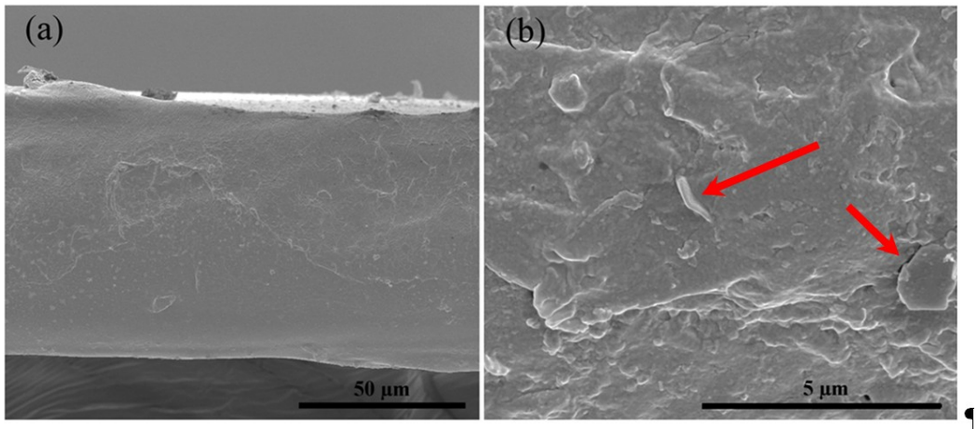

Figure 5.6: SEM picture of PVA-GO 0.5 wt.% at (a) low magnification and (b) higher magnification; the red arrows show GO platelets.

As observed in Figure 5.6 a, the dispersion of GO is very uniform and does not show any agglomerates, nor phase separation. Also at higher magnification, no agglomerates are observed. Instead GO platelets are observed as indicated in Figure 5.6 b, by the red arrows. There is no preferred orientation of the platelets. This

random orientation of GO in PVA solution cast nanocomposites at low loadings is also observed in literature [6]. The GO platelet in Figure 5.6 b, which is pulled-out from the PVA matrix is around 2 µm in width and 20 nm thick. The platelet appears thicker than a monolayer, which is believed to be due to the polymer coating present on the surface of the GO. PVA is known to show strong interaction with GO, which leads to good wetting of the polymer and good interfacial adhesion. Also, it worth noting that from these SEM pictures, no major aggregates or folded sheets are observed, reflecting the mild processing condition involved in solution casting of films.

The good dispersion of GO in PVA, is in agreement with other studies [6, 18, 19, 30]. The chemistry of the polymer strongly affects the dispersion of GO and the exfoliation. Indeed, highly hydrolysed PVA contains a heavy free hydroxyl group. On the other side, GO also contains hydroxyl groups at the edges and on the surface [15], which can easily bond with pendant hydroxyl groups of PVA as presented in Figure 5.7. It is this hydrogen bonding between the PVA and the GO which counterbalance the van der Waals interactions [30].

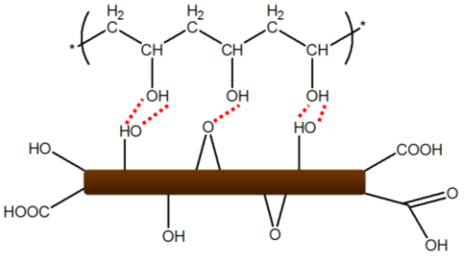

Figure 5.7: Model of the interaction between PVA and GO (redrawn from [20]).

These strong bonds allow for a good dispersion of the GO in the PVA matrix and also positively affects the properties of the nanocomposite as it provides efficient stress transfer between polymer matrix and filler.

5.3.3 Thermal properties

Addition of nanofiller can induce major changes to the molecular mobility, the crystallisation behaviour and glass transition temperature. These modifications can drastically modify the overall mechanical and thermal properties of the nanocomposites. For example, the degree of crystallisation strongly modifies the mechanical behaviour of semi-crystalline polymers, since the crystalline part has a higher modulus compared to the amorphous part [31]. In addition, crystallization through the addition of SWNTs is reported to improve stress transfer between a PVA matrix and SWNTs [32] and for polycaprolactone matrix and GO [33]. To understand the effects of the addition of GO to the nanocomposite properties, we have studied the thermal properties of the nanocomposites by DSC.

A crystallisation study of PVA is difficult to carry out because its melting temperature is very close to its degradation temperature, which affects the crystallisation and shift down the crystallisation temperature [34-36]. As previously discussed by Wang et al. [36], to minimize degradation of the PVA, the cooling rate is increased to – 30 °C.min^{-1}. In Figure 5.8, the melting behaviour of neat PVA is presented during the first heating (dash line) and the second heating (solid line).

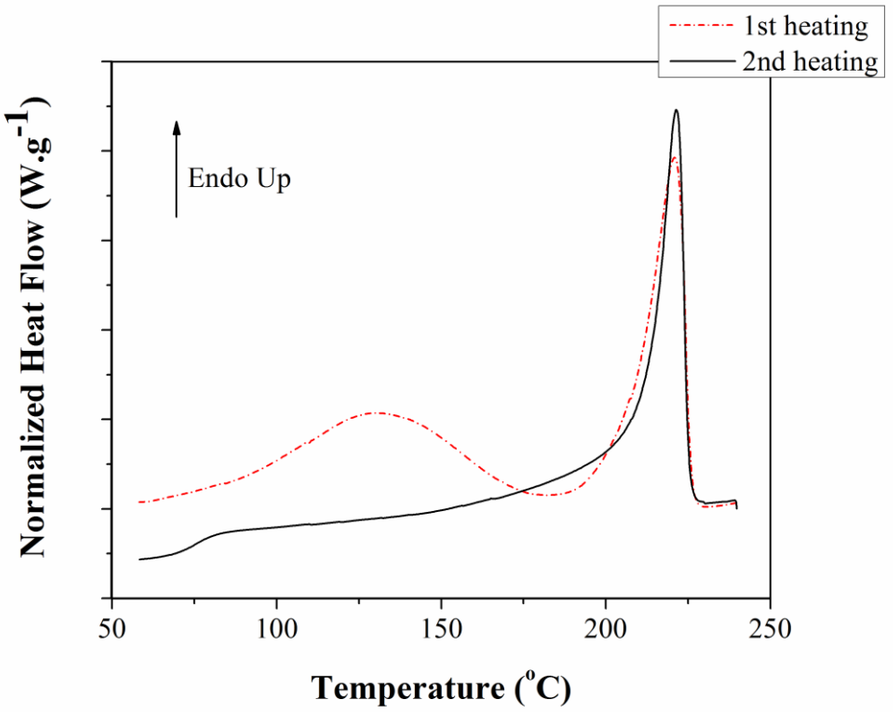

Figure 5.8: DSC scan of the melting behaviour of pure PVA during the first heating (dash line) and second heating (solid line) at a heating rate of 10 °C.min^{-1} and a cooling rate of – 30 °C.min^{-1}.

During the first heating, two endothermic peaks are observed whereas there is only one peak during the second heating. The first peak during the first heating is a broad peak between 50 °C to 150 °C. This peak corresponds to the evaporation of water bonded to PVA [37]. The second peak is observed at higher temperature and represents the actual melting peak of the PVA crystals. This peak is also observed during the second heating. Table 5.1 summarised the thermal behaviour of the PVA and PVA-GO nanocomposites, observed in Figure 5.9.

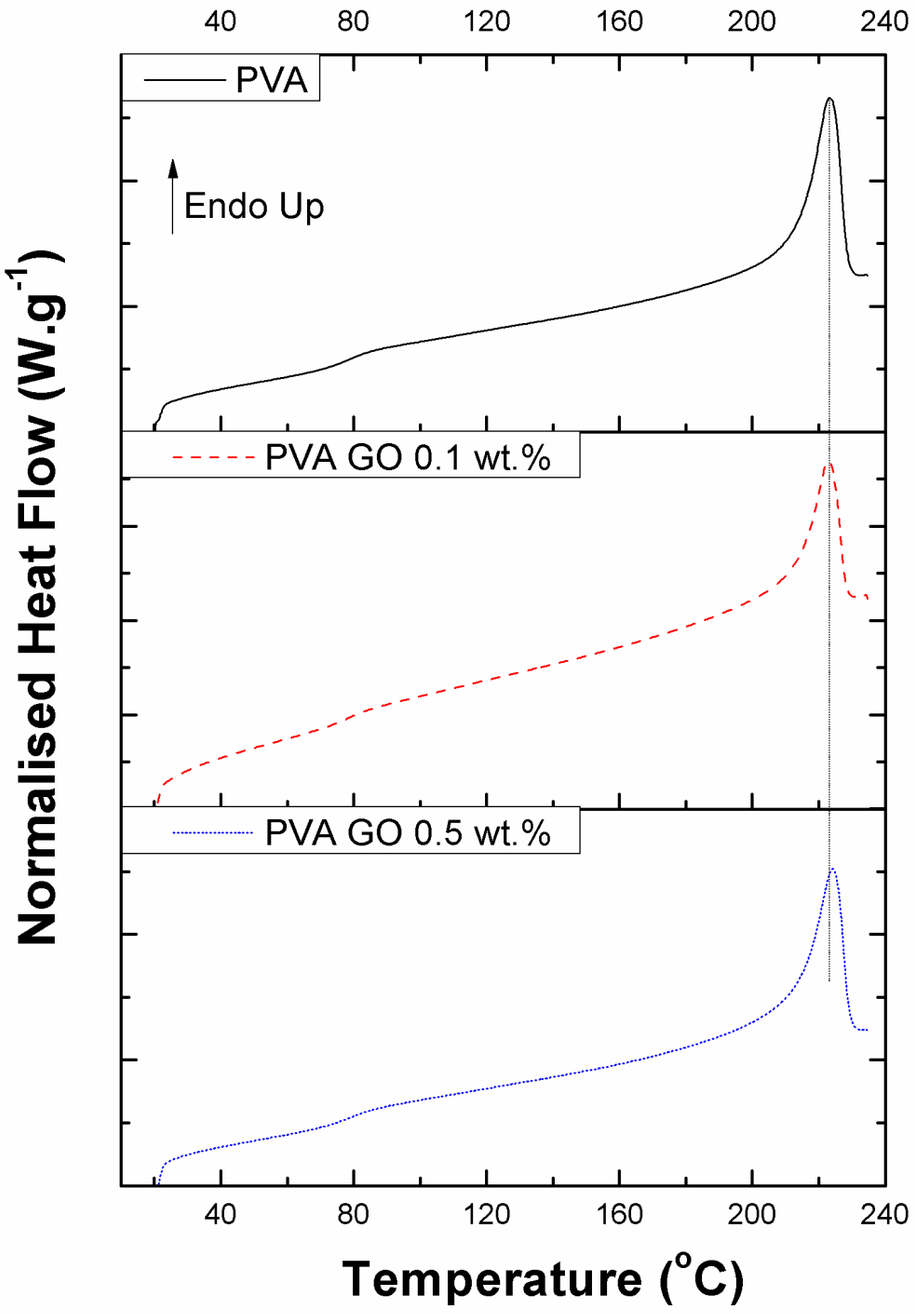

Figure 5.9: First heating curve of pure, PVA-GO 0.1 wt.% and PVA-GO 0.5 wt.%. The dotted line is a guide line representing showing the melting temperature of pure PVA.

Table 5.1: DSC measurements of PVA and PVA-GO nanocomposites, during the first heating ($_1$) and the second heating ($_2$). The glass transition temperatures are measured during second heating. Melting enthalpy and degree of crystallinity are measured during first heating.

	Tg_2 (°C)	**Tm_1 (°C)**	**Tm_2 (°C)**	**ΔQm_1 ($J.g^{-1}$)**	**X_1 (%)**
PVA	74.0	222.5	222.0	54.7	39.5
0.05 wt.% GO	77.4	222.2	222.3	54.4	39.2
0.1 wt.% GO	77.5	222.2	222.7	49.1	35.4
0.5 wt.% GO	79.6	222.8	223.6	51.2	36.9

For all samples, the melting temperature for both first (Tm_1) and second heating (Tm_2) are similar. The crystals formed during the solution casting are of similar size than the crystals formed at high cooling rate. Also the melting temperature remains the same with the addition of GO, which indicates that there is no modification of the crystals by the addition of GO.

The degree of crystallinity (X_c) can be estimated from the melting heat (ΔQm) following this equation:

$$X_c = \frac{\Delta Qm}{\Delta H_0} \qquad 5.1$$

Where ΔH_0, is the melt enthalpy of 100 % crystalline PVA, and corresponds to 138.6 $J.g^{-1}$ [38].

The degree of crystallinity corresponds to the normalised melting peak area corrected for the weight of polymer and compared to a PVA with 100 % crystallinity. The degree of crystallinity is measured during the first heating and is around 39.5 % and slightly reduced by the addition of GO to around 36.9 % for 0.5 wt.% GO. Graphene sheets are observed to reduce the PVA crystallisation kinetics [39] despite its nucleant effects[39, 40]. A reduction of the crystallinity in PVA nanocomposites with the addition of GO is also reported by XRD [5, 41, 42] and is attributed to the strong interaction between the PVA and the GO. Strongly adsorbed on the GO surface, the polymer chains have a lower mobility which inhibits the crystallisation process [42].

Finally the *Tg* is studied during the second heating. The glass transition temperature describes the temperature where polymer chain motion is changed from a glassy state to a more flexible state. Here, the addition of GO lead to a noticeable increase of the *Tg* from 74 to 79 °C with the addition of only 0.5 wt.% GO. This increase in *Tg* is also observed for other studies on PVA-GO [19] and PVA-reduced GO [43, 44]. A major increase of the *Tg* reflects a reduced polymer chain mobility. This change in chain dynamic mobility is associated with again the strong interactions between the PVA and GO [45] in agreement with the chemistry previously described.

Since PVA degrades at temperatures near the melting temperature, the change in *Tg* is also investigate by DMA. As summarised in Table 5.2, the storage modulus at room temperature increases with addition of GO. For instance, the storage modulus increased by 32 % with the addition of the only 0.5 wt.% of GO.

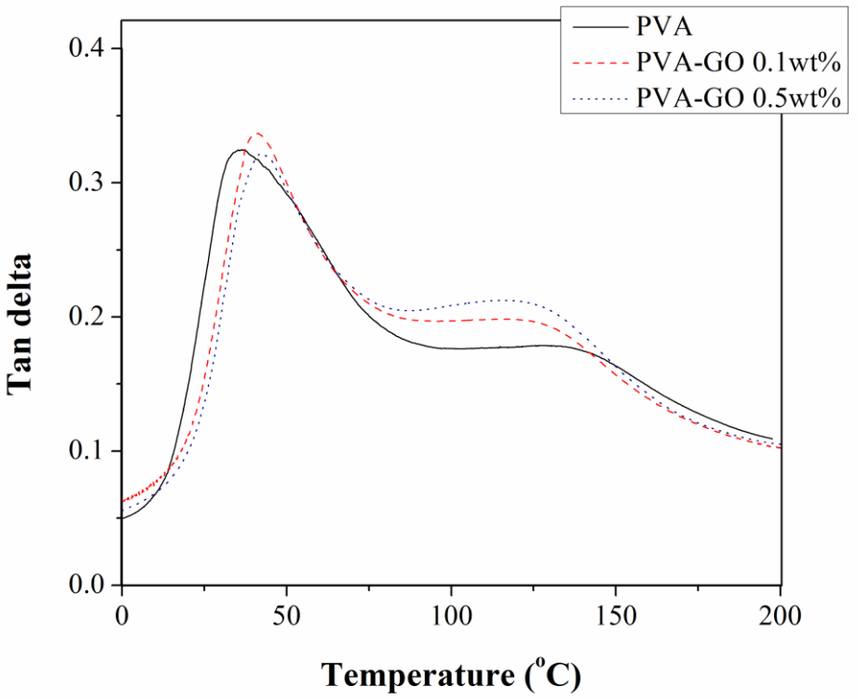

Figure 5.10: DMA spectra of PVA/GO nanocomposites, showing the *tan δ* in function of temperature.

Figure 5.10 presents the mechanical loss tangent, *tan δ*, of the nanocomposites as a function of temperature. The pure PVA film presents two peaks: one at 35 °C and a second one at 128 °C. The first peak, T_α, corresponds to α_a relaxation of the amorphous phase and describes the glass temperature transition of the PVA. The second peak at higher temperature, T_β, on the other hand, corresponds to the β_c relaxation of the crystalline phase of the PVA [46].

In agreement with the DSC and based on the data presented in Table 5.2, the addition of GO also leads to an increase of the T_α toward higher temperatures. The addition of GO leads to a rigidification of the amorphous phase. In contrast, T_β, as reflected by the crystalline region, undergoes a decrease toward lower temperatures with the addition of GO. This shift suggests that there is no interaction between GO

particles and the crystalline phase in PVA. In contrast, SWNTs are observed to initiate a shift toward higher temperatures for relaxation of the crystalline regions [46, 47]. While SWNTs are well-known for its nucleating effect on PVA [35], GO particles on the other hand inhibit the initiation of crystallisation in PVA [5, 41, 42].

Table 5.2: Summary from DMA presenting the storage modulus at 25 ºC and *tan δ* for PVA-GO nanocomposites. T_α and T_β represents the glass temperature transition and the temperature of relaxation of the crystalline phase.

	Storage Modulus @ 25°C	**T_α**	**T_β**
	(MPa)	***(°C)***	***(°C)***
PVA	3 100	35	128
0.1 wt.% GO	3 600	42	116
0.5 wt.% GO	4 100	43	116

The mechanical *Tg* is lower than the *Tg* measured by DSC. First of all, it is worth to note that *Tg* measured by different techniques are difficult to compare. Second of all, the *Tg* measured by DSC is measured during the second heating, thus the samples are fully dry, while it is well known that the presence of water in PVA leads to a plasticising effect which decreases the *Tg* [48].

5.3.4 Mechanical properties

The good dispersion and exfoliation of the GO platelets together with the strong interfacial interactions present between the PVA matrix and GO makes this filler a very good candidate for mechanical reinforcement in solution cast nanocomposite

films. The mechanical properties of the solution cast PVA-GO films are investigated by tensile tests. Figure 5.11 presents the stress-strain curves of the PVA/GO nanocomposites. The results are summarised in Table 5.3

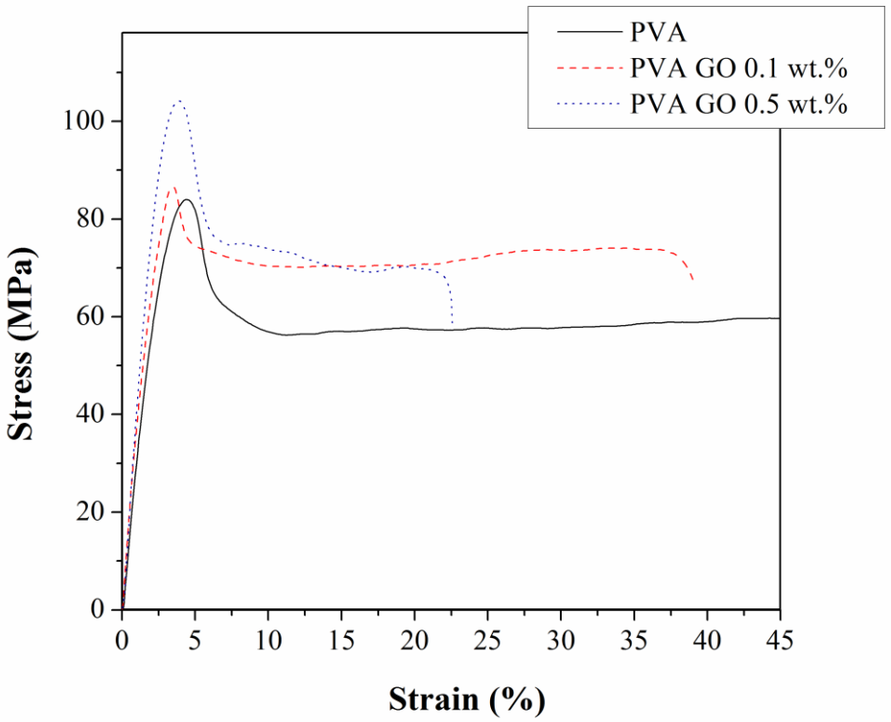

Figure 5.11: Strain-stress curve of neat PVA and PVA-GO nanocomposites.

The addition of GO improved the stiffness of the nanocomposites, as shown in Figure 5.11. Mechanical properties such as Young's modulus and yield stress are increased with the addition of GO. For example, the addition of only 0.5 wt.% of GO increases the Young's modulus and yield stress by 34 % and 17 %, respectively. However, the addition of GO also leads to a reduction of the strain at break, which could be associated with an embrittlement effect of stiff particle in soft matrix.

Table 5.3: Summary of mechanical properties. The values are means ± standard deviation. The data are obtained on minimum 3 to 5 samples.

	Young's modulus *(GPa)*	**Yield stress** *(MPa)*	**Strain at break** *(%)*
PVA	3.2 ± 0.1	90 ± 4	90 ± 71
0.05 wt.% GO	3.5 ± 0.1	91 ± 6	28 ± 12
0.1 wt.% GO	3.9 ± 0.09	101 ± 15	25 ± 11
0.5 wt.% GO	4.3 ± 0.07	106 ± 2	25 ± 21

5.3.5 Micromechanical modelling

In order to quantify the efficiency of the GO to reinforce the PVA matrix, the effective Young's modulus of the GO platelets in the PVA-GO nanocomposites is back-calculated and summarised in Table 5.4; in accordance with the Halpin-Tsai equations as described in paragraph 3.2.2.

Material parameters used for these calculations are a Young's modulus of the neat PVA matrix (E_m) of 3.2 GPa and a Young's modulus of the nanocomposite with 0.5 wt.% GO (E_c) of 4.3 GPa. The reinforcing filler is assumed to be a circular platelet with a thickness of 1.6 nm and an average diameter of 400 nm. The volume fraction (φ_f) is calculated following Equation 4.2 where the density of the PVA and the GO are taken as 1.3 g.cm^{-3} and 2.2 g.cm^{-3}, respectively.

Table 5.4: Contribution of GO, back-calculated using Halpin-Tsai's model for oriented and non-oriented particles.

	GO contribution (GPa)		
	0.05 wt.% GO	**0.1 wt.% GO**	**0.5 wt.% GO**
Oriented	> 1000	> 1000	~ 950
Non-Oriented	> 1000	> 1000	> 1000

The back-calculated Young's modulus of GO is about 950 GPa for 0.5 wt.% oriented nanocomposites and even higher at lower loadings or for random orientations. However, as mention before, the intrinsic modulus of the GO as measured by AFM, is only 208 GPa [17]. Hence, the contribution of the GO to the PVA nanocomposites is 5 times greater as compared to its intrinsic modulus, suggesting some synergistic matrix dominated reinforcing effect.

5.3.6 Polymer orientation

Based on the synergistic mechanical property data, it is expected that the addition of GO has significantly modified the morphology of the polymer matrix. A hypothesis that the synergistic reinforcement is related to a change in the polymer is rather remarkable as the GO loading is very low. For instance, we previously reported that the addition of GO increased the glass transition temperature as a result of a reduction in chain mobility, which might explain the increased stiffness of the overall nanocomposites. In addition, a modification of the orientation of the PVA crystals could also provide an enhancement of the mechanical behaviour of the nanocomposites. For example, graphene sheets are found to act as a strong

nucleating agent for PLLA, where the polymer chains are adsorbed on the surface of the graphene, inducing a change of the chains conformation from random to in-plane. This change in conformation promoted the crystallisation of PLLA [49]. A conformational ordering of isotactic PP chains is also observed on GO, which also triggered early crystallisation [50]. In addition, orientation of PE chains is found to be parallel to the basal plane of reduced-GO [51].

In order to get more insight into the polymer modification after the addition of GO, an X-ray diffraction study is performed. Figure 5.12 presents the diffraction pattern of pure PVA and PVA-GO nanocomposites.

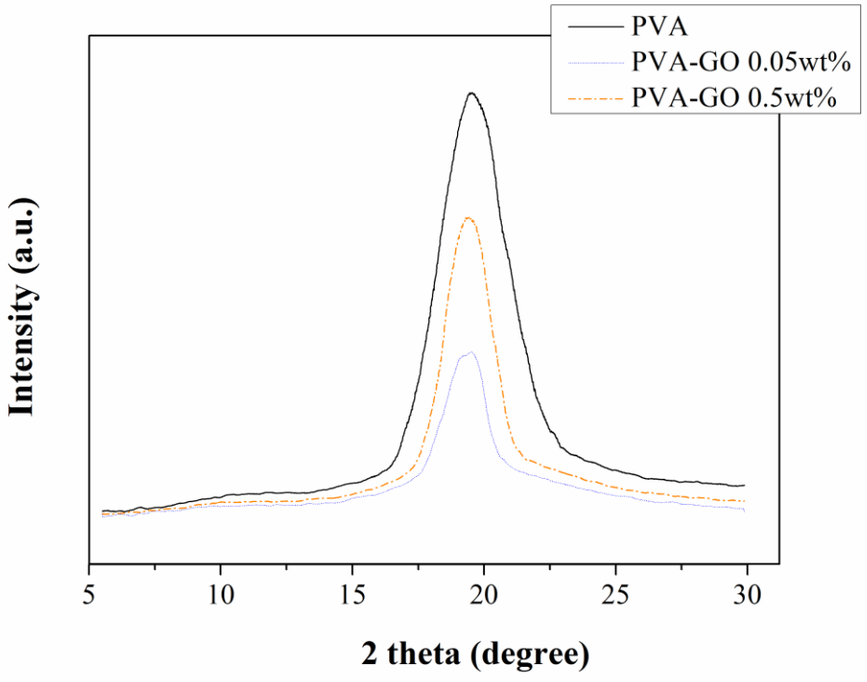

Figure 5.12: Diffraction pattern of pure PVA and PVA nanocomposites.

The X-ray diffraction pattern of pure PVA presents an intense and wide peak at $2\theta = 19.4°$. PVA has four crystalline reflexions, indexed as 100, $10\bar{1}$, 101 and 200

which corresponds to an 2θ angle of 16.0°, 19.4°, 20.1° and 22.7°, respectively [48, 52]. The wide peak observed at $2\theta = 19.4°$ corresponds to the overlap of $10\bar{1}$ and 101 crystalline reflexion. The addition of GO did not shift the peak which indicates that the crystalline structure of the PVA is not affected by the addition of GO. This is consistent with the DSC data, which showed no change in *Tm* with the addition of GO. On the other hand, the intensity of the peak is reduced after the addition of GO. This indicates that the crystallinity is reduced with the addition of GO, and is again in agreement with the DSC results.

To study the polymer orientation, the diffraction is taken in two directions, out-of-plane (face) and in-plane (cross-section) as shown in Figure 5.13. The diffraction pattern for each samples are summarised in Table 5.5.

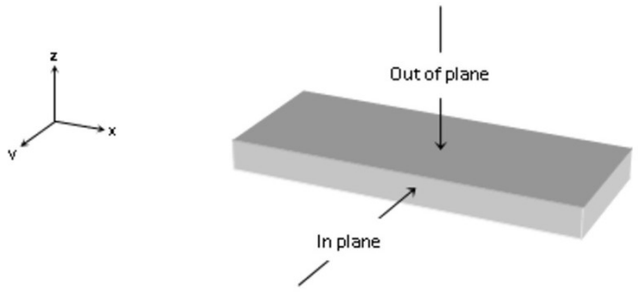

Figure 5.13: Schematic of the XRD measurements.

Table 5.5: Diffraction patterns of solution cast PVA nanocomposites in the surface (out-of-plane) and along the cross-section (in-plane) as presented in Figure 5.13.

	Out of plane	**In plane**
PVA	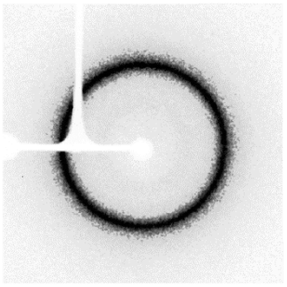	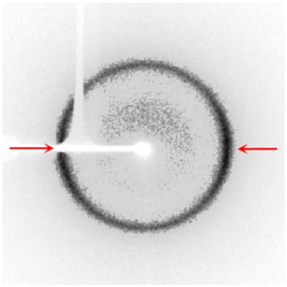
0.05 wt.% GO	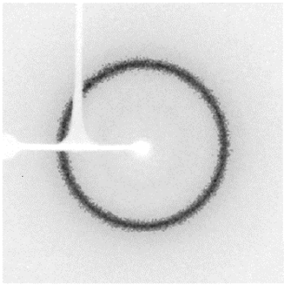	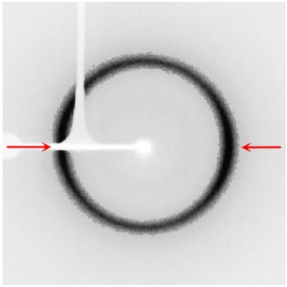
0.1 wt.% GO	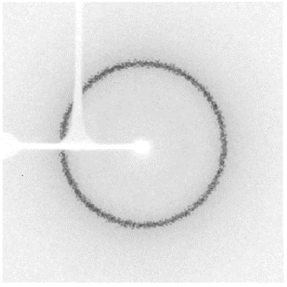	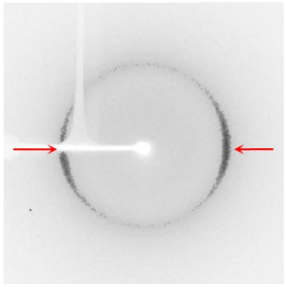

As seen in Table 5.5, in the direction perpendicular to the nanocomposite films the diffraction patterns for all concentrations show no indication of preferred orientation, i.e. PVA crystals are randomly oriented and the addition of GO does not modify the orientation of the PVA crystals. However, as indicated in Table 5.5 by the red arrows for the in-plane 0.1 wt.% GO sample, the diffraction pattern shows greater intensity which indicated a preferred orientation of the PVA crystals when measured through

the thickness of the nanocomposite films. The results show that the addition of GO does not modify affect the pre-orientation of the PVA crystals.

Similar results are observed for solution cast PVA-SWNT nanocomposites where PVA crystals are randomly orientated along the surface of the film but oriented along the thickness [53]. A preferred orientation of lamellar crystals is previously observed in ultra-high molecular weight polyethylene gels cast under ambient condition where the crystals are oriented perpendicular to the thickness sample, while are randomly distributed along the plane [54]. The authors described the orientation of the crystal as a consequence of the reduction of the thickness of the film that occurs during the solvent evaporation as presented in Figure 5.14.

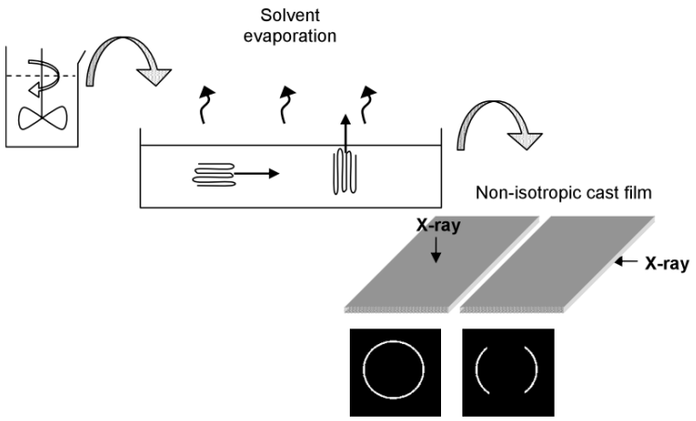

Figure 5.14: Schematic illustration of the crystal orientation during solution casting, resulting in a pre-oriented film. Typical WAXD patterns are observed for films with a random orientation when measured along the surface and oriented when measured along the thickness [53].

5.4. Conclusions

In this chapter we prepared PVA-GO nanocomposites by a sonication supported solution casting method. Nanocomposites with GO loadings of 0.05 wt.%, 0.1 wt.% and 0.5 wt.% are produced. Following sonication, the dispersion of GO in the PVA matrix is very good, which is believed to be due to hydrogen bonding between GO and PVA, preventing GO agglomeration. Based on SEM data, no preferred orientation of the GO sheets in the PVA matrix is observed. Moreover, the presence of folded GO sheets is not observed either as a result of the mild processing conditions involved in the solution casting method.

Thermal properties of the films are studied by DSC. An enhancement of the glass transition temperature is observed with the addition of GO, which can be described to rigidification of the amorphous PVA phase as a result of the strong interactions between PVA and GO. The *Tg* of the PVA increased from 74 to 79 °C for composite systems incorporating as little as 0.5 wt.% of GO. However, no change in overall crystallinity is observed by DSC measurement.

DMA measurements also show an increase in the *Tg*. In addition, here a shift of the crystal relaxation toward lower temperatures is observed with the addition of GO, demonstrating that there is no interaction between GO particles and the crystalline regions of the PVA.

The mechanical properties are greatly improved by the addition of GO nanosheets. For example, the addition of 0.5 wt.% GO increased the Young's modulus and yield stress by 36 % and 13 %, respectively. If a random orientation of the GO is considered, the modulus contribution of the GO to the composite as back-calculated from composite theory exceeded 1 TPa, i.e. 5 times the intrinsic modulus of GO.

This synergistic mechanical reinforcement effect is not only obtained through the addition of GO but a result of a change in polymer modification. For this the orientation of the polymer crystals is studied by WAXD, showing that solution casting leads to preferred orientation of the PVA crystal along the thickness of the nanocomposite films which is not modified after the addition of GO.

In short, solution casting of PVA-GO, lead to well dispersed and exfoliated GO nanocomposites with no re-agglomeration. All of these are key factors in creating nanocomposites with good mechanical reinforcing efficiency. However, in order to get maximum levels of reinforcement, the GO particles have to be aligned along the sample thickness. At low filler content, the GO sheets a randomly oriented in the matrix, however, this alignment can be achieved through post-processing methods such as cold drawing. This will be the investigated in the following chapter.

5.5. References

1. Fiedler, Bodo, Gojny, Florian H., Wichmann, Malte H. G., Nolte, Mathias C. M., and Schulte, Karl, Composites Science and Technology, 2006. **66**(16): p. 3115-3125.
2. Ciselli, P., Wang, Z., and Peijs, T., Materials Technology, 2007. **22**: p. 10-21.
3. Young, Robert J., Kinloch, Ian A., Gong, Lei, and Novoselov, Kostya S., Composites Science and Technology, 2012. **72**(12): p. 1459-1476.
4. Moniruzzaman, Mohammad and Winey, Karen I., Macromolecules, 2006. **39**(16): p. 5194-5205.
5. Li, Yuan-Qing, Yu, Ting, Yang, Tian-Yi, Zheng, Lian-Xi, and Liao, Kin, Advanced Materials, 2012. **24**(25): p. 3426-3431.
6. Zhao, Xin, Zhang, Qinghua, Chen, Dajun, and Lu, Ping, Macromolecules, 2010. **43**(5): p. 2357-2363.
7. Hofmann, Ulrich and Holst, Rudolf, Berichte der deutschen chemischen Gesellschaft (A and B Series), 1939. **72**(4): p. 754-771.
8. Ruess, G. , Monatshefte für Chemie, 1947. **76**: p. 381-417.
9. Scholz, W. and Boehm, H. P., Zeitschrift für anorganische und allgemeine Chemie, 1969. **369**(3-6): p. 327-340.
10. Nakajima, T., Mabuchi, A., and Hagiwara, R., Carbon, 1988. **26**(3): p. 357-361.
11. Szabó, Tamás, Berkesi, Ottó, Forgó, Péter, Josepovits, Katalin, Sanakis, Yiannis, Petridis, Dimitris, and Dékány, Imre, Chemistry of Materials, 2006. **18**(11): p. 2740-2749.
12. Lerf, Anton, He, Heyong, Forster, Michael, and Klinowski, Jacek, The Journal of Physical Chemistry B, 1998. **102**(23): p. 4477-4482.
13. Erickson, Kris, Erni, Rolf, Lee, Zonghoon, Alem, Nasim, Gannett, Will, and Zettl, Alex, Advanced Materials, 2010. **22**(40): p. 4467-4472.
14. Stankovich, Sasha, Piner, Richard D., Nguyen, SonBinh T., and Ruoff, Rodney S., Carbon, 2006. **44**(15): p. 3342-3347.
15. Dreyer, Daniel R., Park, Sungjin, Bielawski, Christopher W., and Ruoff, Rodney S., Chemical Society Reviews, 2010. **39**(1): p. 228-240.
16. Lee, Changgu, Wei, Xiaoding, Kysar, Jeffrey W., and Hone, James, Science, 2008. **321**(5887): p. 385-388.
17. Suk, Ji Won, Piner, Richard D., An, Jinho, and Ruoff, Rodney S., ACS Nano, 2010. **4**(11): p. 6557-6564.
18. Zhou, Tiannan, Chen, Feng, Liu, Kai, Deng, Hua, Zhang, Qin, Feng, Jiwen, and Fu, Qiang, Nanotechnology, 2011. **22**(4): p. 045704.
19. Liang, J. J., Huang, Y., Zhang, L., Wang, Y., Ma, Y. F., Guo, T. Y., and Chen, Y. S., Advanced Functional Materials, 2009. **19**(14): p. 2297-2302.

20. Putz, Karl W., Compton, Owen C., Palmeri, Marc J., Nguyen, SonBinh T., and Brinson, L. Catherine, Advanced Functional Materials, 2010. **20**(19): p. 3322-3329.

21. Xu, Yuxi, Hong, Wenjing, Bai, Hua, Li, Chun, and Shi, Gaoquan, Carbon, 2009. **47**(15): p. 3538-3543.

22. Zhao, Xin, Zhang, Qinghua, Hao, Yanping, Li, Yingzhi, Fang, Ying, and Chen, Dajun, Macromolecules, 2010. **43**(22): p. 9411-9416.

23. Hummers, William S. and Offeman, Richard E., Journal of the American Chemical Society, 1958. **80**(6): p. 1339-1339.

24. Yu, Junrong, Grossiord, Nadia, Koning, Cor E., and Loos, Joachim, Carbon, 2007. **45**(3): p. 618-623.

25. Tkalya, Evgeniy, Ghislandi, Marcos, Alekseev, Alexander, Koning, Cor, and Loos, Joachim, Journal of Materials Chemistry, 2010. **20**(15): p. 3035-3039.

26. Paredes, J. I., Villar-Rodil, S., Martínez-Alonso, A., and Tascón, J. M. D., Langmuir, 2008. **24**(19): p. 10560-10564.

27. Mkhoyan, K. A., Contryman, A. W., Silcox, J., Stewart, D. A., Eda, G., Mattevi, C., Miller, S., and Chhowalla, M., Nano Letters, 2009. **9**(3): p. 1058-1063.

28. Mahmoud, Waleed E., European Polymer Journal, 2011. **47**(8): p. 1534-1540.

29. Shi, Heguang, Li, Yue, and Guo, Tianying, Journal of Applied Polymer Science, 2013. **128**(5): p. 3163-3169.

30. Bao, Chenlu, Guo, Yuqiang, Song, Lei, and Hu, Yuan, Journal of Materials Chemistry, 2011. **21**(36): p. 13942-13950.

31. Robert F. Landel, Lawrence E. Nielsen. Mechanical Engineering. 1993 CRC Press; 2 edition.

32. Cadek, M., Coleman, J. N., Barron, V., Hedicke, K., and Blau, W. J., Applied Physics Letters, 2002. **81**(27): p. 5123-5125.

33. Cai, Dongyu and Song, Mo, Nanotechnology, 2009(31): p. 315708.

34. Holland, B. J. and Hay, J. N., Polymer, 2001. **42**(16): p. 6775-6783.

35. Probst, Olga, Moore, Eric M., Resasco, Daniel E., and Grady, Brian P., Polymer, 2004. **45**(13): p. 4437-4443.

36. Wang, Zhujuan, School of Engineering and Materials Science, Queen Mary University of London, 2007

37. Cheung, Man Ken, Wan, Kris P. Y., and Yu, Peter H., Journal of Applied Polymer Science, 2002. **86**(5): p. 1253-1258.

38. Peppas, Nikolaos A. and Merrill, Edward W., Journal of Applied Polymer Science, 1976. **20**(6): p. 1457-1465.

39. Li, Chengpeng, Vongsvivut, Jitraporn, She, Xiaodong, Li, Yongzhen, She, Fenghua, and Kong, Lingxue, Physical Chemistry Chemical Physics, 2014. **16**(40): p. 22145-22158.

40. Lee, Seungae, Hong, Jin-Yong, and Jang, Jyongsik, Polymer International, 2013. **62**(6): p. 901-908.

41. Qi, Y. Y., Tai, Z. X., Sun, D. F., Chen, J. T., Ma, H. B., Yan, X. B., Liu, B., and Xue, Q. J., Journal of Applied Polymer Science, 2013. **127**(3): p. 1885-1894.

42. Zhu, Jian, Zhang, Huanan, and Kotov, Nicholas A., ACS Nano, 2013. **7**(6): p. 4818-4829.

43. Yang, Xiaoming, Li, Liang, Shang, Songmin, and Tao, Xiao-ming, Polymer, 2010. **51**(15): p. 3431-3435.

44. Salavagione, H. J., Martinez, G., and Gomez, M. A., Journal of Materials Chemistry, 2009. **19**(28): p. 5027-5032.

45. Starr, Francis W., Schrøder, Thomas B., and Glotzer, Sharon C., Macromolecules, 2002. **35**(11): p. 4481-4492.

46. Naebe, Minoo, Lin, Tong, Staiger, Mark P, Dai, Liming, and Wang, Xungai, Nanotechnology, 2008. **19**(30): p. 305702.

47. Zhang, Xiefei, Liu, Tao, Sreekumar, T. V., Kumar, Satish, Hu, Xiaodong, and Smith, Ken, Polymer, 2004. **45**(26): p. 8801-8807.

48. Assender, Hazel E. and Windle, Alan H., Polymer, 1998. **39**(18): p. 4295-4302.

49. Xu, Jia-Zhuang, Chen, Tao, Yang, Chuan-Lu, Li, Zhong-Ming, Mao, Yi-Min, Zeng, Bao-Qing, and Hsiao, Benjamin S., Macromolecules, 2010. **43**(11): p. 5000-5008.

50. Xu, Jia-Zhuang, Liang, Yuan-Ying, Zhong, Gan-Ji, Li, Hai-Long, Chen, Chen, Li, Liang-Bin, and Li, Zhong-Ming, The Journal of Physical Chemistry Letters, 2012. **3**(4): p. 530-535.

51. Cheng, Shan, Chen, Xi, Hsuan, Y. Grace, and Li, Christopher Y., Macromolecules, 2011. **45**(2): p. 993-1000.

52. Strawhecker, K. E. and Manias, E., Chemistry of Materials, 2000. **12**(10): p. 2943-2949.

53. Wang, Zhujuan, Ciselli, Paola, and T Peijs, Nanotechnology, 2007. **18**(45): p. 455709.

54. Smith, P., Lemstra, P. J., Pijpers, J. P. L., and Kiel, A. M., Colloid and Polymer Science, 1981. **259**(11): p. 1070-1080.

Chapter 6

Oriented PVA-GO nanocomposites by uni-axial drawing

6.1. Introduction

Sonication supported solution casting is an efficient method to obtain well dispersed and exfoliated nanoparticles in a polymer matrix. As shown in the previous chapter, in solution cast PVA-GO nanocomposite films a good reinforcing efficiency is achieved with well exfoliated and dispersed GO particles. For instance, in these nanocomposites the addition of 0.5 wt.% GO increased the glass transition temperature by 8 °C, and the Young's modulus of the nanocomposites by 36 %, which corresponded to a high filler efficiency as a result of filler reinforcement as well as modification of the polymer matrix.

Such high reinforcement efficiency is not all that common for nanocomposite system. Carbon nanotube (CNT) based nanocomposites often exhibit disappointing mechanical properties as summarised by Ciselli et al. [1]. For example, Dalton et al. [2] presented a nanocomposite as tough as spider silk based on 60 wt.% SWNTs in PVA matrix. However, in this nanocomposite the effective Young's modulus for the SWNT is only 147 GPa which is around 15 % of the intrinsic modulus of SWNTs, while the effective tensile stress carried by the nantube is 3 GPa [1]. These reinforcement properties are comparable to those of ordinary carbon fibres and well below the potential of SWNTs. To fully exploit the potential of 1D or 2D nanofillers, it is also needed to orientate these fillers. Moreover, as described previously, and in the case of graphene flake, high shearing can also lead to folding, buckling, or scrolling of the graphene sheets in the polymer matrix, thus lowering their effective aspect ratio and reducing the potential of graphene as reinforcement.

In order to further improve the potential of graphene as reinforcement for nanocomposites, it is important to develop post treatments which can align, straighten or unfold the graphene sheets in the matrix. Highly oriented CNT nanocomposites after uniaxial stretching showed a high level of alignment of the CNTs in the polymeric matrix [3-6]. In addition, these studies showed that such uniaxially drawn nanocomposites can achieve close to the theoretical reinforcing efficiency. Several studies have shown that biaxial stretching is another effective post treatment able to exfoliated and oriented 2D nanoclays in polymer matrices [7-9].

In this study, we post-drawn traditional solution cast nanocomposite films of PVA-GO at 0.05, 0.1 and 0.5 wt.% loading to different drawing ratios, in order to align these GO nanosheets. The mechanical and thermal properties of these oriented

nanocomposites are studied and addressed in function of the alignment of the nanoparticles and on the polymer morphology.

6.2. Experimental

6.2.1 Materials

The poly(vinyl alcohol) is supplied by Sigma Aldrich (Mw ~85,000 - 124,000 $g.mol^{-1}$, 98-99 % hydrolyzed). GO is obtained by Hummer's method and provided by Sichuan University.

6.2.2 Preparation

The same protocol is used as described in Chapter 5. Poly(vinyl alcohol) is dissolved in deionised (DI) water at 90 °C and continuously stirred for 4 hrs, to give a homogeneous solution at 10 wt.% loading. This PVA solution is then cooled down to room temperature. GO solution is obtained by dispersing the GO in deionised water at 1 $mg.mL^{-1}$ using a high-power ultrasonication tip (Sonics VCX 500) (amplitude of sonication is set to 20 %, the pulser to 2 sec on / 2 sec off and the energy time is modified in function of the experiment). GO suspension is left aside for at least 12 hrs to let thicker graphite aggregates to precipitate. The right volume of GO solution is then drop wise added into the PVA solution and stirred for 4 hrs at room temperature. The solution is left aside for 12 hrs to allow the solution to degas and then the solution is cast in a PS petri-dish to dry for 5 days under ambient conditions in a fume-hood. All the samples are stored in a desiccator to prevent the moisture absorption by the PVA.

Solid-state post-drawing of the nanocomposite films is performed in an environmental chamber (Instron) at 90 °C, i.e. above *Tg* but below the melting temperature, and then quenched to room temperature. Post-drawing is performed in an environmental chamber (Instron 3119-405-22), on films with a width of 4 mm and a length of 40 mm at a drawing speed of 10 mm.min^{-1}. Draw-ratio is obtained as follows: $\lambda = \frac{l_1}{l_0}$

6.2.3 Characterization

Like in Chapter 5, Atomic Force Microscopy is performed using a NT-MDT in tapping mode. GO exfoliated by sonication is here diluted to 0.1 mg.mL^{-1} and then sprayed onto a freshly cleaved mica sheet. AFM is performed in tapping mode using a three-points head.

Scanning Electron Microscopy is performed using a FEI Inspector-F scanning electron microscope. Samples were observed at a working distance of 10 mm and at 5 kV. Prior to the observation all samples are gold coated.

Dynamic Mechanical Analysis is performed by a DMA Q800 V7.5. The DMA is performed in tension mode (1 Hz) at a temperature range from – 50 °C to 240 °C at 3 °C.min^{-1}.

Differential Scanning Calorimetry is performed using a Mettler DSC 822e differential scanning calorimeter. 6 – 7 mg of material is used for each experiment. The method consists of two heating and two cooling scans. The two heating scans are from 20 °C to 235 °C at a rate of 10 °C.min^{-1} and the two cooling scans are from 235 °C to 20 °C at 30 °C.min^{-1}.

Wide Angle X-Ray Diffraction data are obtained using a Panalytical Xpert Pro diffractometer with a Cu-Kα source at a distance of 8 mm and at a wavelength of 1.54 Å. The reference sample used is aluminium oxide. The number of pixel detectors is 4096*4096 with a size of 15.137 µm. The 2D data are transformed into 1D data using the software FIT2D.

Tensile tests are performed using an Instron 5586 at room temperature, equipped with a load cell of 1 kN at a test speed of 10 $mm.min^{-1}$ and a 20 mm gauge length. The sample width is between 1.5 and 1.6 mm with a thickness between 0.05 and 0.09 mm

6.3. Results and discussion

Post-drawing of the tapes is conducted below the melting point of the PVA, i.e. at 90 °C. This solid-state drawing process induces crystal or chain orientation and is successfully used for the creation of a wide range of high performance synthetic fibres based on flexible chain polymer molecules [10]. Figure 6.1 presents the mechanical behaviour of pure PVA tapes at different draw-ratios.

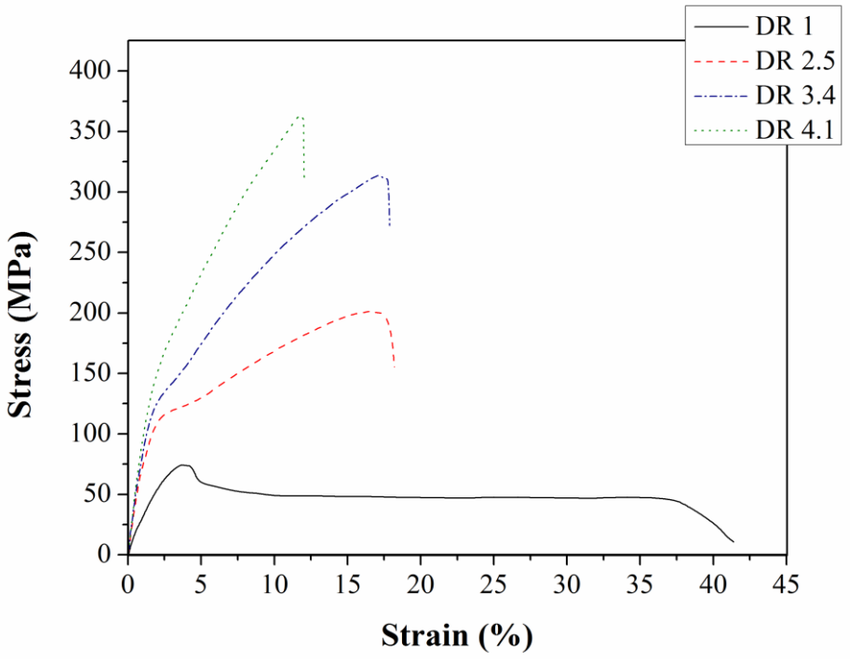

Figure 6.1: Stress-strain curves of pure PVA tapes at different draw-ratios.

Clearly the post-drawing process significantly improves the mechanical properties of the PVA tapes under tension (Figure 6.1). At draw ratio 1, i.e. non-oriented tapes, the PVA tapes behave as a ductile material. As the draw-ratio increases, both Young's modulus and tensile strength increases significantly, while as expected the strain at break is strongly reduced.

Drawing of semi-crystalline polymers has been reported as an efficient way to improve mechanical properties through chain orientation and chain extension [11, 12]. For instance, in the case of ultra-high molecular weight polyethylene (UHMW-PE) solution (gel) spinning can lead to ultra-drawability with draw-ratios exceeding 40, yielding Young's moduli and tensile strengths in excess of 100 and 3 GPa [13]. Drawing semi-crystalline polymers can be described by the drawing of two interpenetrated networks based on interlocked lamella and an entangled amorphous phase [14]. The drawing of semi-crystalline polymer is described in three main

stages by Peterlin [15]. At low drawing ratio, an elastic and plastic deformation of the lamellar structure occurs. Further deformation leads to the rotation of the crystalline region and fragmentation of the crystal lamella where the lamella break into smaller folded chains blocks (see in Figure 6.2 a). The final post-drawing step, which occurs at very high drawing ratio (see in Figure 6.2 b), consists in the plastic deformation of the fibrils where chains unfold to form needle-like crystal [15-17].

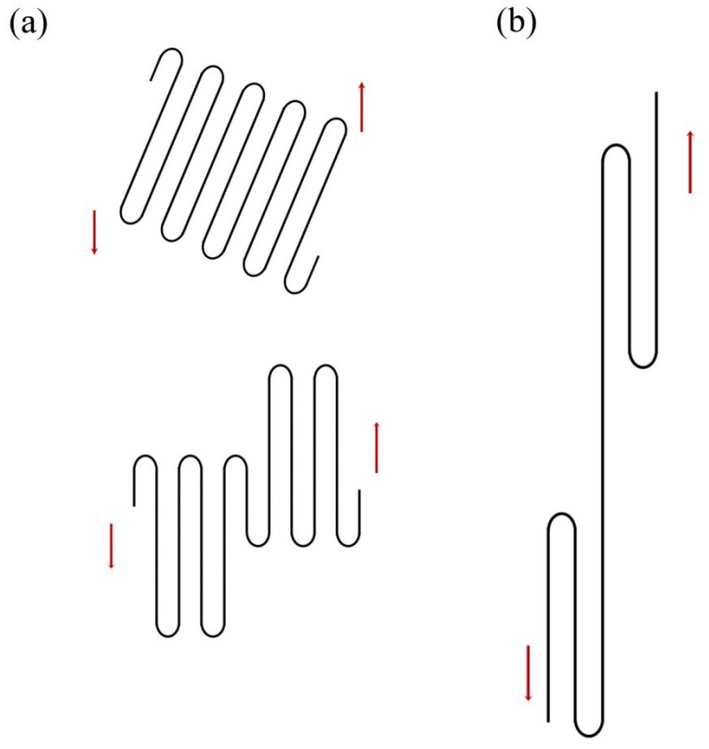

Figure 6.2: Representation of crystal rotation and fragmentation (a) and the deformation into needle-like structure (b) during solid-state drawing, reproduced from [16-17].

PVA is a semi-crystalline polymer with flexible linear chains similar to PE. Several papers have studied the drawability of PVA [5, 11, 18, 19]. Schellekens et al. [11] studied the drawability of PVA and the mechanical properties compared to PE. It is

shown that the stronger intermolecular interactions present in PVA i.e. hydrogen bonding versus van der Waals, confer a lower drawability than in PE.

Drawing of polymer nanocomposites has two majors effect: orientation of the polymer chains as previously discussed but simultaneously also orientation of the 1D or 2D nanofiller. For instance, uniaxial stretching of PVA-SWNT composites is studied by Wang et al. [3, 4]. They observed that the drawing of the PVA nanocomposites resulted in an alignment of both polymer and CNTs, leading to a dramatic increase in the reinforcing potential of the CNTs in the polymer matrix.

6.3.1 Study of the orientation

The effect of post-drawing on the polymer morphology is observed by electron microscopy and presented in Figure 6.3.

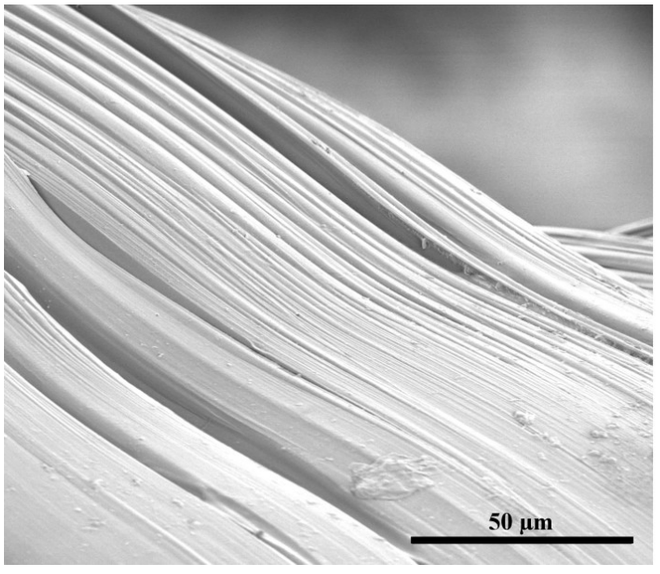

Figure 6.3: SEM image of PVA tape at draw ratio 4.

At draw ratio 4, the micrograph shows a remarkable alignment of the polymer tape. The picture also reveals the formation of oriented fibrils along the drawing direction. The formation of fibrils is a consequence of the drawing process and constitutes of

very long, packed and oriented microfibrils with a lateral dimension *d* between 100 and 200 Å [20]. Unfortunately, GO platelets are not observed.

The molecular orientation is further studied by X-ray diffraction in through transmission direction.

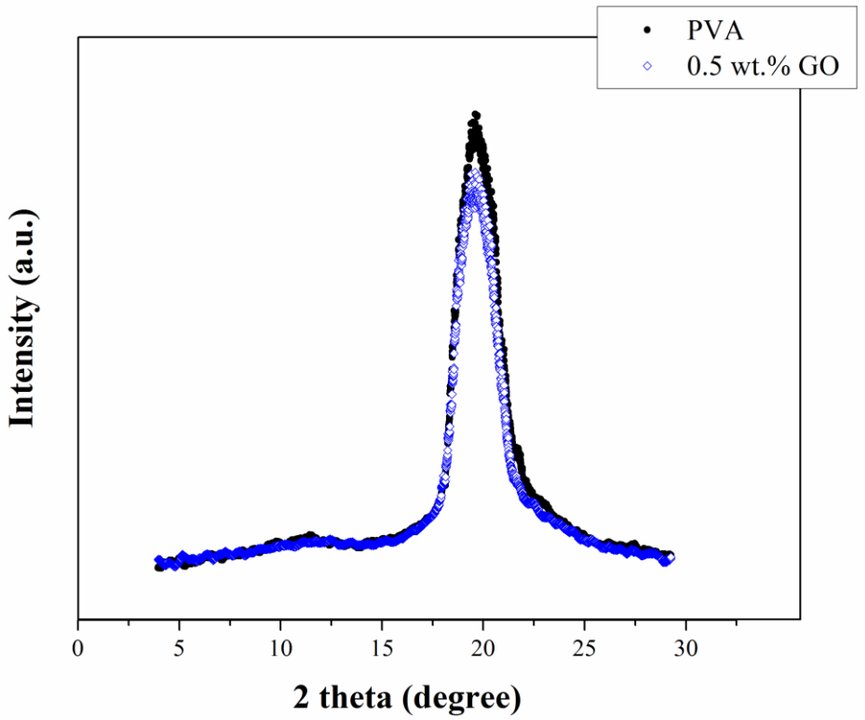

Figure 6.4: Diffraction pattern of drawn PVA and PVA/GO at 0.5 wt.% and draw ratio 4.

The diffraction patterns of drawn PVA and PVA nanocomposites presents an intense and wide peak at $2\theta = 19.4°$. Like previously shown in paragraph 5.3.6, this peak corresponds to the doublet $10\bar{1}$ and 101 crystalline reflexion [21, 22]. The X-ray data provides evidences that neither the drawing, nor the addition of GO creates any new crystalline phases in the nanocomposites. The orientation of the polymer is observed and are summarised in Table 6.1.

Table 6.1: Diffraction pattern of PVA and PVA nanocomposites measured through the film thickness at draw ratio 0, 2 and 4.

	Non Drawn	**DR2**	**DR4**
PVA	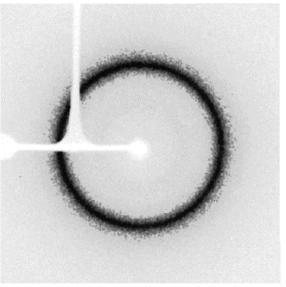	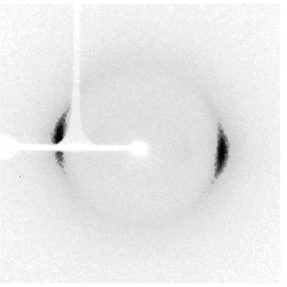	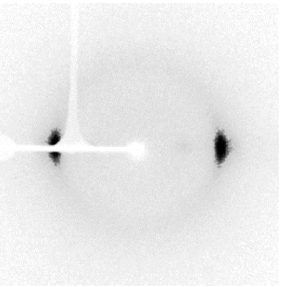
0.05 wt. % GO	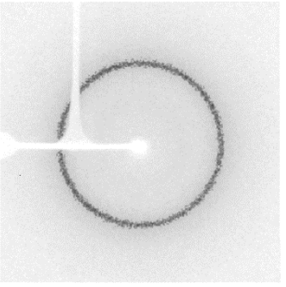	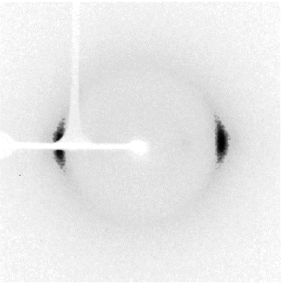	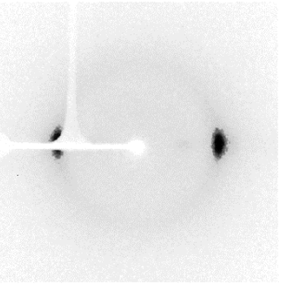
0.5 wt.% GO	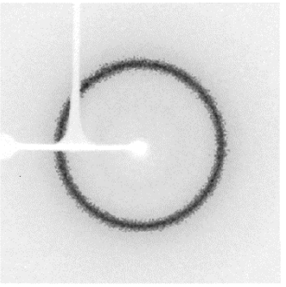	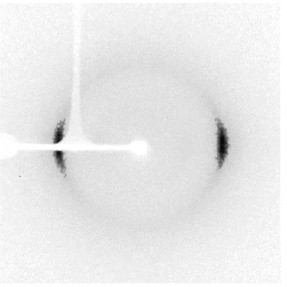	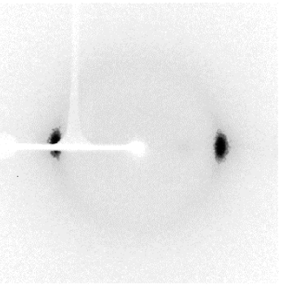

The diffraction patterns of undrawn PVA and PVA nanocomposites show a fully isotropic ring, which indicate that there is no preferential orientation of the crystals even after addition of GO. In contrary, the diffraction patterns of the drawn samples show a clear orientation of the polymer in agreement with literature [23, 24]. The diffraction arc of all samples at draw ratio 4 is reduced compared to draw ratio 2, indicating a better orientation of the polymer crystals. To illustrate the orientation of

the polymer during the drawing, the intensity of pure PVA and PVA-GO at 0.5 wt.% are integrated and plotted versus the azimuthal angle as presented in Figure 6.5.

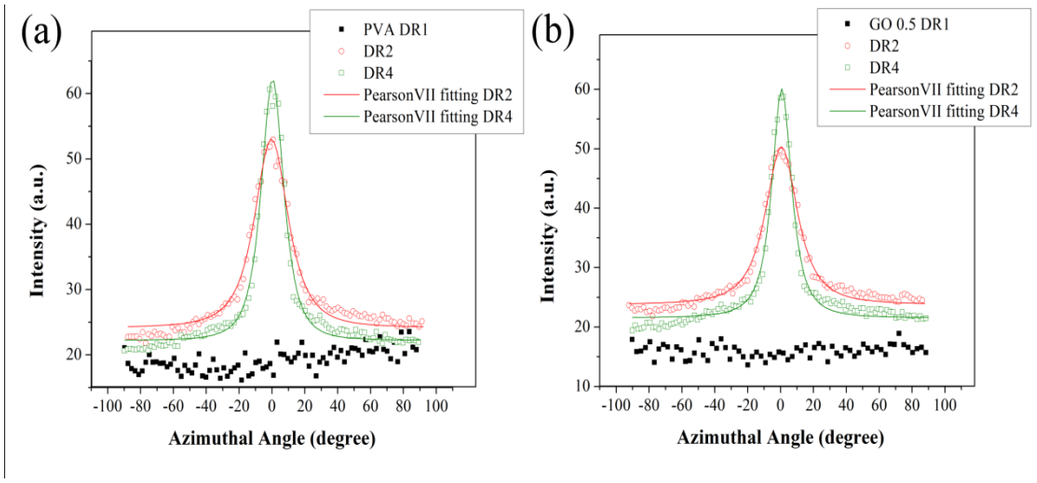

Figure 6.5: Variation of the intensity measured for (a) PVA and (b) PVA-GO 0.5 wt.% nanocomposites at draw ratio 1, 2 and 4. The solid lines represent a PearsonVII fitting where the FWHM are calculated.

As previously presented, at draw ratio 1, i.e. undrawn samples, a randomly oriented crystal structure is observed in both pure PVA and PVA nanocomposite. At draw ratio 2 and 4, no clear difference is observed between neat PVA and PVA nanocomposites. A peak is observed describing the orientation of the crystals along the drawing direction. As the draw ratio increases the peak narrows, indicating alignment of the crystals. The peaks are fitted with a PearsonVII to determine the FWHM and summarised in Table 6.2

Table 6.2: FWHM of the intensity peaks of PVA nanocomposites at draw ratio 2 and 4, calculated with a Pearson VII fitting.

	FWHM *(deg)*		
	PVA	**0.05 wt.% GO**	**0.5 wt.% GO**
DR2	24.2°	19.9°	23.1°
DR4	16.1°	15.4°	14.2°

The orientation factor is estimated based on of the FWMH obtain with a Pearson VII fitting following equation [19]:

$$F = \frac{180 - FWMH}{180} \qquad 6.1$$

This orientation factor is plotted for draw ratio 2 and 4 in Figure 6.6

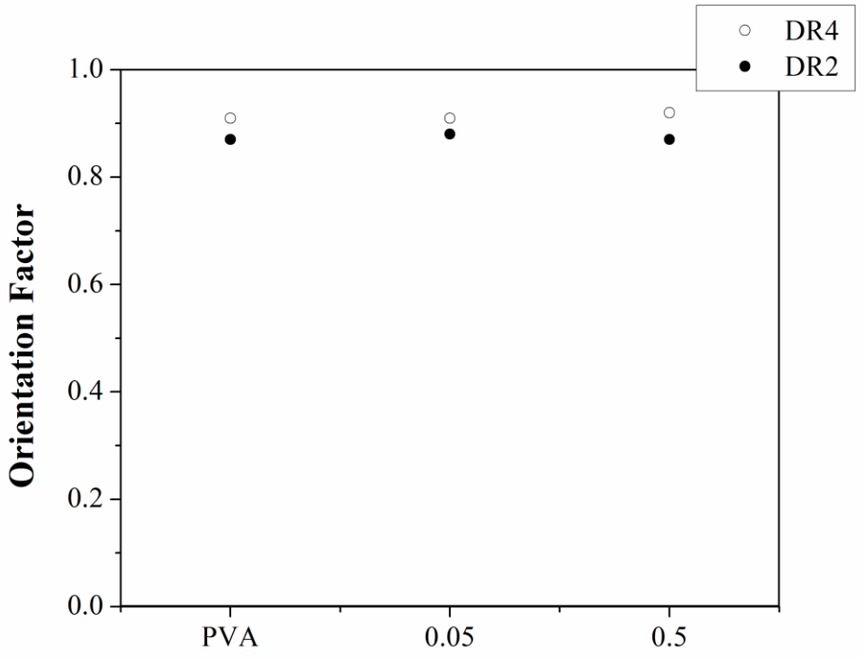

Figure 6.6: Orientation factor calculated using Equation 7.1 for PVA and PVA nanocomposites at draw ratio 2 and 4.

Figure 6.6 presents the variation of the orientation factors with the addition of GO for different drawing ratios. Random orientation and full orientation are defined by an orientation factor tending to 0 and 1, respectively. As seen in Figure 6.6, at draw ratio 2 as well as draw ratio 4, the addition of GO does not affect the alignment of the PVA crystals since orientation factors are similar. At draw ratio 4, the orientation factor is ~0.9, which is an indication of good alignment of the crystals. At draw ratio 2, the orientation factor is slightly lower than at draw ratio 4, however it still indicates some molecular orientation.

In addition, it is expected that GO flakes are oriented during the polymer drawing. Previous studies on CNTs and needle-like clays show a high degree of alignment of CNTs after uniaxial drawing [6, 25-27]. Orientation of the CNTs has been assessed

by Raman spectroscopy and TEM. Orientation of GO in PVA matrix after uniaxial drawing as observed by SEM is reported by Morimune et al. [28]. Orientation of 2D fillers like layered clays [7-9] or mica [29] has been studied by bi-axial stretching. Similar to uniaxial drawing, here a high degree of alignment of the filler was achieved (see Figure 6.7). In addition the authors observed that drawing can lead to better exfoliation of the particles.

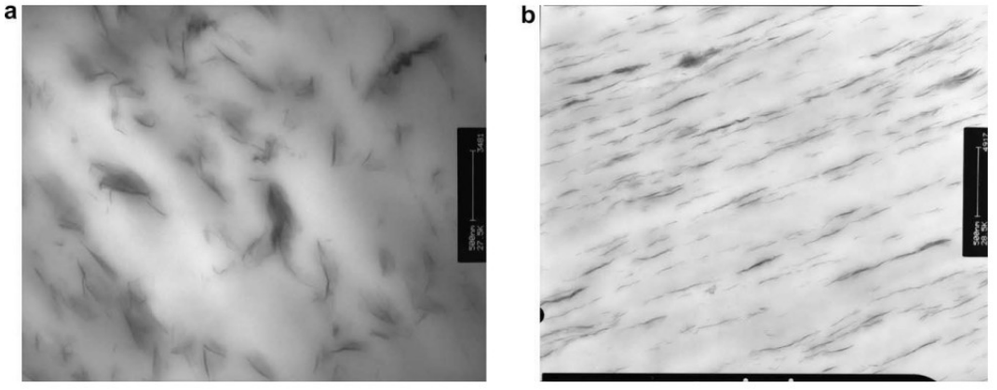

Figure 6.7: TEM image of PP clays nanocomposites; (a) undrawn and (b) drawn at draw-ratio 3.5 [8]. The scale bar represents 500 nm.

6.3.2 Thermal properties

The thermal properties of the drawn tapes are studied by DSC. Only, the first heating is studied since the molecular orientation induced by the drawing process will disappeared after the first heating cycle. The data of drawn PVA and PVA nanocomposites at draw ratio 4 is summarised in Table 6.3.

Table 6.3: DSC measurements of PVA and PVA-GO nanocomposites at draw ratio 4, during the first heating ($_1$) only.

	Tm_1 (°C)	**ΔQm_1 ($J.g^{-1}$)**	**X_1 (%)**
PVA	222.3	65.0	46.9
0.05 wt.% GO	222.9	62.4	45.0
0.1 wt.% GO	223.9	63.3	45.7
0.5 wt.% GO	222.6	62.1	44.8

The melting temperature of drawn PVA crystals is measured at 222 ºC which is similar to undrawn PVA. This melting temperature is not affected by the addition of GO, which indicates that the crystal size is not modified. To further investigate the effect of drawing, the degree of crystallinity is studied. The degree of crystallinity is estimated following Equation 6.9 based on the melt enthalpy. The degree of crystallinity of pure drawn PVA is measured at around 46.9%. The addition of GO leads to a small reduction in crystallinity. A reduction in crystallinity is already observed for isotropic nanocomposites and presented in paragraph 5.3.3. Interestingly, the degree of crystallinity of the drawn PVA is 7 % higher than for undrawn PVA as listed in Table 5.1. This increase in crystallinity with drawing has been reported for a number of semi-crystalline polymers [18, 30] and is known as stress-induced crystallinity. Wu et al. [18] described the crystallisation process of PVA during drawing in three steps: (i) during elastic deformation the crystallinity increases slightly , (ii) after necking crystallinity increases rapidly and at this stage amorphous chains and tied chains are oriented. The folded lamella chains are

gradually oriented along the drawing direction and form microfibrils which induce crystallisation. Finally, crystals start to unfold and are rearranged with tie chains which may form an extended crystalline phase (iii). This process is much slower and crystallinity will increase gradually with stress.

The changes in glass transition could not be observed by DSC since the *Tg* is observed only during the second heating scan. DMA is then carried out, to follow the change in the glass transition temperature with the addition of GO for drawn PVA; presented in Figure 6.8 and summarised in Table 6.4.

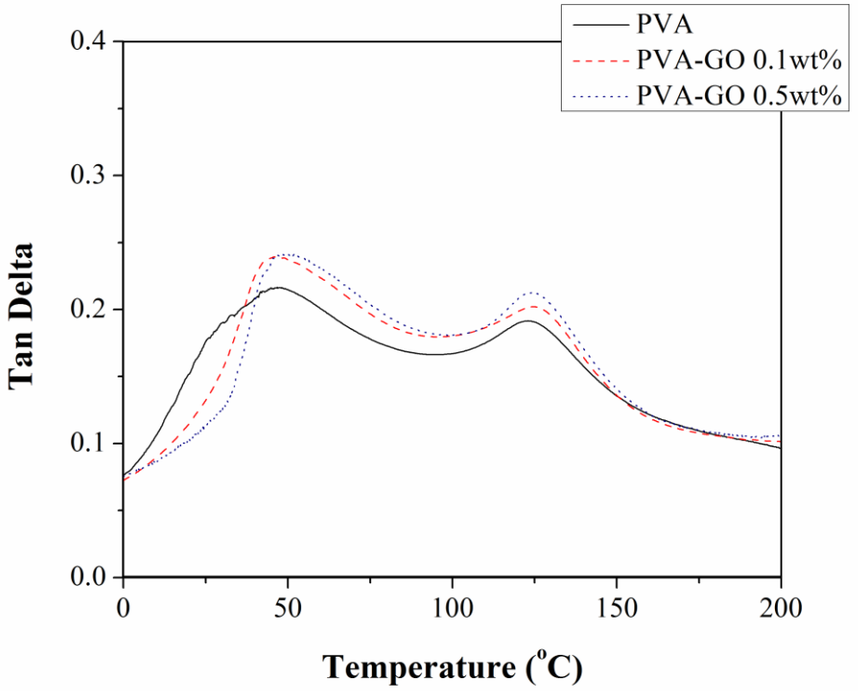

Figure 6.8: DMA spectra of PVA/GO nanocomposites at draw ratio 4, showing *tan δ* in function of temperature.

As previously observed in paragraph 5.3.3, the mechanical loss tangent of the PVA films presents two peaks. Briefly, the first peak, T_α, corresponds to the α_a relaxation of the amorphous phase and describes the glass transition temperature of the PVA.

The second peak at higher temperature, on the other hand, T_β, corresponds to the β_c relaxation of the crystalline phase of the PVA. In drawn PVA and PVA nanocomposites both relaxations peaks are present.

The drawing of the polymer leads to a major increase of the first peak associated to the glass transition temperature. The T_α of drawn PVA is 47 °C, whereas the T_α of isotropic solution-cast PVA is measured at 35 °C (see paragraph 5.3.3). This increase of 12 °C is believed to be due to confinement of the polymer chains after drawing. However, this effect is lowered for PVA nanocomposites as the chains are already confined by the addition GO. In another word, the glass transition temperature is more influenced by the confinement due to drawing than due to the addition of GO.

The relaxation of the crystalline phase of drawn PVA, $T_{\beta,}$ is measured at 123 °C. The temperature of crystalline relaxation is not modified with the addition of GO, indicating no interaction between GO and the crystalline phase.

It is worth noting that for both pure and PVA nanocomposites the intensity of the T_α peaks are reduced compared to those for isotropic solution-cast films. Or in other words for drawn PVA and PVA nanocomposites the intensity of the T_β peaks are comparable to the T_α peaks. This is an indication that the drawn tapes have a higher crystallinity than solution-cast films and is in agreement with the DSC results.

Table 6.4: Summary from DMA presenting T_α and T_β of PVA-GO nanocomposites at draw ratio 4.

	T_α (°C)	T_β (°C)
PVA	47	123
0.1 wt.% GO	46	124
0.5 wt.% GO	48	124

6.3.3 Mechanical properties

The mechanical properties of the drawn nanocomposite tapes are investigated by tensile testing.

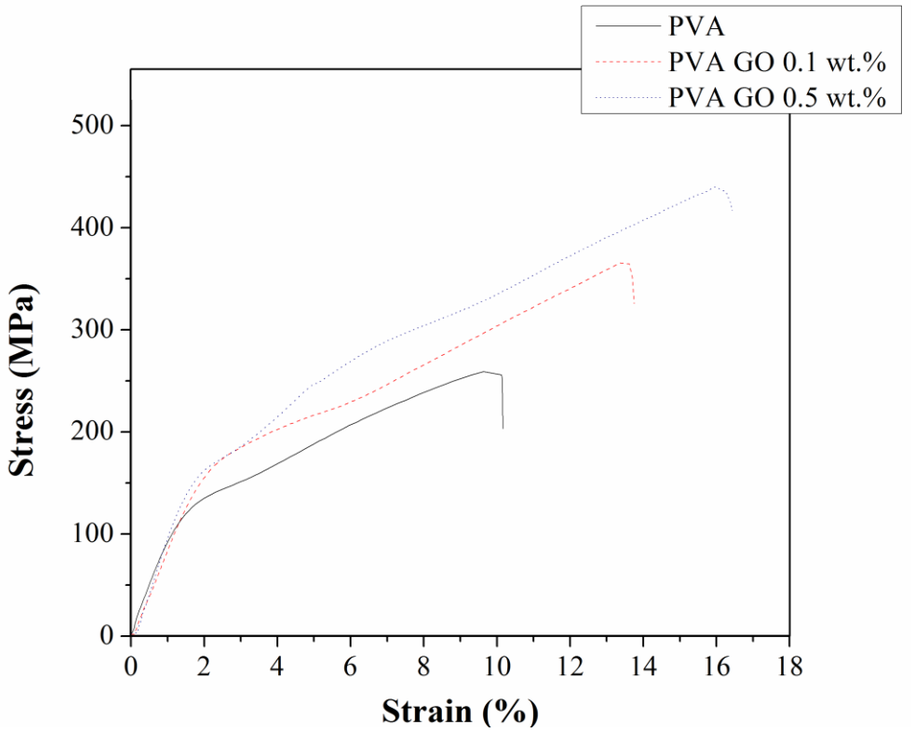

Figure 6.9: Stress-strain curves of PVAGO nanocomposites of draw ratio 4 at different GO loadings.

The addition of GO enhanced the mechanical properties of the oriented nanocomposites. Interestingly, the toughness of the samples is improved together with the Young's modulus and ultimate tensile strength (UTS). For example, the addition of 0.5 wt.% GO, increased the Young's modulus and strength with around 3 % and 35 %, respectively. In addition the strain at break is improved by 49 %. The toughness is calculating by measuring the area underneath the stress-strain curve and listed in Table 6.5. Toughness is doubled with the addition of 0.5 wt.% GO. This increase in toughness is believed to be due to the reduction of the degree of crystallinity as well as the well dispersed and oriented 2D particles which enhances the tortuosity during crack propagation. In addition to that, other mechanisms may

also be involved such as delamination at the polymer/GO interface or delamination of weak GO aggregates, and/or crack deflection.

Table 6.5: Summary of mechanical properties of PVA and PVA-GO nanocomposites at draw ratio ~4. The values are means ± standard deviation. The toughness is simply measured by calculating the area under the curve. The data are obtained on a minimum of 3-5 samples.

	Drawing	**Young's modulus** *(GPa)*	**Tensile strength** *(MPa)*	**Strain at break** *(%)*	**Toughness** *($MJ.m^{-3}$)*
PVA	4.0 ± 0.1	11.9 ± 0.1	335 ± 41	10.1 ± 1.2	23.08 ± 6.4
0.05 wt.% GO	3.9 ± 0.1	12.0 ± 0.1	361 ± 50	10.6 ± 2.3	27.4 ± 6.2
0.1 wt.% GO	3.9 ± 0.1	12.2 ± 0.1	419 ± 54	13.2 ± 3.8	39.31 ± 16.5
0.5 wt.% GO	4.0 ± 0.1	12.3 ± 0.1	452 ± 41	15.1 ± 3.9	43.41 ± 11.2

Similar to the isotropic GO nanocomposites in Chapter 5, the reinforcing efficiency of the GO in the oriented PVA matrix is back-calculated using Halpin-Tsai model [31, 32], as presented in paragraph 5.3.5. A PVA nanocomposite with 0.5 wt.% GO loading is considered, where the GO platelets are oriented with a thickness of 1.6 nm and a diameter of 400 nm. For this system, the back-calculated effective Young's modulus of GO is around 150 GPa, which is 72.5 % of the intrinsic modulus of GO, i.e. 207 GPa [33]. As such it is highly plausible that the reinforcement observed in oriented PVA nanocomposites is truly based on the reinforcement by GO without any artefacts from polymer modifications.

6.4. Conclusions

Here we present the mechanical properties of oriented PVA-GO nanocomposites as produced by solution casting films followed by solid-state drawing as a post treatment that aligns both polymer chains as well as the graphene oxide sheets. XRD of PVA crystals shows that alignment of the PVA crystals is already observed at draw ratio 2. More importantly it is shown that the morphology of the PVA crystals after drawing is not affected by the presence of GO sheets.

The thermal properties of the films are studied by DSC. The crystallinity of drawn pure PVA and PVA nanocomposites are higher than for undrawn samples as a result of strain-induced crystallisation. However, the overall crystallinity is slightly reduced with the addition of GO. DMA measurements revealed that soli-state drawing lead to an increase of the glass transition temperature of the PVA compared to isotropic undrawn samples. Interestingly, the glass transition temperature is similar for pure PVA and PVA nanocomposites, indicating that chain mobility is dominated by the drawing mechanism rather than the addition of GO. The mechanical properties of the oriented nanocomposite tapes are also improved with the addition of GO. For example, the addition of 0.5 wt.% GO increased the Young's modulus and the tensile strength by 3 % and 35 %, respectively. More importantly, the strain at break also increased with the addition of GO, leading to a significant increase in toughness of the oriented nanocomposites. For instance, the addition of 0.5 wt.% of GO doubled the toughness compared to pure PVA tapes.

Finally, it is shown that the oriented GO sheets in the PVA nanocomposites exhibited a good reinforcing efficiency. Back-calculated from composite theory, the effective modulus of the GO in the nanocomposites is estimated at around 150 GPa,

which is 72.5 % of the intrinsic Young's modulus of GO. These results show the importance to create GO nanocomposites with a good level of alignment, exfoliation and dispersion.

6.5. References

1. Ciselli, P., Wang, Z., and Peijs, T., Materials Technology, 2007. **22**: p. 10-21.
2. Dalton, Alan B., Collins, Steve, Munoz, Edgar, Razal, Joselito M., Ebron, Von Howard, Ferraris, John P., Coleman, Jonathan N., Kim, Bog G., and Baughman, Ray H., Nature, 2003. **423**(6941): p. 703-703.
3. Wang, Zhujuan, Ciselli, Paola, and T Peijs, Nanotechnology, 2007. **18**(45): p. 455709.
4. Wang, Zhujuan, School of Engineering and Materials Science, Queen Mary University of London, 2007
5. Miaudet, P., Badaire, S., Maugey, M., Derré, A., Pichot, V., Launois, P., Poulin, P., and Zakri, C., Nano Letters, 2005. **5**(11): p. 2212-2215.
6. Deng, H., Bilotti, E., Zhang, R., and Peijs, T., Journal of Applied Polymer Science, 2010. **118**(1): p. 30-41.
7. Abu-Zurayk, Rund, Harkin-Jones, Eileen, McNally, Tony, Menary, Gary, Martin, Peter, and Armstrong, Cecil, Composites Science and Technology, 2009. **69**(10): p. 1644-1652.
8. Abu-Zurayk, Rund, Harkin-Jones, Eileen, McNally, Tony, Menary, Gary, Martin, Peter, Armstrong, Cecil, and McAfee, Marion, Composites Science and Technology, 2010. **70**(9): p. 1353-1359.
9. Rajeev, R. S., Harkin-Jones, E., Soon, K., McNally, T., Menary, G., Armstrong, C. G., and Martin, P. J., European Polymer Journal, 2009. **45**(2): p. 332-340.
10. Ward, I.M. and Hadley, D.W. 1993: John Wiley & Sons Ltd.
11. Schellekens, R. and Bastiaansen, C., Journal of Applied Polymer Science, 1991. **43**(12): p. 2311-2315.
12. Yao, Jian, Bastiaansen, Cees, and Peijs, Ton, Fibers, 2014. **2**(2): p. 158-186.
13. Smith, P. and Lemstra, P. J., Colloid and Polymer Science, 1980. **258**(7): p. 891-894.
14. Men, Yongfeng, Rieger, Jens, and Strobl, Gert, Physical Review Letters, 2003. **91**(9): p. 095502.
15. Peterlin, A., Polymer Engineering & Science, 1977. **17**(3): p. 183-193.
16. Hu, W. G. and Schmidt-Rohr, K., Acta Polymerica, 1999. **50**(8): p. 271-285.
17. Séguéla, Roland, Macromolecular Materials and Engineering, 2007. **292**(3): p. 235-244.
18. Wu, Qian, Chen, Ning, and Wang, Qi, Journal of Polymer Research, 2010. **17**(6): p. 903-909.
19. Miyazaki, Tsukasa, Hoshiko, Akie, Akasaka, Midori, Sakai, Miki, Takeda, Yuuki, and Sakurai, Shinichi, Macromolecules, 2007. **40**(23): p. 8277-8284.
20. Peterlin, A., Colloid and Polymer Science, 1975. **253**(10): p. 809-823.

21. Assender, Hazel E. and Windle, Alan H., Polymer, 1998. **39**(18): p. 4295-4302.

22. Strawhecker, K. E. and Manias, E., Chemistry of Materials, 2000. **12**(10): p. 2943-2949.

23. Wu, Qian, Chen, Ning, Li, Li, and Wang, Qi, Journal of Applied Polymer Science, 2012. **124**(1): p. 421-428.

24. Wang, W., Ciselli, P., Kuznetsov, E., Peijs, T., and Barber, A. H., Philosophical Transactions of the Royal Society a-Mathematical Physical and Engineering Sciences, 2008. **366**(1870): p. 1613-1626.

25. Jin, L., Bower, C., and Zhou, O., Applied Physics Letters, 1998. **73**(9): p. 1197-1199.

26. Wang, Z., Ciselli, P., and Peijs, T., Nanotechnology, 2007. **18**(45).

27. Bilotti, Emiliano, Deng, Hua, Zhang, Rui, Lu, Dun, Bras, Wim, Fischer, Hartmut R., and Peijs, Ton, Macromolecular Materials and Engineering, 2010. **295**(1): p. 37-47.

28. Morimune, Seira, Kotera, Masaru, Nishino, Takashi, and Goto, Takuya, Carbon, 2014. **70**(0): p. 38-45.

29. Soon, Kok H., Harkin-Jones, Eileen, Rajeev, Rajvihar S., Menary, Gary, McNally, Tony, Martin, Peter J., and Armstrong, Cecil, Polymer International, 2009. **58**(10): p. 1134-1141.

30. Lu, X. F. and Hay, J. N., Polymer, 2001. **42**(19): p. 8055-8067.

31. Halpin, J.C. and Kardos, J.L. , Polymer Engineering and Science, 1976. **16**(5): p. 344 - 352.

32. Van Es, M, Technology University Delft, 2001

33. Suk, Ji Won, Piner, Richard D., An, Jinho, and Ruoff, Rodney S., ACS Nano, 2010. **4**(11): p. 6557-6564.

Chapter 7

Deposition of PVA and GO layers by spray-coating method

7.1. Introduction

The deposition of graphene monolayer is very attractive especially for applications such as solar cells [1-3], flexible devices [4] or hierarchical nanocomposite [5]. For this the deposition process needs to be reliable, reproductive, versatile, and scalable to large areas. Several methods to deposit monolayer are already available including spin-coating [6], ink-jet printing [7, 8], roller or dip coating [9] or electro-spraying [10, 11]. Spray coating is an attractive process as it can cover a large area, deposit a uniform layer and it is a well established processed for industrial coatings and paints.

Creating a monolayer by spraying method consists of an atomisation process of a solution, driven by air flows. The uniformity and the thickness of the layer are tuned

by controlled atomisation. In the case of polymeric layers, these layers are formed by singles droplets which coalesce on the substrate before drying [12]. However, in the case of nanoparticles, like GO, the solution is sprayed in a way to remove the solvent in order to limit the mobility of the particles once deposited onto the substrate [13].

In this study, the deposition of a layer of PVA and monolayers of graphene oxide is studied in order to obtain thin and homogeneous layers. In the case of PVA layer, the pressure and the distance between nozzle and substrate are first studied. These parameters allowed us to tune the atomisation of the polymer solution and control its surface topography. The concentration and the volume of solution are studied in function of the thickness of the polymer layer. The deposition of a monolayer of GO nanoparticles is also studied in order to obtain a uniform, homogeneous layer. Solvent type and volume of GO solution is studied and assessed in function of the surface coverage.

7.2. Experimental

7.2.1 Materials

PVA (Mw ~ 85,000-124,000 $g.mol^{-1}$, 98-99 % hydrolyzed), PMMA (Mw ~ 35 000 $g.mol^{-1}$), isopropanol and propylene glycol monomethyl ether acetate were purchased from Sigma Aldrich. Polystyrene (Empera 124N) was obtained from Ineos. GO is obtained by Hummer's method and provided by Sichuan University. Glass slides are supplied by VWR and Mica sheets, grade V-4, are supplied by SPI Supplies.

7.2.2 Preparation

PVA is dissolved in deionised water at 90 °C and continuously stirred for 4 hrs, to give a solution with a polymer concentration of 10 wt.%. The PVA solution is then cooled down to room temperature. This solution is then diluted to different concentrations. PS is dissolved in toluene at 80 °C and continuously stirred for 4 hrs, to give a homogeneous solution with 5 wt.% GO. Also PMMA is dissolved in PGMEA at 90 °C and continuously stirred for 4 hrs, to give a solution with a polymer concentration of 20 wt.%.

Graphene oxide solution is obtained by dispersing the GO in deionised water at 1 $mg.mL^{-1}$ by a high-power ultrasonication tip (Sonics VCX 500) (amplitude of sonication is set to 20 %, the pulser to 2 sec on / 2 sec off for 1000 J). GO suspension is left aside for at least 12 hrs to let thicker graphite aggregates to precipitate.

The glass slides substrates are cut to form a 4 cm^2 wafer. These wafers are then spin-coated (spincoater G3P-8 from SCS), with either PMMA or PS solution. The coating is achieved at 500 rpm for 1 min. The films are then left in the oven for 10 min at 60 °C, until fully dry.

PS is treated using a corona surface treater (BD20 from ETP). For a surface of 80 cm^2, the gun is placed 2 cm away from the wafer to avoid burning of the PS layer and applied for 4 min. Since the functionalisation of the PS layer decrease over time [14], spraying is always performed immediately after the treatment.

Spraying is performed using an Iwata airbrush HP-C Plus with an Iwata Power Jet Pro compressor. Due to the volatility of the solvent and particles during the spraying

process, all the experiments are conducted in a fume-hood. To compare spraying conditions, a standard size zone of 80 cm^2 is set.

7.2.3 Characterization

Atomic force microscopy is performed with NT-MDT in tapping mode. GO exfoliated by sonication is diluted to 0.1 $mg.mL^{-1}$ and then is sprayed onto a freshly cleaved mica sheet or onto coated glass slides. AFM is performed in tapping mode using a three-points head. Roughness is measured through Nova software.

Scanning electron microscopy is performed with a FEI Inspect-F microscope. Samples are observed at a working distance of 10 mm and at 5 kV. The samples are, prior to the observation, coated with a layer of gold.

Contact angle measurements are performed using three probe liquids, PEG, Glycerol, and Water. A 5 µm drop is deposited on the polymer. The angle measurement is obtained with a DSA 100 KRUSS apparatus and Drop Shape Analysis software. The contact angle of each liquid is based on an average of three drop measurement.

7.2.4 Deposition of a PVA layer by spray coating

The surface topography of the PVA layer is first studied. The layer deposited is expected to be thin, uniform, homogeneous and smooth. The surface topography of the polymeric layer plays a major role in the final nanocomposites. For example, Kotov et al. [15] have presented a LbL nanocomposite, based on polyelectrolyte-rGO- where the electrical conductivity is affected by the roughness of the substrate. A decrease of the conductivity from 10^4 to 10^7 $\Omega^{-1}.m^{-1}$ is observed for the LbL sample with the rougher polymeric layers. This is believed to be due to a less

uniform self-assembly process in these materials, which lead to disrupted layers and a less uniform in-plane contact between rGO.

7.2.4.1 Effect of the sacrificial layer

Since LbL nanocomposites are based on a bottom-up approach, the nanocomposite is built up on top of a wafer. In order to get a free-standing nanocomposite several methods have been studied to peel the nanocomposite film without damaging it. Direct peeling [16] or etching the wafer [17] are some methods to obtain free standing films. The use of a sacrificial layer is the most common method [18, 19] as it can be adapted to any substrate and any film.

A sacrificial layer is a layer deposited on a solid substrate. This layer, usually very thin, can be obtained by traditional deposition method, i.e. spin-coating, dip-coating, etc. Next the desired layers are built-up on this pre-deposited layer. When the desired film is thick enough, the film is immersed in a solution which dissolves the pre-deposited layer but does not affect the desired film. After dissolution of the sacrificial layer, the desired film is detached from the substrate.

The choice of the sacrificial layer is based on several criteria which are i) a good interaction with the matrix, in our case PVA layer, ii) can be dissolved in a solution which does not interact with our PVA-GO nanocomposite, and iii) a low toxicity of the solvents to be used.

In order to study the effect of the sacrificial layer on the morphology of the first PVA layer two common polymers, i.e. PMMA and PS, are studied. Both polymers are spin-coated, to form a thin layer. Following this a layer of PVA is sprayed and studied by electron microscopy as presented in Figure 7.1.

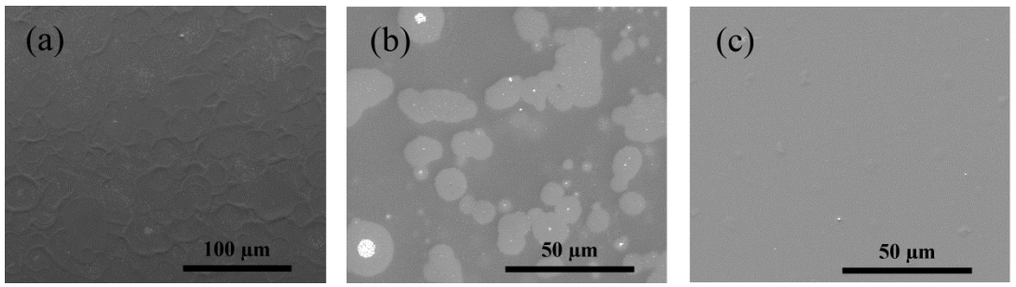

Figure 7.1: SEM microscopy of sprayed PVA layer deposited onto different sacrificial layers; a) PMMA, b) PS and c) PS with O_2 plasma treatment.

The surface topography from SEM shows that deposited on PMMA, Figure 7.1 a, the PVA layer is not homogeneous. The PVA layers exhibit wide craters. On the other hand, PVA deposited on PS shows even less uniform coatings with uncoated islands, Figure 7.1 b. Here, PVA has clearly not fully coated the sacrificial layer due to dewetting of the hydrophilic PVA on top of the hydrophobic PS. When the PVA layer is sprayed, the water droplets tend to minimise the surface area in contact with the PS. It is worth to note, however, that the PVA deposited does seem to have a smooth surface. To increase the hydrophilic behaviour of the PS layer, a corona treatment is applied on the PS surface [20, 21]. Figure 7.1 c shows the surface topography of the PVA layer after treatment of the PS layer. No islands are observed, which indicates good wetting of PVA on the O_2 treated-PS layer. Since we obtained a good wetting of the PVA and the surface is relatively smooth, further substrates are coated with PS, and are all treated with corona prior to the spraying experiments.

7.2.4.2 Effect of spraying pressure

To understand the effect of the pressure on the sprayed PVA layer, PVA layer are sprayed at a constant nozzle to substrate distance, but at different pressures. Figure

7.2 shows AFM pictures in height mode of PVA layers sprayed at low, medium and high pressure, respectively.

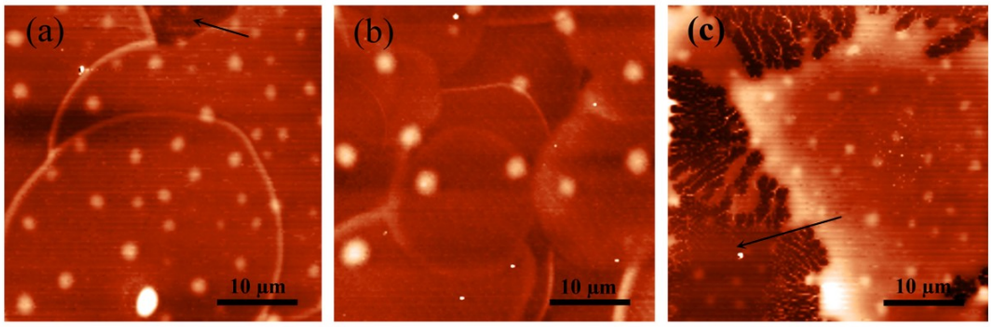

Figure 7.2: AFM images representing the surface topography of PVA layer sprayed at different pressures; (a) P = 1 bar, (b) P = 1.4 bar, (c) P = 2.8 bar. The black arrows show the sacrificial layered uncovered by the PVA and the white dots on the pictures are due to the plasma treatment on PS.

Low air pressure (Figure 7.2 a) results in sputtering rather than atomisation of PVA solution. The density of the spraying is low and consisted of big droplets. When these few big droplets are sprayed, they have lesser chance to be close to each other and to coalesce. As another large droplet is deposited, the previous droplet has already dried, and cannot coalesce together. This results in a non-uniform film with lots of uncovered areas. Upon increasing pressure (Figure 7.2 b), the density of the spraying increases and consists of smaller droplets, leading to a more uniform film. These small droplets have a higher chance to coalesce before drying. If the pressure is further increased (Figure 7.2 c), the PVA solution is blown away by the airflow, which again leads to a non-uniform layer of PVA.

7.2.4.3 Effect nozzle to substrate distance

To understand the effect of the distance between the nozzle and the substrate on the sprayed PVA layer, PVA layers are sprayed at different nozzle-substrate distances. Figure 7.3 shows AFM topography of PVA layers sprayed at a distance of 15, 20 and 25 cm, respectively.

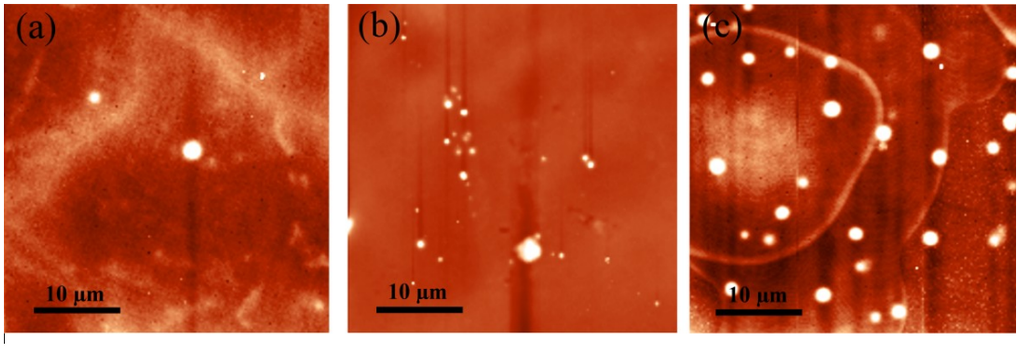

Figure 7.3: AFM height image of PVA layer sprayed at different nozzle-substrate distances; a) 15 cm, b) 20 cm and c) 25 cm.

When the distance between the nozzle and the substrate is small, like in Figure 7.3 a, a layer of PVA is deposited. However, this deposited layer is very wet and instable with a high chance of runs and sags as a result of gravity. As the distance increases (Figure 7.3 b) the solution droplets deposited are dryer creating a more homogeneous PVA layer since they are wet enough to coalesce with others. If the distance is further increased (Figure 7.3 c) the PVA droplets dry or partially dry before reaching the substrate surface, resulting in a non-homogeneous layer of PVA of drops which do not merge.

7.2.4.4 Thickness of the PVA layer

In order to determine how much solution is needed to cover a certain area, we studied the surface of the PVA layer with AFM as presented in Figure 7.4 (a; b).

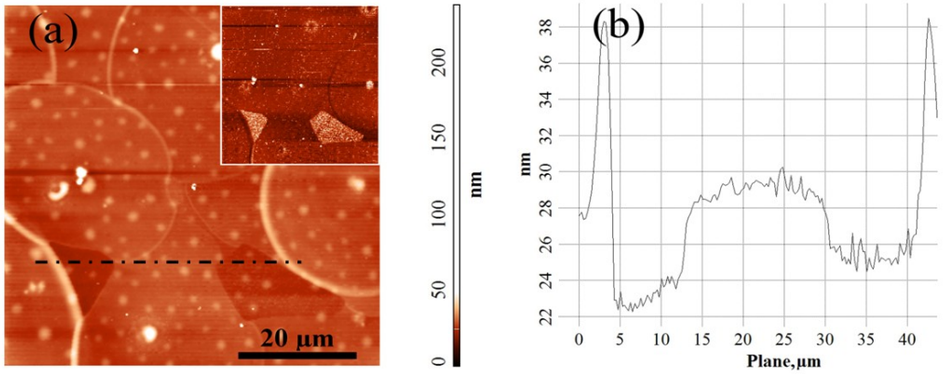

Figure 7.4: a) Surface of PVA layer from AFM microscopy; the inset picture shows the phase image of the same area, b) Surface topography along the dashed line in picture a).

The surface of the PVA is observed by AFM (Figure 7.4 a), showing PVA droplets randomly deposited onto the sacrificial layer. The two darker zones represent the sacrificial layer, i.e. the O_2 treated PS. These zones are highlighted in the inset picture, showing the phase contrast image of the same area; the sacrificial layer having the lighter colour. The thickness of a PVA droplet is calculated from the surface topography along the dashed line (Figure 7.4 a) and plotted in Figure 7.4 b). The thickness of PVA droplets are measured at around 6 nm.

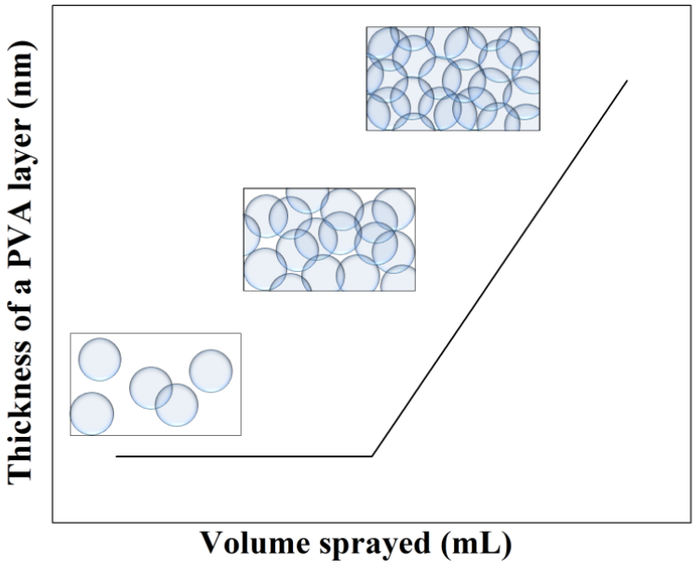

Figure 7.5: Schematic model of the morphology of the sprayed PVA layer in function of the volume of solution sprayed. The rectangles represent the surface of the sprayed PVA layer, whereas the white zone shows the sacrificial layer with the blue PVA droplets sprayed on top of it.

The spraying of PVA solution behaves like a percolated system as shown in Figure 7.5. During spraying, the PVA droplets are sprayed randomly onto the surface. At the beginning the droplets are spread randomly over the surface and are not connected. As the volume of solution sprayed increases, the droplets start to merge together to form a continuous layer. The thickness of the layer increases with the sprayed volume.

In order to estimate the volume of solution necessary to fully cover a surface, layer thicknesses are measured by AFM and plotted in Figure 7.6.

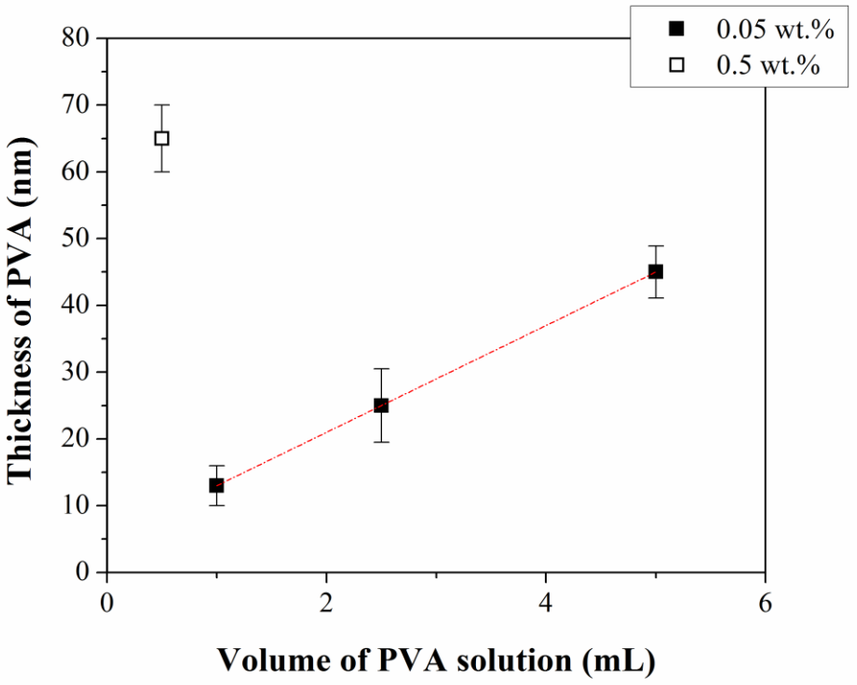

Figure 7.6: Thickness of the PVA layer in function of the volume of aqueous PVA solution sprayed at a concentration of (■) 0.05 wt. % and (□) 0.5 wt. %.

Figure 7.6 shows the thickness of the PVA layer in function of the volume of PVA solution sprayed where the black squares represents an aqueous solution of PVA at 0.05 wt. % concentration and the hollow squares a solution at 0.5 wt. %. For the lower concentration, the thickness of the PVA layer increases as the volume increases. Spraying a volume of 1 mL creates a polymer layer of 13 nm. This corresponds to a bi-layer of PVA if we assume that polymer droplets are around 6 nm thick.

In order to study the effects of polymer concentration on the layer thickness, we compared the previous PVA solution (black squares) with a solution of higher concentration (hollow squares). As observed the solution at 0.5 wt. % leads to a

much thicker PVA layer. For example, after spraying 0.5 mL, the thickness of this layer reaches 65 nm.

In short it is concluded that two parameters are important to produce thin layers with a controlled thickness. The first one is the concentration of the solution. Solution concentration is an efficient parameter to control roughly the polymer thickness, allowing very thick or very thin layers. The volume sprayed on the other hand is a parameter which allows for a better control of the polymer layer thickness and allows for the adjustment of the thickness.

7.2.5 Deposition of GO by spray-coating

Similar to the polymer layer, the surface topography of the GO layer is studied when deposited by spray-coating. The layer deposited is expected to be a mono-layer or bi-layer, and homogeneous. In order to spray such a mono- or a bi-layer of graphene, the dispersion of GO in various solvents and the volume sprayed is studied.

7.2.5.1 Effect of solvent

The physical properties of solvents are important in the quality of the spraying. The solution sprayed needs to dry quickly in order to create a homogeneous layer. Spraying a nanoparticles solution with a high volatility allows to the particles to be deposited dry onto the surface. Conversely, if the volatility of the solvent is too low, the droplets do not dry immediately and are pushed away from the surface, resulting in a non-uniform deposition [12]. On the other hand, to obtain mono or bi-layers of GO, the quality of the GO dispersion is crucial [22]. Table 1 shows the physical properties of water and ethanol which are used as a solvent.

Table 7.1: Physical properties of solvents from [23].

	Vapour pressure at 21 C ***(mmHg)***	**Boiling Point** ***(°C)***	**Evaporation rate** ***(Ether=1)***
Water	19	100	-
Ethanol	45.7	78	8.3

Due to the high evaporation rate and the low toxicity, ethanol is studied first. GO is sonicated either in water, ethanol or a mixture of both. Figure 7.7 shows the dispersion of GO in various solvents immediately after sonication (1) and after one day sedimentation (2).

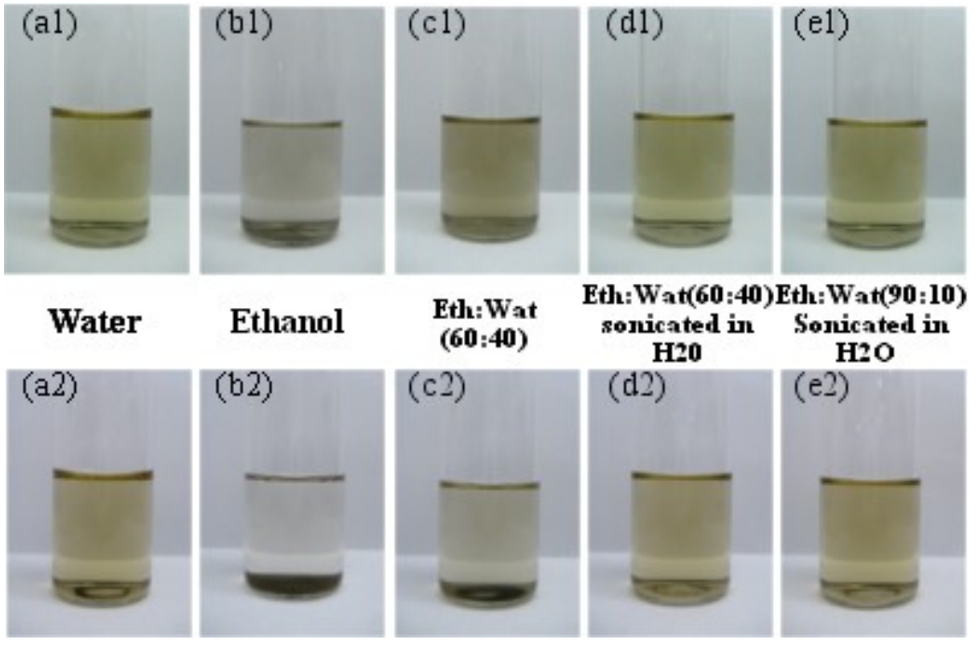

Figure 7.7: Dispersion of GO in various solvents: (1) represents the solution immediately after sonication and (2) represents the solution after one day sedimentation. a) aqueous solution of GO; b) GO in ethanol; c) a GO in a solution of

ethanol:water (60:40); d) GO in a solution of ethanol:water (60:40) where the GO is sonicated in water only; e) GO in a solution of ethanol:water (90:10) where the GO is sonicated in water only.

As previously reported by Parades et al. [24] and as observed in Figure 7.7 a1 the dispersion of GO in water is good. After one day, Figure 7.7 a2, the dispersion of GO is still stable, however some GO agglomerates have sedimentated forming a ring at the bottom of the bottle. Ethanol is studied as it has a higher volatility than water. When GO is sonicated in pure ethanol, Figure 7.7 b1, the dispersion is unstable and GO particles sedimentate quickly. After one day, Figure 7.7 b2, the GO particles have completely sedimented and are at the bottom of the bottle. A mixture of both solvents is then studied. When a solution of GO in an ethanol: water (60: 40) mixture is sonicated, Figure 7.7 c1, the dispersion is found unstable. After a few hours, GO particles start to agglomerate and finally sedimentate after one day, Figure 7.7 c2. On the other hand, when GO is first sonicated in water with the ethanol added later in the same proportion, Figure 7.7 d1, the GO solution remains stable even for months, Figure 7.7 d2. By adding the ethanol after sonicating GO in water, we get a stable solution even in an ethanol: water (90:10) mixture (Figure 7.7 e1 and e2).

The AFM pictures show the deposition of GO particles in various solvents and are presented in Figure 7.8.

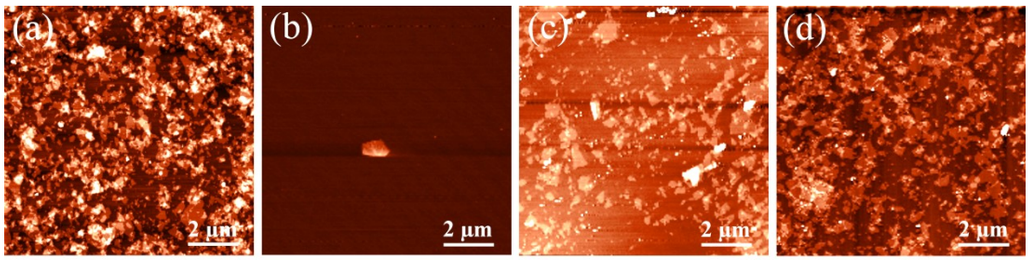

Figure 7.8: AFM of GO deposited on mica after one day sedimentation from a) aqueous solution of GO, b) GO in ethanol, c) GO in ethanol:water (60:40) mixture and d) GO in ethanol:water (60:40) mixture where the GO is sonicated in water only.

As previously discussed, the deposition of GO from an aqueous solution is very good. The deposited monolayer of GO is homogeneous and covers the whole surface, as seen in Figure 7.8 a. On the other hand, spraying GO from an ethanol solution shows no deposition of GO (Figure 7.8 b). The mica surface is clean with only a few big agglomerates showing. Since GO flakes are unstable in ethanol, GO mainly sedimentated at the bottom and only very few GO agglomerates are deposited.

The ethanol: water (60: 40) mixture sonicated together (Figure 7.8 c) presents an inhomogeneous deposition of GO together with agglomerates. In addition, the area covered by GO is reduced compared to the one obtained from an aqueous solution. On the other hand, in the ethanol:water (60: 40) mixture with the GO sonicated in water (Figure 7.8 d) the deposition is similar to the one obtain in water. The deposition consists of a monolayer of GO, which is homogeneous and covers the whole substrate.

From AFM microscopy, we can observe that the quality of the layer of sprayed GO is very dependent of the initial dispersion of the GO in the solution. A well dispersed

GO solution leads to a uniform deposition of mono-layers, and inversely a badly dispersed GO solution leads to the non-uniform deposition of a few thick flakes.

7.2.5.2 Deposition of a layer of GO by spraying method

The volume of GO solution necessary to estimate the covering rate and thickness of a deposited layer of GO is examined. Figure 7.9 shows the surface covered by a layer of GO for different volumes of solution sprayed.

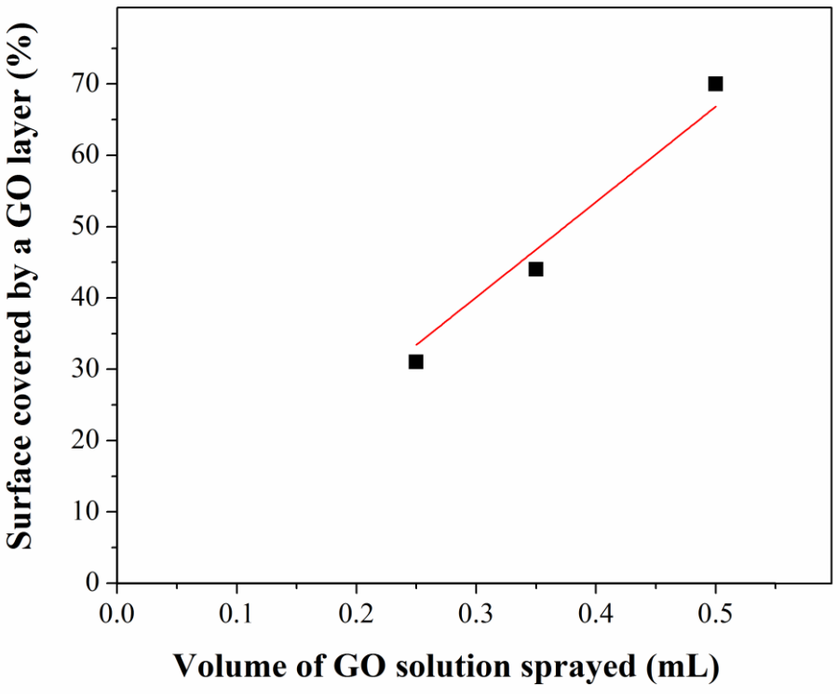

Figure 7.9: Evolution of surface cover by GO in function of the GO solution volume sprayed at 1 mg.mL^{-1}. The red line is a linear fitting intercepting at 0.

As expected the surface covered by GO increases as the volume sprayed increases (Figure 7.9). For example, 0.35 mL of GO solution sprayed covers more than 40 % of the surface, while 0.5 mL covers up to 70 %. To understand the morphology of

the GO layer sprayed, the thickness of the GO layer is also investigated in relation to the volume sprayed (Figure 7.10).

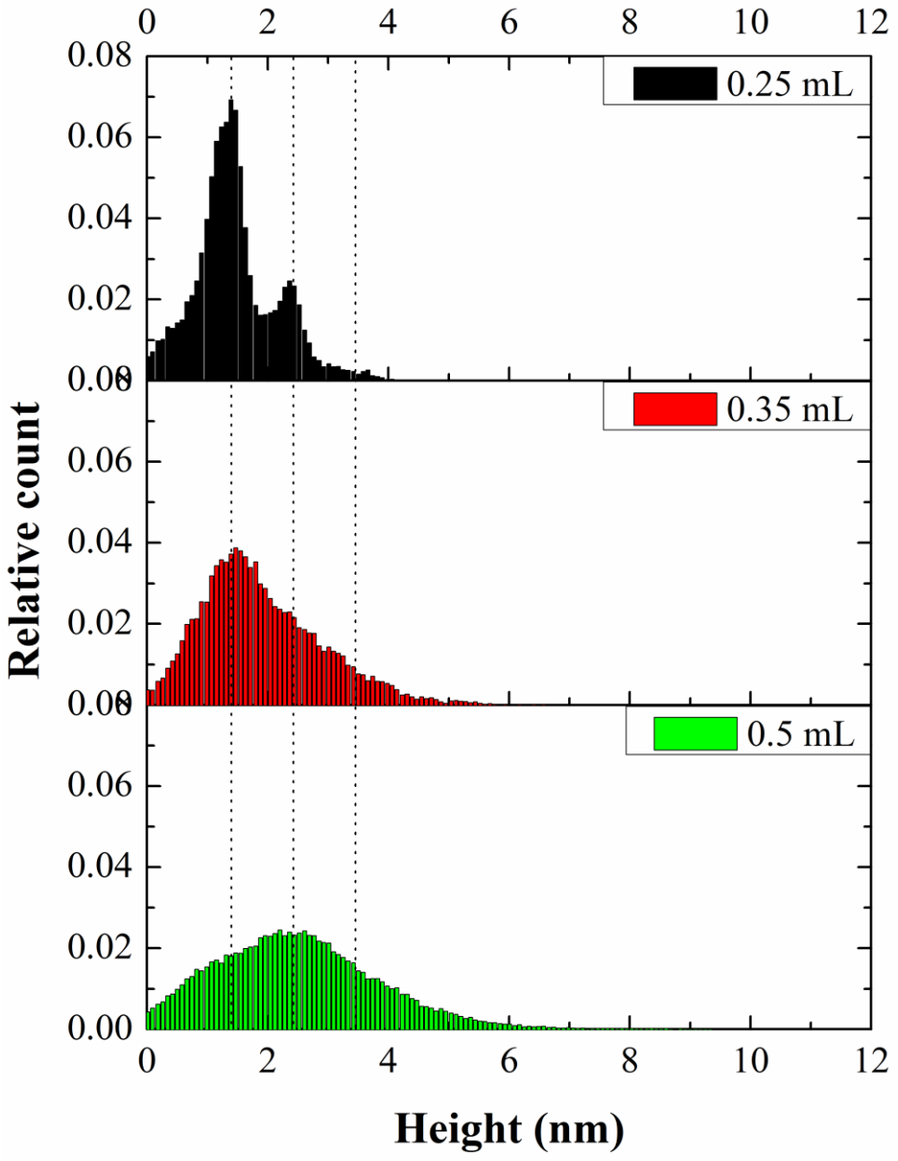

Figure 7.10: Histogram representing the thickness of the GO layer for 0.25, 0.35 mL and 0.5 mL of GO solution sprayed. The dotted lines at 1.4, 2.4 and 3.4 nm represent the thickness of a mono-layer, bi-layer and tri-layer.

At 0.25 mL of GO sprayed, i.e. 31 % of surface covered, the GO layer is mainly composed of mono-layer and few bi-layers. On the other hand at 0.35 mL, i.e. 44 % of surface covered, the surface is covered by mono-layer and bi-layers but also few tri-layers. And finally at 0.5 mL, i.e. 70 % of surface covered, the layer is mainly composed of bi-layers, followed by mono-layers and tri-layers.

7.2.6 Deposition of GO on a polymeric layer

The deposition of GO is studied for two different polymer layers. Graphene like graphene oxide, due to its dimensionality, atomic thickness and high aspect ratio, are very flexible sheets [25]. Because of this one of the drawbacks is that these sheet are very sensitive to their environment [26]. The interaction of sprayed GO with its environment is studied by spraying a GO solution onto mica, the reference, a PMMA layer and a PVA layer. PMMA and PVA are chosen based on their polarity and their ability to form a very smooth surface. To prevent an effect of polymer surface topology on the GO [27, 28], the roughness is checked by AFM, and is around 0.2 nm, 0.7 nm and 1 nm, respectively for mica, PMMA and PVA.

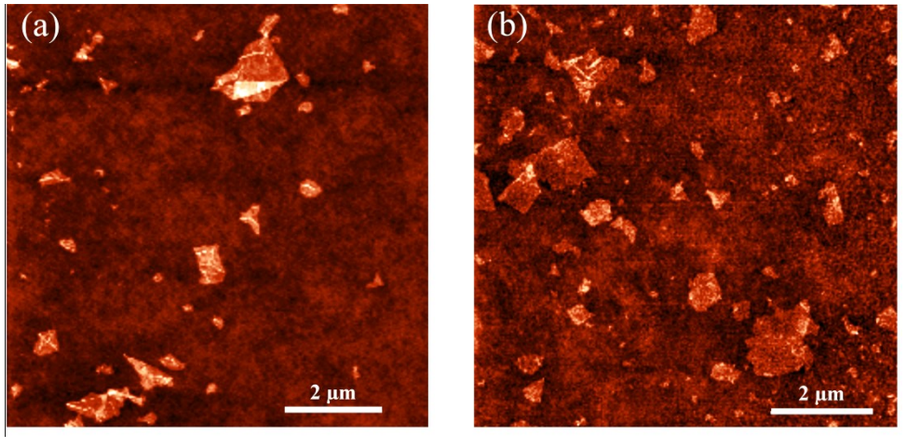

Figure 7.11: GO sprayed and deposited on a) PMMA and b) PVA layer.

Figure 7.11 shows the deposition of GO on PMMA and PVA layers. Figure 7.11 aand b clearly show that either on PMMA and PVA, the GO flakes are well distributed and deposited flat on both polymeric layers. The noticeable difference between both pictures is that on PMMA, the morphology of the GO platelets contains many more defects than on PVA. These defects consist usually of major wrinkles but also less frequently in folded platelets.

Figure 7.12, shows some representative images of damaged GO sheets deposited on PMMA. Usually, and especially for small aspect ratio platelets defects consist of the formation of major wrinkles, as seen in Figure 7.12 a. These wrinkles are not the *intrinsic ripples* as often discussed for graphene platelets [29], as the height of those wrinkles is usually between the nanometre up to 5 nm with widths between 20 to 100 nm. Similar wrinkles have been previously reported on deposited GO platelets [30, 31]. For instance, Cote et al. [30] observed that under compression, GO morphology in aqueous solution evolves from flat to wrinkled by changing the pH of the solution; i.e. changing the hydrophilicity and the wettability of GO. In basic solution, GO is more hydrophilic, and under compression no wrinkles are observed. GO tend to overlap. In contrary, in acidic solution, GO are less hydrophobic and under compression GO are squeezed resulting in the formation of wrinkles of more than 3 nm high.

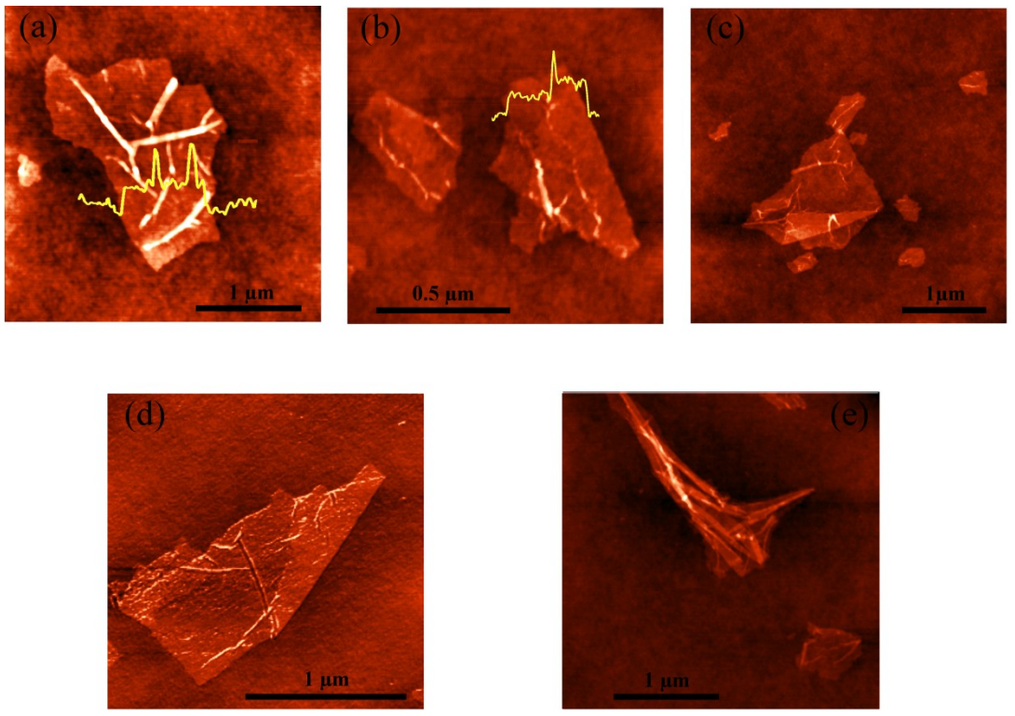

Figure 7.12: Defects observed in GO sheets deposited on PMMA including; (a) wrinkled flake, (b) flake folded in two, (c) and (d) folded and wrinkled flakes, (e) "multiple fold in zigzag" flake.

The second type of defect observed is folding of the GO sheet as observed in Figure 7.12 b, c and d. In addition, these folded structures are usually wrinkled. GO sheets folded in two, are observed in Figure 7.12 b which reduces by half their aspect ratio in one direction. The GO sheet can also contain multiple folds, as in Figure 7.12 c where the GO is triple folded. In single layer and bi-layer graphene sheet, it has been observed that this folding occurs along the symmetry axes, i.e. 30, 60, 90 and 120° which is along the [100] and [210] axes [32-34]. Similar observations are made for GO by Pandey et al. [31]. They observed that GO folds along the same symmetry axes than graphene sheet. In addition their observation suggests that the stress developed in such folds may eventually lead to cracks. The most damaged configuration observed in this study is shown in Figure 7.12 e. It shows a micron-

sized GO sheet, with a heavily folded configuration. The folds occur mainly perpendicular to the longer side of GO however some folds are also observed along to the longer side. This highlights the fact that in order to unfold the GO, the sheets have to be stretched in two directions. Interestingly, despite the many different folding configurations observed, a 3D crumpled ball-like particle [35] is not observed.

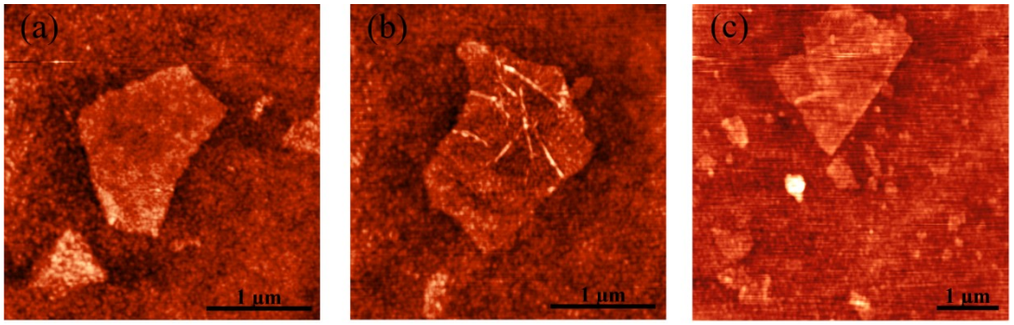

Figure 7.13: Defects observed in GO sheets on PVA surface; (a) light folded GO, (b) wrinkled GO and (c) GO folded in two.

Representative defects in the GO configuration when deposited on PVA are also observed, and presented in Figure 7.13. Similar defects are also observed in high aspect ratio GO sprayed on PVA, however, these defects are usually less predominant. For instance, Figure 7.13 a shows a folded GO, while a GO sheet folded in two is observed in Figure 7.13 c. Although, no multiple folds are observed, as seen in Figure 7.12 e, wrinkles are observed of 60 nm in length and up to 5 nm in height (Figure 7.13 b). These wrinkles are consistent with those observed on PMMA.

To further appreciate the difference between in GO morphology sprayed on PVA and PMMA a statistical analysis was performed and is shown in Figure 7.14 a and b. The histograms present the percentage of GO containing defects when they are

deposited on either PMMA or PVA layers based on more than 100 GO platelets. In this case, any changes in the 2D conformation, either major wrinkles, folds or crumples are considered as defects. The percentage of defects on GO morphology is also studied in function of the initial length of the GO, i.e. for a folded flake the length is recalculated taking in account the folded part.

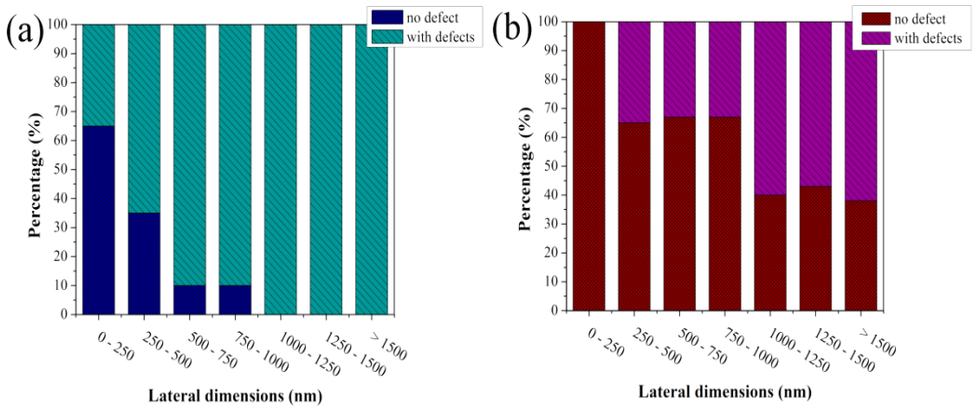

Figure 7.14: Histogram representing the proportion of GO sprayed on (a) PMMA and (b) PVA, representing the number of GO sheets with and without defects based on more than 100 GO sheets.

For both PMMA and PVA, defects in the GO sheet morphology are observed. As the GO aspect ratio increases, the proportion of GO with a defective morphology increases. For GO deposited on PMMA, defects are observed even for very small platelets below 250 nm. All platelets larger than one micron show defects when deposited on PMMA. In contrast, small GO flakes deposited on PVA are defect free, although also here the number of defect platelets increases with aspect ratio. However, for GO on PVA some micron-sized platelets are undamaged.

The results highlight that the larger the sheets, the more prompt they are to show defects. This trend may result from the high flexibility of GO sheets. There is also a

distinctive difference in the distribution of the population of flakes with wrinkles and folds between both substrates. As all samples were sprayed in the same conditions we presume the deposition process is not the driving force for these changes in morphology. As previously discussed by Putz et al. [35], PVA has stronger interactions with GO than with PMMA due to the strong H-bonding. Rather than the processing [33, 36, 37], we consider the surface energy of the polymer films to influence on the morphology of sprayed GO.

To illustrate this, contact angle measurements were performed using three probe liquids and the surface free energy was determined by the Owens-Wendt theory as reported here [38, 39]. The data are summarised in Table 7.2: Surface Tension Data for the Three Probe Liquids, with the total surface tension, γ_1, the dispersive component, γ_1^d , and the polar component, γ_1^p and obtained from [40]. Θ, correspond to the contact angle measured for each liquids on PMMA and PVA.Table 7.2.

Table 7.2: Surface Tension Data for the Three Probe Liquids, with the total surface tension, γ_1, the dispersive component, γ_1^d , and the polar component, γ_1^p and obtained from [40]. Θ, correspond to the contact angle measured for each liquids on PMMA and PVA.

	γ_1 *(mJ.m^{-2})*	γ_1^d *(mJ.m^{-2})*	γ_1^p *(mJ.m^{-2})*	**Θ *(deg)***	
				PMMA	**PVA**
PEG	48.3	29.4	19.0	31.6 ± 3.0	35.5 ± 3.7
Glycerol	64.0	34.0	30.0	64.4 ± 1.1	52.9 ± 1.1
Water	72.8	21.8	51.0	67.4 ± 2.4	58.9 ± 2.3

As detailed in Table 7.3, it is found that the surface free energy is slightly higher in the case of the PVA substrate, i.e. 31.7 $mJ.m^{-2}$ for PMMA and 43.7 $mJ.m^{-2}$ for PVA. More interestingly, there is a large difference in the polar contribution (γ_l^p) for these films.

Table 7.3: Surface free energy γ_l of PVA and PMMA spin coated films with dispersive γ_l^d and polar γ_l^p contributions determined from the Owens-Wendt plot.

	γ_l^p ***(mJ.m^{-2})***	γ_l^d ***(mJ.m^{-2})***	γ_l ***(mJ.m^{-2})***
PVA	32.3 ± 0.1	11.4 ± 0.4	43.7 ± 0.6
PMMA	17.2 ± 2.0	14.5 ± 1.6	31.7 ± 0.8

The higher polarity of the PVA surface might be the reason for observing less damaged conformations of sprayed GO sheets. Similar findings were also reported in the literature where a change in configuration of suspended GO membranes from crumpled to compact structure is previously demonstrated in aqueous solution by adding acetone molecules. The change of conformation is attributed to the addition of less polar molecules as well as the lower affinity between the membrane and the medium [41]. Similar observations were obtained with suspended GO in aqueous solution and in nanocomposites, where GO conformation evolves from extended to aggregate as the affinity between GO and the dispersion medium or polymer matrix decreases [42].

7.3. Conclusions

The spraying conditions of graphene oxide monolayers are studied for two different cases. Firstly, the spraying deposition of a polymeric layer is studied. In this case, the aim is to deposit a thin, uniform and homogeneous layer of PVA. Spraying polymeric layers consists of deposition of polymer droplets which coalesce to form a uniform layer. Parameters like pressure, nozzle to substrate distance but also the chemical nature of a sacrificial layer are studied. It is found that they all play a major role in the quality of the spraying but that they can also counterbalance each other. For example, spraying at high pressure blows away the solution from the surface due to the strong airflow. However this effect is reduced if the distance between the nozzle and the substrate is large. The volume as well as the concentration of the solution is also studied in order to estimate the lowest possible thickness of sprayed PVA layer. Lower concentrations at constant volume lead to thinner layer, while the volume of solution sprayed allows for some fine-tuning of the deposited thickness.

Spraying conditions are also studied for the deposition of homogeneous mono-layers of GO. For the spraying of GO the nanoparticles needs to be dry prior to deposition. For this, first the dispersion of GO in different solvents is studied. Well dispersed GO in solution is essential to obtain GO monolayers as poor dispersion will lead to the deposition of GO aggregates. The spraying volume is also investigated, showing an increase in deposited GO with increasing volume of solution sprayed.

In addition, defects on the GO configuration are observed when they are deposited on PMMA and PVA substrates. These defects include large wrinkles and/or folds. It is observed that for both PVA and PMMA, the proportion of GO with a defective morphology increases as the GO aspect ratio increases. However, it is much more

pronounced in the case of PMMA, which have a lower polar contribution. Based on these results, it seems that the GO morphology is strongly affected by the polymer chemistry. Finally, we have shown that spraying is a very versatile process to deposit thin layers of polymer and graphene oxide. The deposition of these layers can be finely tuned by adjusting several parameters like spraying conditions (pressure, distance, volume, etc.), the nature of the solvent or the nature of the substrate.

7.4. References

1. L.-M. Chen, Z. Hong, W.L. Kwan, C.-H. Lu, Y.-F. Lai, B. Lei, C.-P. Liu, and Y. Yang, ACS Nano, 2010. **4**(8): p. 4744-4752.
2. C. Girotto, B.P. Rand, J. Genoe, and P. Heremans, Solar Energy Materials and Solar Cells, 2009. **93**(4): p. 454-458.
3. S.F. Tedde, J. Kern, T. Sterzl, J. Fu□rst, P. Lugli, and O. Hayden, Nano Letters, 2009. **9**(3): p. 980-983.
4. S. Bae, H. Kim, Y. Lee, X. Xu, J.-S. Park, Y. Zheng, J. Balakrishnan, T. Lei, H. Ri Kim, Y.I. Song, Y.-J. Kim, K.S. Kim, B. Ozyilmaz, J.-H. Ahn, B.H. Hong, and S. Iijima, Nat Nano, 2010. **5**(8): p. 574-578.
5. C. Sellam, Z. Zhai, H. Zahabi, H. Deng, E. Bilotti, and T. Peijs, MRS Online Proceedings Library, 2012. **1410**: p. null-null.
6. W. Hong, Y. Xu, G. Lu, C. Li, and G. Shi, Electrochemistry Communications, 2008. **10**(10): p. 1555-1558.
7. S.-C. Chang, J. Liu, J. Bharathan, Y. Yang, J. Onohara, and J. Kido, Advanced Materials, 1999. **11**(9): p. 734-737.
8. B.J. de Gans, P.C. Duineveld, and U.S. Schubert, Advanced Materials, 2004. **16**(3): p. 203-213.
9. J.W. Jung and W.H. Jo, Advanced Functional Materials, 2010. **20**(14): p. 2355-2363.
10. J. Zheng, A. He, J. Li, J. Xu, and C.C. Han, Polymer, 2006. **47**(20): p. 7095-7102.
11. V. Morozov, T. Morozova, and N. Kallenbach, International Journal of Mass Spectrometry, 1998. **178**(3): p. 143-159.
12. C.N. Hoth, R. Steim, P. Schilinsky, S.A. Choulis, S.F. Tedde, O. Hayden, and C.J. Brabec, Organic Electronics, 2009. **10**(4): p. 587-593.
13. A. O'Neill, U. Khan, P.N. Nirmalraj, J. Boland, and J.N. Coleman, The Journal of Physical Chemistry C, 2011. **115**(13): p. 5422-5428.
14. J. Larrieu, B. Held, H. Martinez, and Y. Tison, Surface and Coatings Technology, 2005. **200**(7): p. 2310-2316.
15. N.A. Kotov, I. Dékány, and J.H. Fendler, Advanced Materials, 1996. **8**(8): p. 637-641.
16. J.L. Lutkenhaus, K.D. Hrabak, K. McEnnis, and P.T. Hammond, Journal of the American Chemical Society, 2005. **127**(49): p. 17228-17234.
17. P. Podsiadlo, A.K. Kaushik, E.M. Arruda, A.M. Waas, B.S. Shim, J. Xu, H. Nandivada, B.G. Pumplin, J. Lahann, A. Ramamoorthy, and N.A. Kotov, Science, 2007. **318**(5847): p. 80-83.
18. S.S. Ono and G. Decher, Nano Letters, 2006. **6**(4): p. 592-598.
19. S.T. Dubas, T.R. Farhat, and J.B. Schlenoff, Journal of the American Chemical Society, 2001. **123**(22): p. 5368-5369.

20. S. Guruvenket, G.M. Rao, M. Komath, and A.M. Raichur, Applied Surface Science, 2004. **236**(1–4): p. 278-284.

21. Y. Chen, Q. Gao, H. Wan, J. Yi, Y. Wei, and P. Liu, Applied Surface Science, 2013. **265**(0): p. 452-457.

22. O.C. Compton and S.T. Nguyen, SMALL, 2010. **6**(6): p. 711-723.

23. I.M. Smallwood. Second ed. 2002: Blackwell Science.

24. J.I. Paredes, S. Villar-Rodil, A. Martínez-Alonso, and J.M.D. Tascón, Langmuir, 2008. **24**(19): p. 10560-10564.

25. R.F. Service, Science, 2009. **324**(5929): p. 875-877.

26. Q. Li, Z. Li, M. Chen, and Y. Fang, Nano Letters, 2009. **9**(5): p. 2129-2132.

27. U. Stoberl, U. Wurstbauer, W. Wegscheider, D. Weiss, and J. Eroms, Applied Physics Letters, 2008. **93**(5): p. -.

28. S. Scharfenberg, D.Z. Rocklin, C. Chialvo, R.L. Weaver, P.M. Goldbart, and N. Mason, Applied Physics Letters, 2011. **98**(9): p. 091908.

29. J.C. Meyer, A.K. Geim, M.I. Katsnelson, K.S. Novoselov, T.J. Booth, and S. Roth, Nature, 2007. **446**(7131): p. 60-63.

30. L.J. Cote, J. Kim, Z. Zhang, C. Sun, and J. Huang, Soft Matter, 2010. **6**(24): p. 6096-6101.

31. D.K. Pandey, T.F. Chung, G. Prakash, R. Piner, Y.P. Chen, and R. Reifenberger, Surface Science, 2011. **605**(17–18): p. 1669-1675.

32. H.-V. Roy, C. Kallinger, B. Marsen, and K. Sattler, Journal of Applied Physics, 1998. **83**(9): p. 4695-4699.

33. H.V. Roy, C. Kallinger, and K. Sattler, Surface Science, 1998. **407**(1–3): p. 1-6.

34. L. Li, R.P. Liu, Z.W. Chen, Q. Wang, M.Z. Ma, Q. Jing, G. Li, and Y. Tian, Carbon, 2006. **44**(8): p. 1544-1547.

35. J. Luo, H.D. Jang, T. Sun, L. Xiao, Z. He, A.P. Katsoulidis, M.G. Kanatzidis, J.M. Gibson, and J. Huang, ACS Nano, 2011. **5**(11): p. 8943-8949.

36. Z.J. Li, Z.G. Cheng, R. Wang, Q. Li, and Y. Fang, Nano Letters, 2009. **9**(10): p. 3599-3602.

37. G. Tsoukleri, J. Parthenios, K. Papagelis, R. Jalil, A.C. Ferrari, A.K. Geim, K.S. Novoselov, and C. Galiotis, SMALL, 2009. **5**(21): p. 2397-2402

38. U. Stachewicz, S. Li, E. Bilotti, and A.H. Barber, Applied Physics Letters, 2012. **100**(9): p. -.

39. U. Stachewicz and A.H. Barber, Langmuir, 2011. **27**(6): p. 3024-3029.

40. B. Jańczuk, T. Białopiotrowicz, and A. Zdziennicka, Journal of Colloid and Interface Science, 1999. **211**(1): p. 96-103.

41. X. Wen, C.W. Garland, T. Hwa, M. Kardar, E. Kokufuta, Y. Li, M. Orkisz, and T. Tanaka, Nature, 1992. **355**(6359): p. 426-428.

42. M. Hirata, T. Gotou, S. Horiuchi, M. Fujiwara, and M. Ohba, Carbon, 2004. **42**(14): p. 2929-2937.

Chapter 8

Bio-inspired PVA-GO nanocomposites by layer by layer spraying

8.1. Introduction

Bio-composites such as bones, teeth, or nacre are composed of mineral particles and a protein matrix with superior strength and toughness. For example, nacre which is composed of 95% of mineral particles is 3000 times tougher than the mineral particle it is based on. Common features in bio-composites are their complex architectures with several orders of hierarchical structure, different hierarchical structures at different length scales, arrangements and orientations, a very high volume fraction of high aspect ratio particles and the smallest building blocks often being at the nanoscale [1]. In contrast traditional man-made nanocomposites, like melt-mixing, solution casting or in-situ polymerization, have a relatively low efficiency and a low potential of reinforcement of the nanoparticles mainly because of the difficulty to

create highly loaded nanocomposites, which display homogeneous dispersion of the nanoparticles, good adhesion between the particles and the matrix, and with highly oriented particles within the matrix [2].

According to mechanical predictions based on the rule of mixture or Halpin-Tsai's model, increasing the volume fraction would allow getting very high reinforced nanocomposites. However, traditional nanocomposites usually exhibit very low loading [3-5], as low volume fraction of nanoparticles leads to a better dispersion in the matrix, and thus a better reinforcing efficiency in the nanocomposite. In addition, the volume fraction is limited by 3 mains factors, (i) the increase of the viscosity as the loading increase [6], (ii) a lower degree of dispersion as the loading increases, and finally (iii) the decrease of maximum packing for high aspect ratio particles considering a random polymer coil [7].

Another parameter to get effectively reinforced nanocomposites is through their aspect ratio. Indeed, according to Halpin-Tsai model [8], an increase in aspect ratio leads to an increase of the nanocomposite reinforcement. However, by comparing two graphite nanoplatelets (GNP) of 1 μm and 15 μm width, GNP with lower aspect ratio exhibited a better reinforcement [9, 10]. This behaviour is described as a drawback of the high flexibility of high aspect ratio GNP. As the aspect ratio of the GNP increase, the particles becomes more flexible and thus more sensitive to the polymer motion, which leads to irremediable scrolling or buckling of the particles.

Processing of nanocomposites is probably one of the key to overcome these drawbacks. For example, Wang et al. [11] showed that solution cast PVA-SWNT drawn into tapes achieved a very high mechanical reinforcement. The drawing process allowed the SWNT to align in the matrix. The addition of 0.1 wt.% led to an

increase of 200 % of the tensile strength and correspond to a contribution of the SWNT in the nanocomposite strength equivalent to 88 GPa. Recently, highly organized nanocomposites are highlight due to ability to high control of the structure of the nanocomposites [12]. Highly organized man-made nanocomposites have been mainly obtained by the layer-by-layer approach. This process is a bottom-up approach leading to a highly hierarchical structured nanocomposite. The most well-known process used is dip coating which consists of dipping repeatedly a substrate into three solutions (polymer, filler, and aqueous media) [13-15]. Another method of highly oriented and high volume fraction nanocomposites is obtained by vacuum filtration to form paper-like nanocomposites [16, 17]. A PVA-GO nanocomposites at 80 % loading is obtained by simple and traditional solution cast method, and presents a layer by layer structure [18]. Recently, a novel approach has been developed by Deville et al. [19] based on cast freeze-dried nanocomposites which also leads to highly ordered 3D structures [20, 21].

Spraying is a recent, versatile and rapid method for multilayer assemblies. It is a bottom-up approach, which consists of alternatively spraying two solutions (polymer and filler) on various substrates. The main advantage of spraying, besides being a simple method, is the ability to grow layers on large areas or objects with complex shapes like fibres [22].

Two dimensional particles such as graphene or graphene oxide are very attractive and promising nanofillers for multifunctional nanocomposites and can out-perform 1D fillers like carbon nanotubes. For mechanical properties, 2D particles have specific advantages over 1D particles because of the larger surface area in contact with the polymer matrix. The ability of GO to disperse in aqueous solution as well as

its ability to form H-bonding with polar polymers makes it a great candidate for spraying layer-by-layer nanocomposites.

In this study, we present a systematic comparison between a traditional solution cast nanocomposite and a layered nanocomposites obtained by sequential deposition of PVA and GO in solution. A uniform thin film consisting of 150 bi-layers is rapidly obtained over a large area, forming an LbL nanocomposite. Each layer is characterized by AFM. The uniform growth is monitored with UV-Vis spectrometer. The dispersion, optical, thermal and mechanical properties of both nanocomposites are investigated and addressed in function of the GO orientation.

8.2. Experimental

8.2.1 Materials

Poly(vinyl alcohol) (Mw ~ 85,000-124,000 $g.mol^{-1}$, 98-99 % hydrolyzed) and 5 vol.% glutaraldehyde solution in water (GA) are purchased from Sigma Aldrich. The graphene oxide is obtained by Hummer's method [23]. Polystyrene (Empera 124N) is obtained from Ineos.

8.2.2 Preparation

Solution preparation

PVA is dissolved in deionised water at 90^{o}C under continuous stirring for 4 hrs to produce two solutions with concentrations of 0.05 wt.% and 10 wt.%. A 5 wt.% PS solution is prepared in toluene at 90^{o}C under continuous stirring for 3 hrs. Graphene oxide suspension is obtained by dispersing the GO in deionised water at 1 $mg.mL^{-1}$

by a high-power ultra-sonication tip (1000 J). The suspension is left aside for 12 hrs to precipitate thicker aggregates.

Spray assisted LbL nanocomposite

Layer-by-layer nanocomposites are obtained by sequential deposition of PVA and GO in solution on a glass slide covered with a sacrificial layer via the spraying method. The nanocomposite film is prepared in 3 steps; the deposition of a sacrificial layer, the sequential layer deposition and the dissolution of the sacrificial layer to finally obtain a free standing film.

First, the GO suspension in DI water is further diluted in ethanol to give a final GO concentration of 0.01mg.mL^{-1} in water:ethanol with a 40:60 ratio. Glass slides are cleaned with isopropanol and dried with compressed air. A PS sacrificial layer is obtained by spin-coating PS solution at 2000 rpm for 1 min. The glass slides are then treated with an O_2 plasma for 4 min. The layer-by-layer PVA-GO nanocomposites are obtained by sequential deposition of PVA and GO in solution using an Iwata airbrush, see Figure 8.1. For the PVA layer, 0.1 g of PVA solution at 0.05 wt.% is used for spraying 56 cm^2. The airbrush spray gun is kept at 20 cm from the surface and the pressure is fixed at 18 psi. For the GO layer, 0.8 g of GO suspension at 0.01 wt.% is used to spray 56 cm^2. The spray gun is kept at 30 cm and the pressure is fixed at 25 psi. A pure PVA film is also produced using the same method. The sacrificial layer is subsequently dissolved by immersing the glass slides in toluene for 3 hrs at room temperature. The nanocomposite films are then peeled off from the glass slide, fixed on a metal frame and further washed in toluene for 24 hrs. The obtained free standing films are left to dry in air overnight and stored in a dessicator.

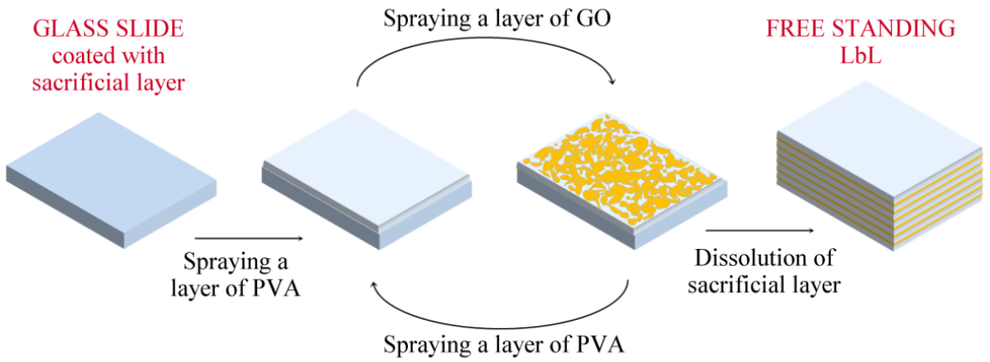

Figure 8.1: Spraying approach for layer-by-layer assembly where alternatively solutions of PVA/Di Water and GO/Di Water/Ethanol are sprayed on a glass slide coated with a PS sacrificial layer. The free-standing films are obtained by immersing the glass in toluene solution.

Solution cast nanocomposite

The GO dispersion (1 $mg.mL^{-1}$) is added to the PVA solution (10 wt.%) to produce a 5.4 wt.% solution. The solution is cast in a petri dish at room temperature and the solvent is evaporated over a week in ambient conditions. The obtained nanocomposite is peeled off and stored in a dessicator.

8.2.3 Characterization

Atomic Force Microscopy is performed using an NT-MDT in tapping mode. The analysis of particles is obtained with ImageJ software to measure the surface covered by GO.

Thermogravimetric analysis is performed with a TA Instrument Q500. The films are heated from room temperature to 800 °C at 10 $°C.min^{-1}$ under N_2 atmosphere.

Differential Scanning Calorimetry is performed by Mettler DSC 822e differential scanning calorimeter. 6 – 7 mg of material is used for each experiment. The method consists in two heating and two cooling. The two heating are from 20 °C to 235 °C at a heating rate of 10 °C.min^{-1} and the two cooling are from 235 °C to 20 °C at 30 °C.min^{-1}.

Morphological examinations are carried out using a FEI Inspector-F scanning electron microscope. Samples are observed at a working distance of 10 mm and at 10 kV. Prior to the SEM measurement, the sample are cross-linked with GA at 5 vol.% and then gold coated. To crosslink the PVA nanocomposites, the samples are dipped into the GA solution for 30 min, and then rinsed in de-ionized water. Then the samples are dried in air and then stored in dessicator.

Tensile tests are performed using an Instron 5586 at room temperature, equipped with a load cell of 2.5 N at a test speed of 10 % of the specimen length. Prior to the test, the films are fixed onto a cardboard frame as seen in Figure 8.2 a. The cardboard ensures a good parallelism between the film and the direction of the stretching and to protect the film to any stresses when the film is mounted on the equipment. Then the cardboard are cut and the films are stretched, showed in Figure 8.2 b.

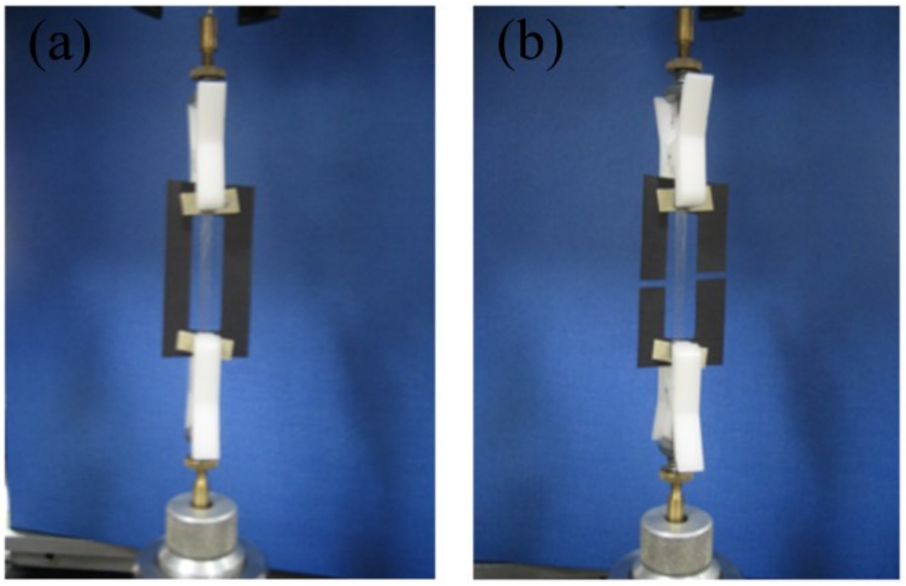

Figure 8.2: Tensile test of LbL nanocomposite films. (a) Before the test are the film is fixed on cardboard frame; (b) during the test, the cardboard frame is cut and the film is stretched.

8.3. Results and discussions

8.3.1 Characterization of the layer by layer process

The current LbL PVA-GO nanocomposites are made by a bottom-up approach where a nanometer-thick layer of GO and a layer of PVA are sequentially sprayed on a glass slide covered with a PS sacrificial layer.

Like in Chapter 5 and 6, the GO is obtained by Hummers's method [23] and is dispersed in DI water by ultrasound sonication. Ultrasound sonication is used to breaks down the aggregate and thus providing monolayers of graphene oxide with high aspect ratio. To avoid over-exposure of GO to ultrasound which would damages the sheets, UV-Vis spectroscopy is used to monitor the dispersion of the GO in DI

water as described in paragraph 5.3.1. A threshold in the UV-Vis peak is obtained after 1000 Joules. In order to fully exfoliate the particles and to get the highest aspect ratio, the solution of GO in DI water is sonicated for 1000 J only.

The supernatant is extracted and the aqueous solution of GO is diluted with a solution of DI water: ethanol to finally obtain an ethanol: DI water ratio of 60:40. The solution of GO in ethanol: DI water is stable even after several months.

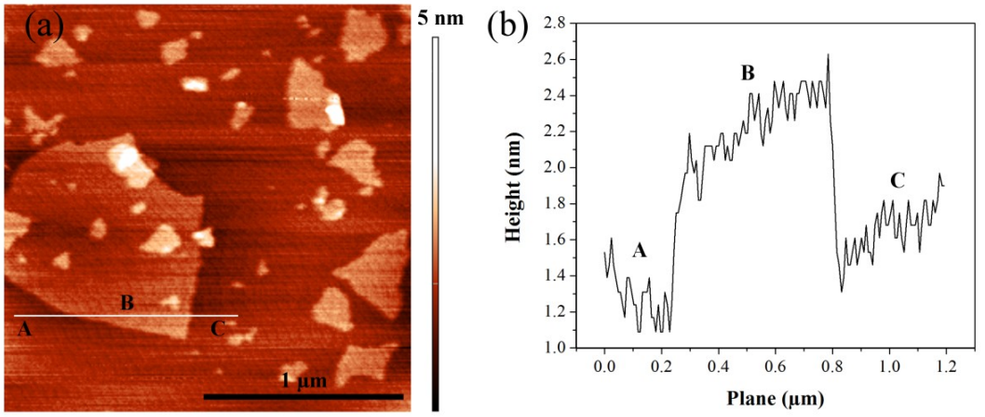

Figure 8.3: AFM picture in tapping mode of GO sprayed on mica substrate. a) Height image showing the GO platelets topography. b) topography profile along the white line.

Different GO solution mixtures are investigated in paragraph 7.3.5.1. A mixture of ethanol : DI water is chosen to spray GO because ethanol has an higher evaporation rate, so it evaporates quicker and prevents the particles from reaggregating. Furthermore, this prevents the dissolution of the PVA layers of the nanocomposites. Sprayed on mica, the GO platelets are mainly monolayers with a thickness of 1.6 nm as presented in Figure 8.3 and in accordance with the structure of GO [24]. Presented in paragraph 5.3.1, the range of diameters of the GO platelets is very wide from

50 nm to 2.0 µm. But in average for 100 particles, the diameter is 400 nm, giving an average aspect ratio of 300.

A solution of ethanol : DI water/GO is sprayed on mica sheet and presented in Figure 8.4 a and b.

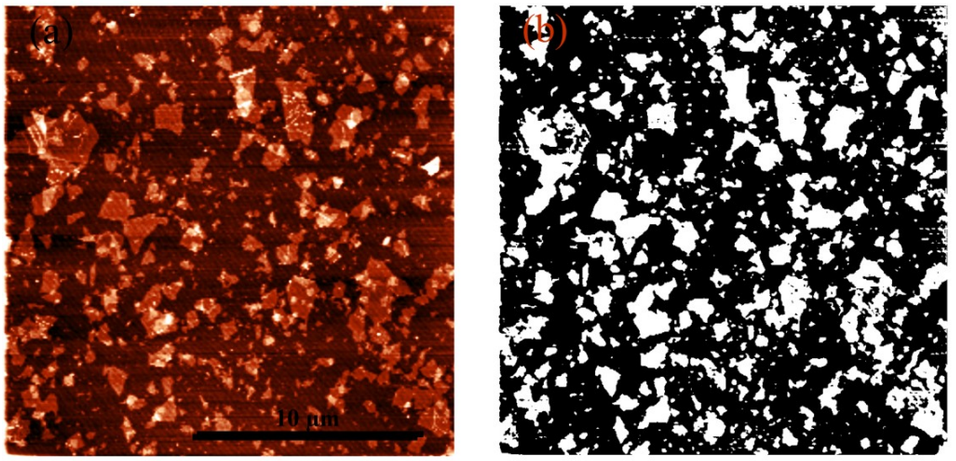

Figure 8.4: AFM pictures of a layer of GO sprayed on mica; (a) initial pictures; (b) threshold data manipulation.

The layer of GO is consisted in well dispersed GO flakes. The layer of GO is uniformed and covered the whole surface as seen in Figure 8.4 a. By adjusting the colour threshold, as shown in Figure 8.4 b, the surface covered by a layer of GO is estimated around 33 %. The thickness of the layer is measured and presented in Figure 8.5.

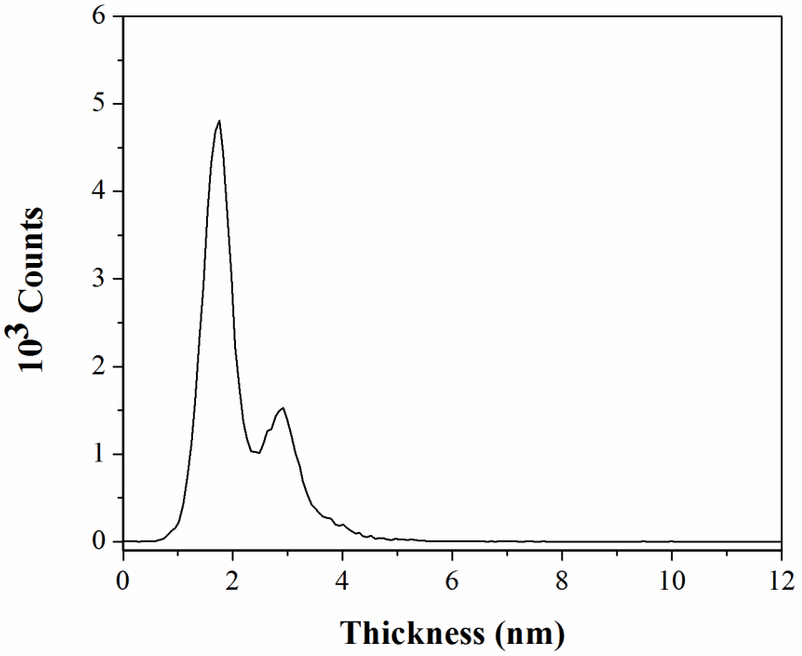

Figure 8.5: Histogram of sprayed GO thickness layer.

The histogram represents the thickness of GO of the deposited GO layer. On the histogram, two peaks are observed. The first peak is observed at 1.6 nm representing 69 % of the GO. The second peak, much smaller, is observed at 2.8 nm representing 31 %. Based on the study from Mkhoyan et al. [24] where the thickness of GO is measured about 1.6, 2.6 and 3.6 nm for a monolayer, bi and tri-layers, we assume that our deposition of GO is composed of ~ 69 % of monolayer and the rest of bi-layers or two monolayers lying on top of each other.

To spray a PVA layer, the polymer drops need to fully wet the surface to allow them to recombine and form a homogeneous layer. The surface of the sacrificial PS layer is plasma treated to create hydroxyl groups and make the surface more hydrophilic. The main challenge is to spray a uniform PVA layer without forming drops. Based on the work discussed in Chapter 7 paragraph 7.3.4, and following the condition

described in the experimental part, a uniform layer of PVA is obtained by spraying, see in Figure 8.6. The thickness of the layer is estimated by scratching the PVA layer onto the glass slide and is in the range of 10-15 nm, with a roughness about 1 nm.

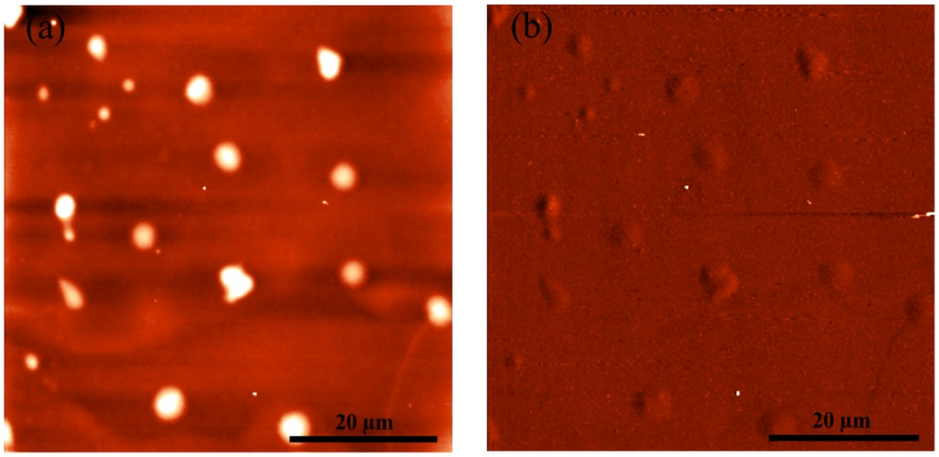

Figure 8.6: AFM picture of PVA layer after optimisation of spraying method on PS sacrificial layer a) height image of PVA layer, b) phase image. The round pattern on the pictures is due to the plasma treatment on PS.

Deposited on PVA layer, GO are well deposited and laid flat. Only high aspect ratio GO is subjected to a modification of their morphologies. By a simple calculation, the volume fraction of GO (φ_{GO}) in PVA matrix can be estimated with the equation 8.1:

$$\varphi_{GO} = \frac{vol_{GO} \times 100}{(vol_{GO} + vol_{PVA})} \qquad 8.2$$

With the volume of PVA and GO based on 1 nm^2. Since the GO covered only 40 % of the layer, the volume of GO is 40 % of the layer thickness if the thickness of GO is 1.6 nm and the thickness of the PVA is 15 nm. The volume of the GO layer and PVA are estimated at 0.68 nm^3 and 15 nm^3 respectively. Based on the Equation 8.2 the volume fraction of GO is estimated at around 4.0 vol. %.

The uniformity of layer growth is followed by UV/Vis absorbance. The deposition of each PVA-GO bi-layer is monitored until 5 bi-layers. The absorbance increased proportional with each bi-layer deposition of PVA-GO and is presented in Figure 8.7. We therefore can conclude that a uniform deposition of PVA-GO layer is obtained by the current spraying method.

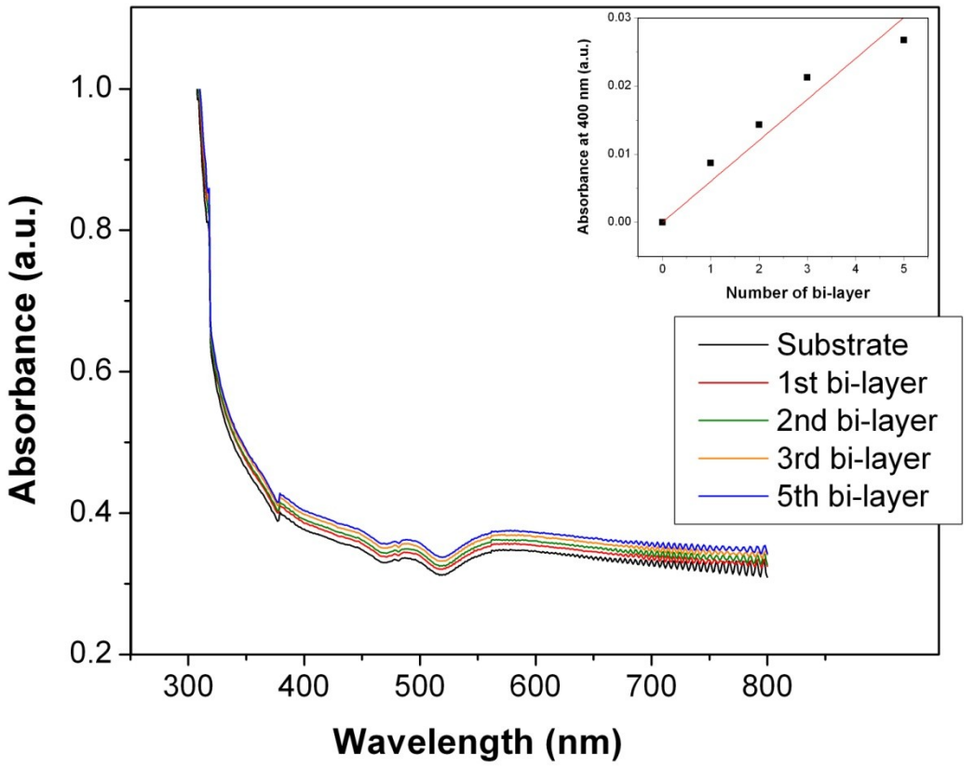

Figure 8.7: Absorbance at the light wavelength of $(PVA\text{-}GO)_n$ as a function of the number, n, of bi-layer after baseline correction. Inset graph shows the absorbance at 400 nm, chosen arbitrary.

The photograph in Figure 8.8 shows PVA-GO films of 25, 50, 75 and 100 bi-layers and reveals that the transparency of the LbL film is decreased as the PVA-GO bi-layer number is increased.

Figure 8.8: Photograph showing the transparency at 25, 50, 75, 100 bi-layers (from left to right).

PVA-GO nanocomposites consisting in 150 bi-layers are built-up. Scanning electron microscopy characterisation provides an average thickness of the film of around ~1.8 µm ± 0.2. Also, as seen in Figure 8.9, the cross section of the PVA-GO films shows clearly a layered structure.

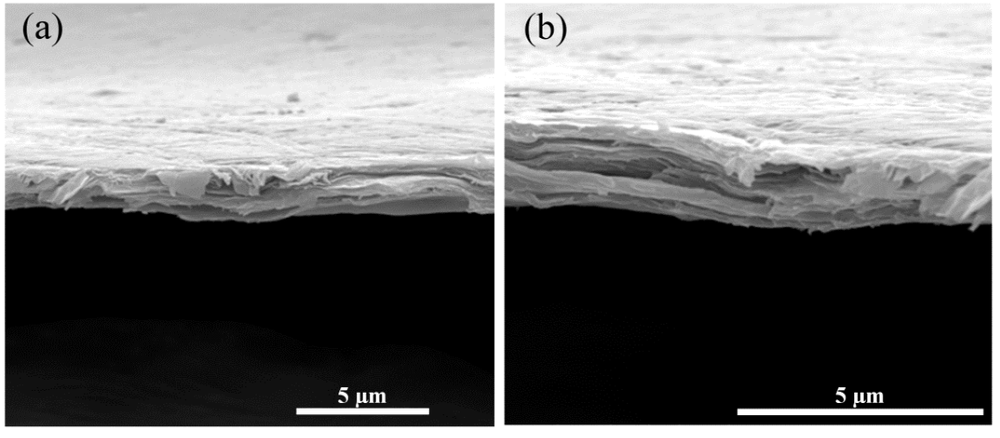

Figure 8.9: SEM characterisation of 200 bi-layers of PVA-GO nanocomposite free standing film. a) cross-section of the film. b) closer view showing the lamellar structure.

To measure the GO loading in our nanocomposite, TGA is used. At 600°C, the loading of GO in the nanocomposite is ~3.7 wt.%. However, as previously reported by Tiannan et al. [25], GO is thermally unstable and can undergo different mass loss when the temperature rises. In agreement with their TGA data, GO itself undergoes a loss of 45 wt.% at 600°C. From this the corrected percentage of GO in the LbL films corresponds to a loading of 5.4 wt.%.

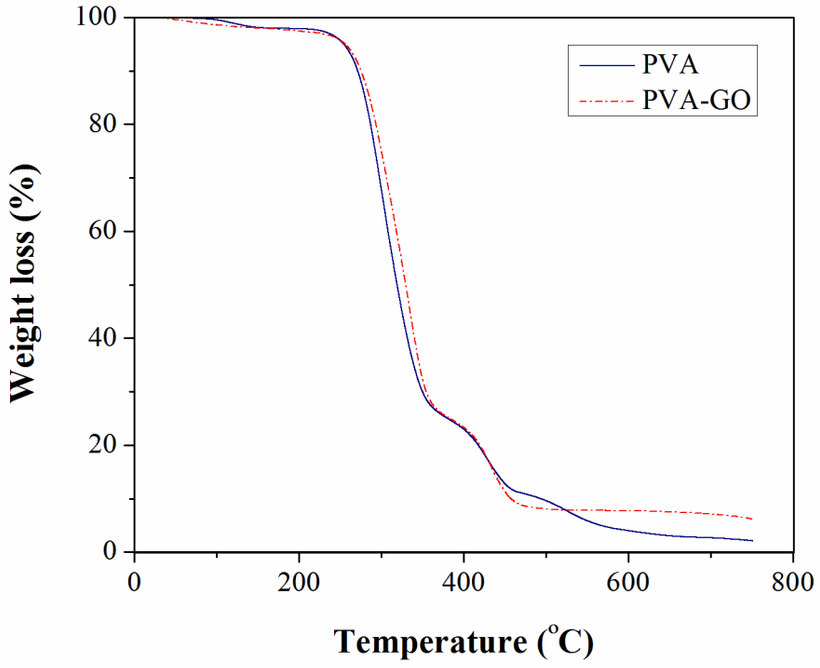

Figure 8.10: Degradation of LbL PVA film (solid line) and the LbL PVA-GO nanocomposite (dash line) in function of the temperature.

In order to compare with the previous rapid estimation, the volume fraction (φ_{GO}) is calculated as following the equation 4.2 where the density of the PVA and the GO are 1.3 g.cm^{-3} and 2.2 g.cm^{-3}, respectively. Based on the TGA results the nanocomposite at 5.4 wt.% of GO consists of a nanocomposite of 3.3 vol%.

8.3.2 Characterization of the traditional solution cast nanocomposites

To study the potential benefit of a hierarchical nanocomposite where the filler is well organised in the polymer matrix. A traditional solution cast PVA-GO is studied. The solution-cast PVA–GO nanocomposites are produced with the same GO loading than for the LbL nanocomposites, i.e. 5.4 wt.%.

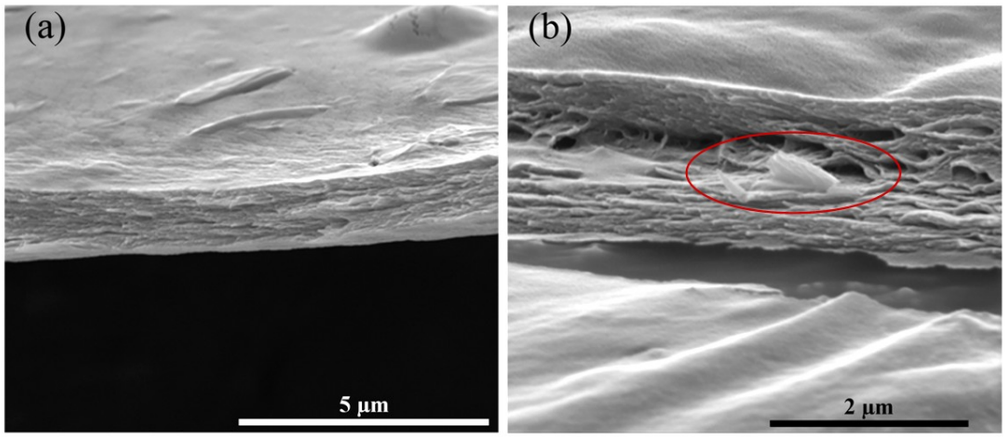

Figure 8.11: SEM picture of 5.4 wt.% cast PVA-GO at low magnification (a) and at higher magnification (b) where a red circle indicates GO agglomerate.

The scanning electron micrograph of a cast PVA-GO at 5.4 wt.%, presented in Figure 8.11 a, shows an orientated nanocomposite. The alignment of the GO along the film thickness is already reported in the literature [18, 26].

However, despite the very good dispersion of the GO in the matrix, traditional casting method did not prevent agglomerate formation as seen in Figure 8.11 b. The reagglomeration of the nanoparticles is well known especially at high loading and is associated to a restacking of the filler due to the van der Waals forces during slow drying process [27].

8.3.3 Characterization of LbL nanocomposite properties compared to cast nanocomposites.

8.3.3.1 Thermal properties

The thermal properties of the LbL nanocomposites are first studied by DSC. As discussed in paragraph 5.3.3, PVA is very sensitive to thermal degradation so the conditions are defined to minimise the polymer thermal degradation. The melting behaviour of the nanocomposites is presented in Figure 8.12.

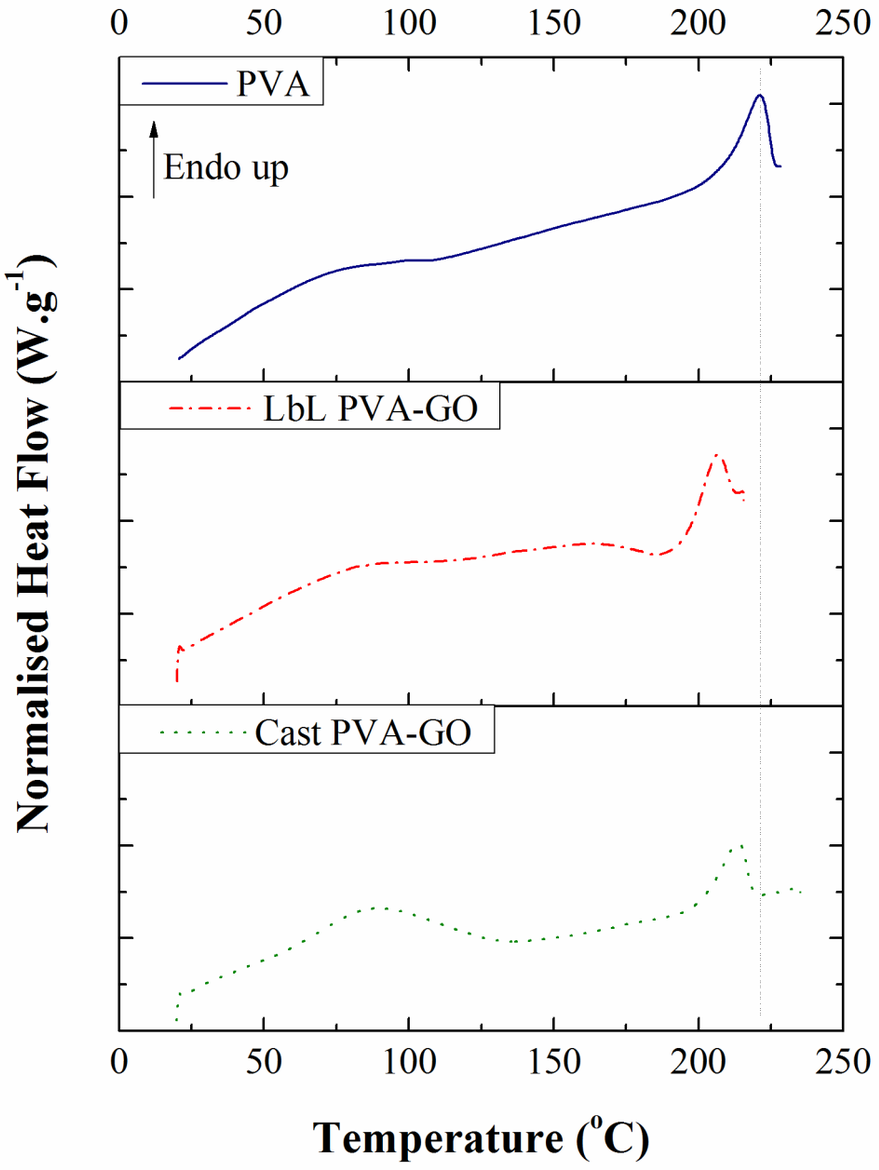

Figure 8.12: First heating phase of pure PVA, LbL PVA-GO and Cast PVA-GO.

During the first heating, two endothermic peaks are observed. For all the samples, a first broad peak is observed from 50 °C to 150 °C which corresponds to the evaporation of water bonded to PVA [28]. Also a second peak is observed at higher temperature and represents the melting peak of the PVA crystals. In the case of GO nanocomposites, for both cast and LbL nanocomposites, the melting peak is shifted

to lower temperatures. In addition, for both, the area of the melting peak is smaller than for a pure PVA. All the data are summarised in Table 8.1. The LbL nanocomposite showed a reduction of the melting temperature of 14 °C. The cast nanocomposite also presented a reduction of the *Tm* but less than 10 °C. A shift of the melting peak to lower temperatures for LbL nanocomposites was previously observed for LbL nanocomposites in the literature [13, 29]. The reduction of the melting temperature is described by Zhou et al. [29] as a reduction of polymer mobility due to an increase of the confinement of the polymer chains but could also be attributed to a reduction of the crystal size [30].

The degree of crystallinity is estimated following Equation 5.1 where ΔH_0, the melt enthalpy of 100 % crystalline PVA corresponds to 138.6 $J.g^{-1}$ [31].

As observed in Table 8.1, the degree of crystallinity of the pure PVA (cast or LbL) is estimated around 40 % which is similar to our previous work on cast PVA-GO nanocomposites (see paragraph 5.3.3). Also, with the addition of GO, the degree of crystallinity was strongly reduced. For instance, for the LbL nanocomposites, the degree of crystallinity dropped to 25 % which represent a reduction of 67 %. A similar effect is also observed for the cast nanocomposites where the crystallinity dropped to 30 % i.e. a reduction of 43 %. The reduction of the degree of crystallinity with the addition of GO has also been reported in literature [18, 29, 32]. Here it is often attributed to the strong interaction between the PVA and the GO. Adsorbed on the GO surface, the polymer chains have a reduced mobility and inhibit the PVA crystallisation [29]. This inhibition is important when the loading is high or the chains are constraints [29].

Tg is also estimated with DSC, from the second heating, and summarised in Table 8.1. The addition of GO leads to a shift of the *Tg* to higher temperature. For instance, for the LbL nanocomposite and for the cast nanocomposite a shift in *Tg* is observed of 18 °C and 12 °C, respectively. This shift reflects the strongly reduced mobility of the polymer motion which is more pronounced for the LbL system.

Table 8.1: Summary of DSC measurements of PVA and PVA-GO nanocomposites, during the first heating (1) and the second heating (2). The glass transition temperature, are measured during the second heating. The melting temperatures, the melting enthalpy and the degree of crystallinity are measured during the first heating.

	Tg_2 (°C)	**Tm_1 (°C)**	**ΔQm_1 ($J.g^{-1}$)**	**X_1 (%)**
LbL PVA	74	220	57.48	41.5
LbL PVA – GO	92	206	34.45	24.9
Cast PVA	76	224	60.46	43.6
Cast PVA – GO	88	214	42.26	30.5

From the thermal properties, we can observe that either cast or LbL nanocomposites showed similar features; i.e. a reduction of the melting temperature, a reduction of the degree of crystallinity, an increase of the *Tg* and a reduction of the crystallisation temperature. However all these features are more pronounced for the LbL nanocomposites which supports the hypothesis that the PVA chains are more confined between the GO sheets in the LbL system than in the solution cast system [29].

8.3.3.2 Mechanical properties

The mechanical properties of the nanocomposites are studied by tensile testing and presented in Figure 8.13 and summarised in Table 8.2. PVA curves show a ductile behaviour with a strain at break of up to 19 %. The Young's modulus (E) is around 2.9 GPa and the yield stress is around 33 MPa which is consistent with literature [33].

With the addition of GO, both nanocomposites i.e. LbL and cast showed an increase of the mechanical properties. For instance, the Young's modulus of the LbL is nearly doubled, while the yield stress is improved by 90 %. However, due to the embrittlement effect, the strain at break is however significantly reduced. On the other hand, for the cast PVA-GO nanocomposites, the Young's modulus is increased by 37 % as the yield stress is doubled.

Both LbL and cast nanocomposites displayed good mechanical reinforcement as seen in Table 8.2 which is believed to be due to i) a good dispersion of the GO in the matrix, ii) a good stress transfer between the PVA and the GO.

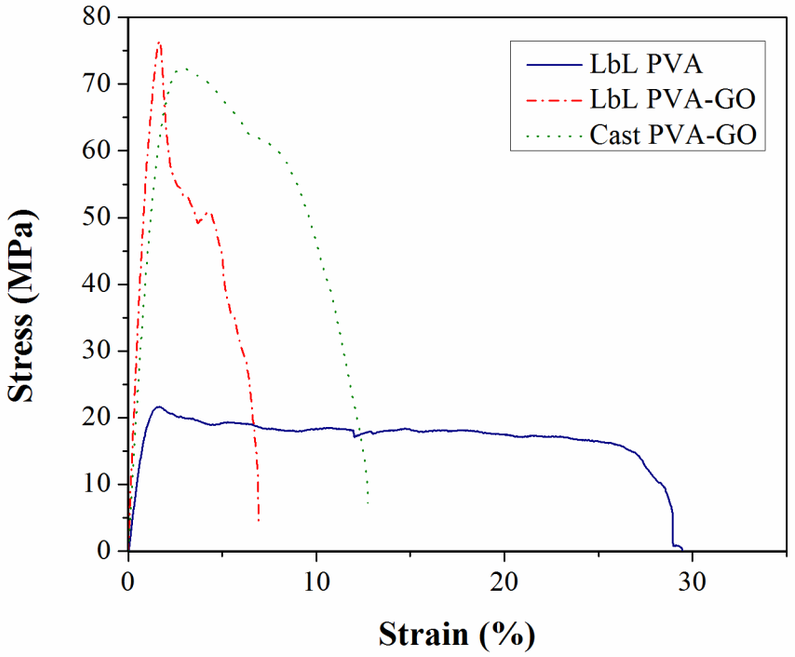

Figure 8.13: Strain-stress curves of 150 bi-layers GO nanocomposite (round) and 150 layer of PVA (diamond).

To complete this investigation the effective modulus of the graphene oxide in the nanocomposites is back-calculated using the Halpin-Tsai model [8] in accordance with [34]. The modulus contribution of GO in our nanocomposite is up to 120 GPa, which is below the intrinsic Young's modulus of GO at 207 GPa [35] but still at a good reinforcing efficiency level.

Table 8.2: Summary of mechanical properties of the LbL nanocomposites. The values are means ± standard deviation. The data are obtained on minimum 3 samples. The effective contribution of GO in the nanocomposite is back-calculated using Halpin-Tsai's model and noted as E_{GO}.

	E_{GO} ***(GPa)***	**E** ***(GPa)***	**Yield stress** ***(MPa)***	**Strain** ***(%)***
PVA	-	2.9 ± 0.7	33 ± 13	19 ± 9
LbL PVA-GO (5.4 wt.%)	120	5.9 ± 0.8	62 ± 17	8 ± 2
Cast PVA-GO (5.4 wt.%)	51	4.0 ± 0.4	67 ± 6	12 ± 2

To compare our layer by layer PVA-GO nanocomposite with the cast PVA-GO and the graphene based nanocomposite from the literature [10, 25, 33, 36-42] , the contribution of the graphene is plotted in function of the loading. All contributions are back-calculated using the Halpin-Tsai theory [8, 34], considering an aligned state, as presented in Figure 8.14. The blue broad band corresponds to the intrinsic modulus of reduced graphene oxide and graphene oxide, i.e. 250 GPa [43] and 207 [35] respectively. Therefore a blue guide line following the evolution of the contribution of graphene in function of the loading is plotted. As, it is discussed previously the contribution of the graphene decreases as the loading increases. In the case of the LbL PVA-GO, the contribution is doubled compared to the cast nanocomposite. The current reinforcement does not follow the trend described by the blue curve. An improved reinforcement is achieved by structuring GO in the

polymer matrix. In contrast, cast GO nanocomposite presents a lower effective modulus contribution which is nore in line with the trend described previously.

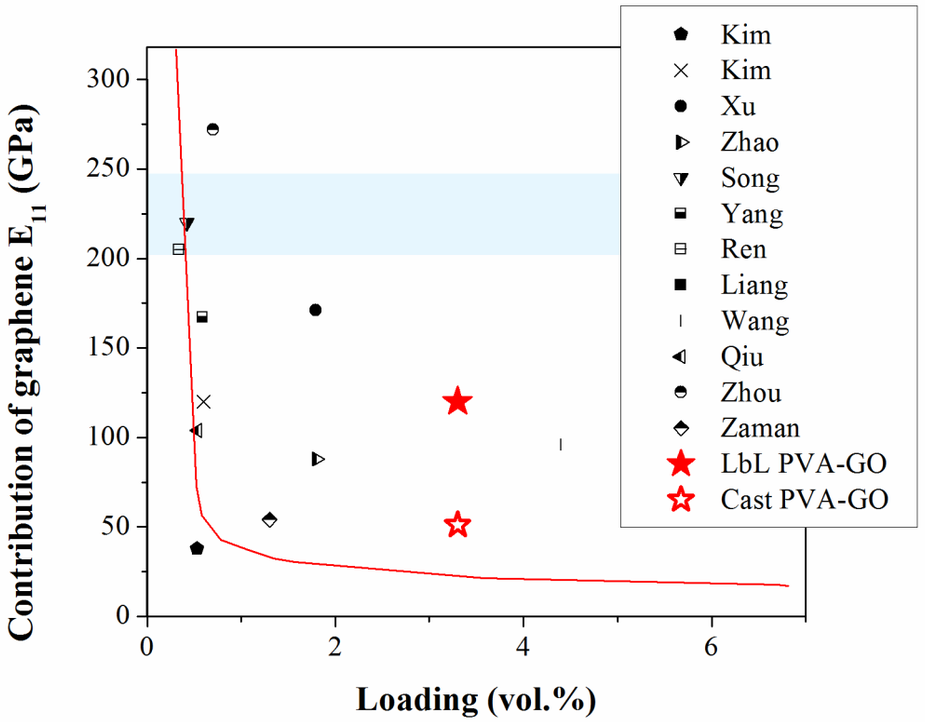

Figure 8.14: Evolution of the contribution of the graphene based nanocomposite in function of the loading. The full red star corresponds to the GO contribution in the LbL PVA-GO and the red hollow star corresponds to the GO contribution in the cast PVA-GO. The sparse red lines bar corresponds to the intrinsic modulus of reduced graphene oxide and graphene oxide and the blue solid line is guide line.

8.3.4 Conclusions

A hierarchical nanocomposite based on 150 bi-layers of PVA-GO is built-up by spraying method. Spraying is a new bottom-up approach allowing a good control of the structure of each individual layer on a bigger scale. The properties of the LbL nanocomposites are systematically compared to a traditional solution cast nanocomposites PVA-GO. The LbL PVA-GO nanocomposites showed a highly lamellar structure, consisting of ~5.4 wt.% GO. On the other hand the cast nanocomposites also presented a lamellar structure. The thermal properties are also investigated. For both methods, the addition of GO strongly reduced the degree of crystallisation, lowered the melting temperature and increased the glass transition temperature. However these effects are all more pronounced for the LbL nanocomposite system. The mechanical properties showed also a good reinforcement for both methods. In the LbL nanocomposites, the Young's modulus and tensile strength are doubled or nearly doubled. On the other hand, the Young's modulus in the solution cast system is improved by ~60 %. Indeed in both case, a good dispersion of the GO is obtained, with aligned particles and good stress transfer due to the strong interactions between the PVA and the GO. However, in the case of the LbL system, the GO contribution is more than double (120 GPa) the effective contribution for cast PVA-GO (51 GPa). The improvement in mechanical properties is believed to be due to the nanoscale organization in the sprayed nanocomposites which improve dispersion and allowed for a better stress transfer between the PVA and GO driven by hydrogen bonding. It also demonstrates the potential of hierarchical nanocomposites based on 2D nanofillers.

8.4. References

1. B. Ji and H. Gao, Journal of the Mechanics and Physics of Solids, 2004. **52**(9): p. 1963-1990.
2. P. Ciselli, Z. Wang, and T. Peijs, Materials Technology, 2007. **22**: p. 10-21.
3. M.A. Rafiee, J. Rafiee, Z. Wang, H. Song, Z.-Z. Yu, and N. Koratkar, ACS Nano, 2009. **3**(12): p. 3884-3890.
4. O.C. Compton, S. Kim, C. Pierre, J.M. Torkelson, and S.T. Nguyen, Advanced Materials, 2010. **22**(42): p. 4759-4763.
5. T. Ramanathan, A.A. Abdala, S. Stankovich, D.A. Dikin, M. Herrera-Alonso, R.D. Piner, D.H. Adamson, H.C. Schniepp, X. Chen, R.S. Ruoff, S.T. Nguyen, I.A. Aksay, R.K. Prud'homme, and L.C. Brinson, Nature Nanotechnology, 2008. **3**(6): p. 327-331.
6. K. Kalaitzidou, H. Fukushima, and L.T. Drzal, Carbon, 2007. **45**(7): p. 1446-1452.
7. XGSciences. http://www.xgsciences.com.
8. J.C. Halpin and J.L. Kardos, Polymer Engineering and Science, 1976. **16**(5): p. 344 - 352.
9. K. Kalaitzidou, H. Fukushima, and L.T. Drzal, Composites Part a-Applied Science and Manufacturing, 2007. **38**(7): p. 1675-1682.
10. K. Kalaitzidou, H. Fukushima, H. Miyagawa, and L.T. Drzal, Polymer Engineering & Science, 2007. **47**(11): p. 1796-1803.
11. Z. Wang, P. Ciselli, and T. Peijs, Nanotechnology, 2007. **18**(45).
12. H.D. Espinosa, T. Filleter, and M. Naraghi, Advanced Materials, 2012. **24**(21): p. 2805-2823.
13. P. Podsiadlo, A.K. Kaushik, E.M. Arruda, A.M. Waas, B.S. Shim, J. Xu, H. Nandivada, B.G. Pumplin, J. Lahann, A. Ramamoorthy, and N.A. Kotov, Science, 2007. **318**(5847): p. 80-83.
14. D. Chen, X. Wang, T. Liu, X. Wang, and J. Li, ACS Applied Materials & Interfaces, 2010. **2**(7): p. 2005-2011.
15. X. Zhao, Q. Zhang, Y. Hao, Y. Li, Y. Fang, and D. Chen, Macromolecules, 2010. **43**(22): p. 9411-9416.
16. K.W. Putz, O.C. Compton, M.J. Palmeri, S.T. Nguyen, and L.C. Brinson, Advanced Functional Materials, 2010. **20**(19): p. 3322-3329.
17. X. Wang, H. Bai, Z. Yao, A. Liu, and G. Shi, Journal of Materials Chemistry, 2010. **20**(41): p. 9032-9036.
18. Y.-Q. Li, T. Yu, T.-Y. Yang, L.-X. Zheng, and K. Liao, Advanced Materials, 2012. **24**(25): p. 3426-3431.
19. S. Deville, E. Saiz, R.K. Nalla, and A.P. Tomsia, Science, 2006. **311**(5760): p. 515-518.

20. E. Munch, M.E. Launey, D.H. Alsem, E. Saiz, A.P. Tomsia, and R.O. Ritchie, Science, 2008. **322**(5907): p. 1516-1520.

21. J.L. Vickery, A.J. Patil, and S. Mann, Advanced Materials, 2009. **21**(21): p. 2180-2184.

22. K.C. Krogman, J.L. Lowery, N.S. Zacharia, G.C. Rutledge, and P.T. Hammond, Nature Materials, 2009. **8**(6): p. 512-518.

23. W.S. Hummers and R.E. Offeman, Journal of the American Chemical Society, 1958. **80**(6): p. 1339-1339.

24. K.A. Mkhoyan, A.W. Contryman, J. Silcox, D.A. Stewart, G. Eda, C. Mattevi, S. Miller, and M. Chhowalla, Nano Letters, 2009. **9**(3): p. 1058-1063.

25. T. Zhou, F. Chen, K. Liu, H. Deng, Q. Zhang, J. Feng, and Q. Fu, Nanotechnology, 2011. **22**(4): p. 045704.

26. X. Yang, L. Li, S. Shang, and X.-m. Tao, Polymer, 2010. **51**(15): p. 3431-3435.

27. M. Moniruzzaman and K.I. Winey, Macromolecules, 2006. **39**(16): p. 5194-5205.

28. M.K. Cheung, K.P.Y. Wan, and P.H. Yu, Journal of Applied Polymer Science, 2002. **86**(5): p. 1253-1258.

29. J. Zhu, H. Zhang, and N.A. Kotov, ACS Nano, 2013. **7**(6): p. 4818-4829.

30. Y. Bin, M. Mine, A. Koganemaru, X. Jiang, and M. Matsuo, Polymer, 2006. **47**(4): p. 1308-1317.

31. N.A. Peppas and E.W. Merrill, Journal of Applied Polymer Science, 1976. **20**(6): p. 1457-1465.

32. Y.Y. Qi, Z.X. Tai, D.F. Sun, J.T. Chen, H.B. Ma, X.B. Yan, B. Liu, and Q.J. Xue, Journal of Applied Polymer Science, 2013. **127**(3): p. 1885-1894.

33. J.J. Liang, Y. Huang, L. Zhang, Y. Wang, Y.F. Ma, T.Y. Guo, and Y.S. Chen, Advanced Functional Materials, 2009. **19**(14): p. 2297-2302.

34. M. Van Es. 2001, Technology University Delft: Delft, The Netherlands.

35. J.W. Suk, R.D. Piner, J. An, and R.S. Ruoff, ACS Nano, 2010. **4**(11): p. 6557-6564.

36. H. Kim and C.W. Macosko, Polymer, 2009. **50**(15): p. 3797-3809.

37. H. Kim and C.W. Macosko, Macromolecules, 2008. **41**(9): p. 3317-3327.

38. X. Zhao, Q. Zhang, D. Chen, and P. Lu, Macromolecules, 2010. **43**(5): p. 2357-2363.

39. P. Song, Z. Cao, Y. Cai, L. Zhao, Z. Fang, and S. Fu, Polymer, 2011. **52**(18): p. 4001-4010.

40. P.-G. Ren, D.-X. Yan, T. Chen, B.-Q. Zeng, and Z.-M. Li, Journal of Applied Polymer Science, 2011. **121**(6): p. 3167-3174.

41. I. Zaman, T.T. Phan, H.-C. Kuan, Q. Meng, L.T. Bao La, L. Luong, O. Youssf, and J. Ma, Polymer, 2011. **52**(7): p. 1603-1611.

42. I.-H. Kim and Y.G. Jeong, Journal of Polymer Science Part B: Polymer Physics, 2010. **48**(8): p. 850-858.

43. C. Gómez-Navarro, M. Burghard, and K. Kern, Nano Letters, 2008. **8**(7): p. 2045-2049.

Chapter 9

Conclusion and future works

9.1. Conclusion

During the last decade graphene and its "relatives" have made major breakthrough in numerous fields like energy, transport, biomedical, nanocomposites, etc.. A real enthusiasm for 2D nanosheets is observed in academia as well as industry. More specifically for nanocomposites, 2D particles have some attractive features. Its dimensionality confers unique intrinsic properties but also provides some advantages like a higher contact surface with the polymer and/or an increase in tortuosity compared to 1D particles. These characteristics are important for mechanical reinforcement of nanocomposites as they can lead to better stress transfer, and may also lead to increased toughness of nanocomposites. In addition, 2D nanofillers are expected to improve thermal stability and barrier properties as this is strongly governed by a tortuosity mechanism.

In this thesis, graphite nanoplatelets and graphene oxide nanocomposites are studied for mechanical reinforcement. The nanocomposites are produced by either traditional or more

advanced processing techniques. The potential of reinforcement of the particles in polymeric matrix is addressed according to the effect of the processing on the particles (i) and the effect of the filler on the polymer morphology (ii).

Modification of the particles morphology with the processing

The processing can dramatically alter the 2D morphology of the particles. Polymer shearing as in extrusion compounding processes can for instance disrupt the 2D morphology. The ability for 2D particles to fold is linked to their flexibility. In another word, 2D particles with high aspect ratios are more "affected" than low aspect ratio particles since they are more flexible. A major risk during processing of graphene nanocomposites is to heavily fold or scroll the flakes and though this reduce their aspect ratio and to some extend lose their 2 dimensional characters.

Polycarbonate filled with graphite nanoplatelets was produced by melt mixing (Chapter 4). Like often described for melt mixed nanocomposites, melt compounded PC-GNP nanocomposites showed a relatively poor dispersion with particles randomly distributed throughout the matrix. The GNP observed in the matrix by electron microscopy were thick, about 50 nm. However, particles morphology was highly sensitive to shear mixing and particles were heavily folded. Solution cast PVA-GO nanocomposites showed a random orientation of the GO in the matrix (Chapter 5). The GO was well dispersed in the matrix and no folding or buckling of GO was observed. However, folded flakes were often observed for high aspect ratio particles, while low aspect ratio particles showed little folding. Spraying as a process to deposit a mono-layer of GO was studied (Chapter 7). Folded but also heavily wrinkled GO sheets were observed with high aspect ratio particles being the most affected. Interestingly, it was observed that the surface chemistry of the substrates also affected the GO morphology, with GO nanosheets showing more folds on PMMA surfaces than on PVA.

Polymer modifications with the addition of graphene like nanoparticles

Polymer modifications are common in nanocomposites. Polymer modification can take different forms including orientation, rigidification and/or extension of the polymer chains. But also, size, shape and orientation of the crystals, the form of the crystalline phase as well as a change in the degree of crystallinity, can all be observed after the addition of nanoparticles to semi-crystalline polymers.

The addition of GNP in the amorphous PC did not significantly modify the polymer (Chapter 4). The glass transition of the nanocomposites was found to be similar to that of the pure PC. The polymer did not coat the particles indicating a poor interaction between the PC and the GNP. On the other hand, GO was found to drastically modify the PVA morphology. Solution casting of GO nanocomposites showed a very strong interaction with the PVA, which is related to strong H-bonding between PVA and GO (Chapter 5). The strong interaction between the polymer and the GO leads to a rigidification of the amorphous chains. On the other hand, the addition of GO inhibit the crystallisation which leads to a reduction of the degree of crystallinity. In addition, the relaxation of the crystalline phase is lowered compared to pure PVA indicating a poor interaction between the GO and the crystalline phase. On the other hand, polymer morphology after uni-axial drawing showed similar features between the pure and nanocomposites (Chapter 6). The drawing lead to the orientation of crystals along the drawing direction. Also an increase of the crystalline domains was observed which is related to stress-induced crystallisation. The glass transition is also improved. However, the addition of GO in uni-axially drawn nanocomposites did not modify the morphology of the drawn PVA. The morphology of the PVA chains is thus governed by the drawing process and not by the addition of GO. Finally, in the layer-by-layer systems (Chapter 8), the addition of GO dramatically modified the morphology of the PVA.

With the addition of GO, the glass transition temperature increased, while a reduction of the degree of crystallinity was observed. Also a reduction of the melting temperature was observed. These features were all more pronounced for the LbL nanocomposites compared to solution cast systems indicating that the polymer chains are more confined in the LbL system.

Potential of reinforcement of graphene like particles

The potential to mechanically reinforce nanocomposites using graphene is investigating for traditional processing as well as more advanced processing methods. In order to illustrate the potential of reinforcement, the contribution of the nanoparticles to the nanocomposite property was back-calculated using the Halpin-Tsai's model and experimental data.

Melt mixing of PC-GNP nanocomposites showed a very weak mechanical reinforcing efficiency (Chapter 4). The poor reinforcement is mainly associated to poor dispersion, poor interaction between the polymer and the nanofiller, and the random distribution of the nanoparticles. In addition, folded flakes were observed in the polymer matrix. In solution cast systems, however, the addition of GO in a PVA matrix lead to a dramatic increase of the mechanical properties. However this reinforcement was not solely the result of filler reinforcement but was also due to a strong modification of the polymer matrix as a result of the strong interaction between PVA and GO, and an immobilization of the amorphous phase (Chapter 5). After uniaxial drawing (Chapter 6), the polymer modification of the neat polymer and nanocomposites was similar. A good mechanical reinforcement was obtained which originates from the well dispersed and aligned GO sheets. Finally, the mechanical reinforcement of LbL nanocomposites was studied in Chapter 8. Here, a very good mechanical reinforcement was achieved at a loading of 5.4 wt. %. However, also here the addition of GO strongly modified the polymer morphology, i.e. a reduction in crystallinity was observed as well as an strong immobilization of the amorphous phase.

Finally it seems that in order to fully exploit the potential of graphene for the reinforcement of nanocomposites the following points needs to be addressed:

- A good dispersion of the nanofiller to avoid agglomerates which weakens the nanocomposites. The dispersion of the filler is strongly related to the processing history, with melt mixing leading to a relatively poor dispersion compared to solution mixed systems. Nanofiller dispersion is also strongly affected by polymer chemistry, with good interactions between polymer and filler leading to better dispersions.
- High aspect ratio particles are preferred to reinforce nanocomposite. Based on mechanical models, an increase of their aspect ratio leads to better mechanical properties.
- Orientation of the filler is necessary to fully reinforce the polymer matrix.
- Good stress transfer between the polymer and the particles is fundamental for mechanical reinforcement. A good level of stress-transfer is obtained if there is a good interaction between the particle and polymer. Chemical functionalisation can improve the stress transfer as in the case of oxidation of graphene for instance. However, oxidation also leads to a weakening of the nanosheets themselves and a reduced intrinsic graphene Young's modulus. A compromise may be more suitable, probably through the use of reduced graphene oxide.

And more specifically for 2D graphene-like particles:

- The number of layers constituting the graphene like particles is important because the intrinsic modulus of multilayer graphene is related to the number of layers, and decreases as the number of layers increases.
- Control of the platelets morphology is crucial to reinforce nanocomposites. The processing method can greatly modify the morphology. Indeed, processes such as

melt mixing where nanoparticles are subjected to shear forces can lead to heavily folded flakes. Low aspect ratio nanoparticles, on the other hand, are less sensitive for folding as they are less flexible. However, as described previously, low aspect ratio particles are also less effective to reinforce nanocomposites.

9.2. Future works

The importance of controlling the morphology of graphene has been demonstrated throughout this thesis. In this regards, processes that allow for controlling the organization of polymers with well defined hierarchy have a real potential for future development of graphene nanocomposites. Although extensive work has been demonstrated at lab scale, today's challenge is to be able to transfer or adapt the hierarchical composite's approach to industrial scale production. Processing routes such as film blowing, biaxial drawing or multiple layer co-extrusion are promising to address this challenge. For instance is has been shown that the biaxial orientation taking place during film blowing is able to induce 2D orientation of clay nanoplatelets in a LDPE matrix [1]. The morphology resulting from this process showed significant improvement in barrier properties to oxygen due to the 2D organisation of the 2D nanofiller.

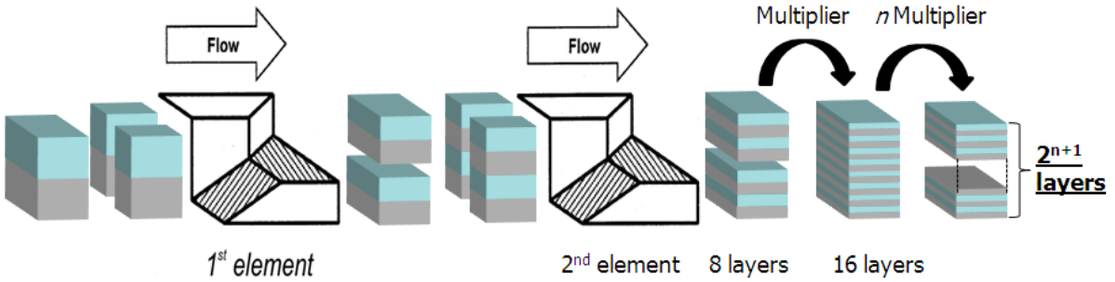

Figure 9.1: Schematic representation of the multiple layer co-extrusion process (adapted from [2]).

Multi-layer extrusion processes such as multiflux or multiplier technologies (Figure 9.1) have also a huge potential in the field of structured nanocomposites. In this process, a bilayer (or trilayer) polymer melt goes through a series of cutting, stretching and folding operations, resulting in a layered morphology of an extruded film [3]. The number of layers can range from 2 up to thousands, with individual layer thicknesses as low as 10 nm [2, 4]. We have demonstrated that this process could be used to localize graphene nanoplatelets in a composite film. In these initial experiments, we have produced films consisting of 64 alternating layers of high density polyethylene (HDPE) filled with graphene nanoplatelets and unfilled low density polyethylene (LDPE). DSC results (Figure 9.2a) confirm that the polymers are not miscible and after extrusion there is a clear distinction between the two phases (Figure 9.2b).

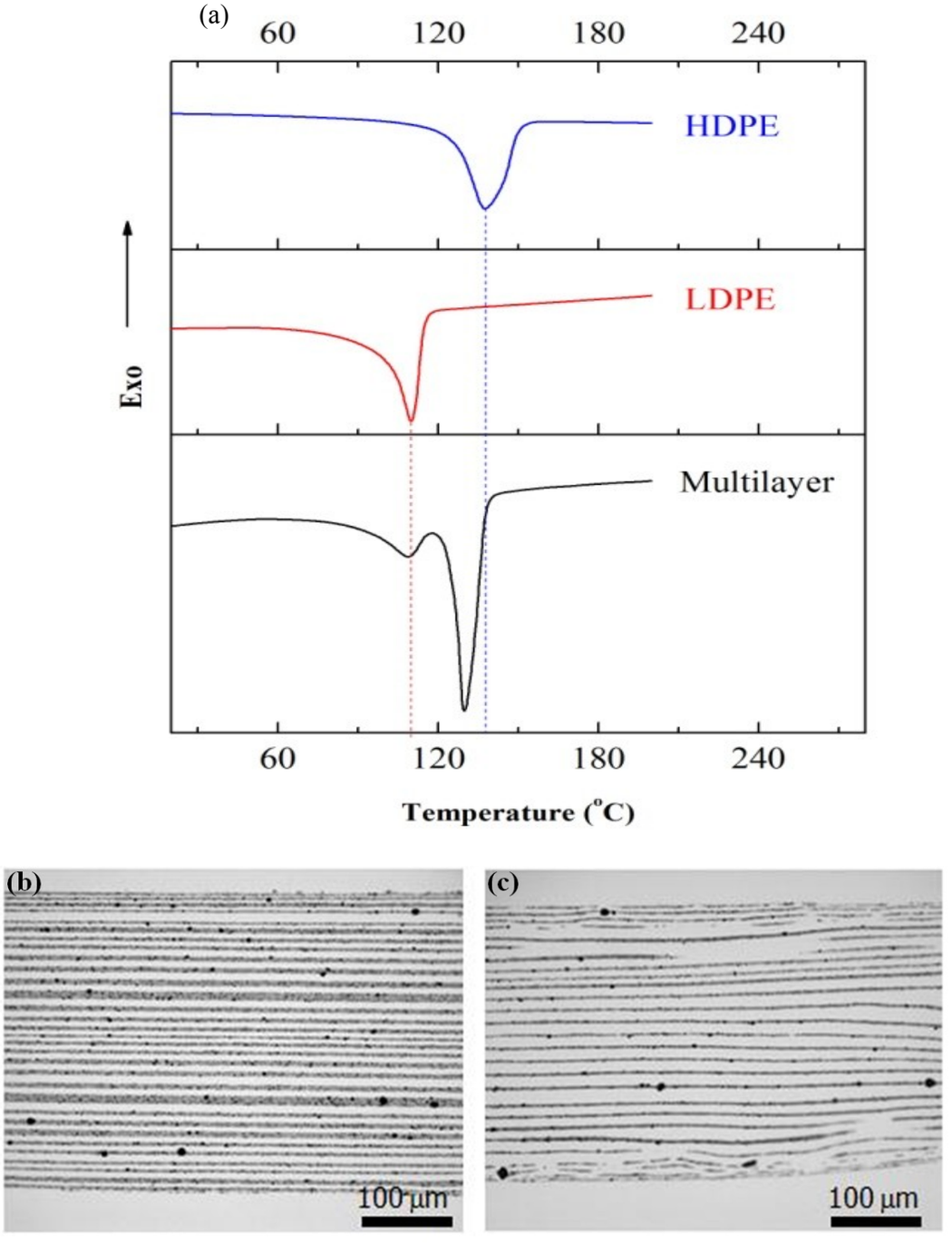

Figure 9.2: a) DSC diagram of the virgin polymer and the multilayer film b) optical microscopy image of the composite film's cross-section with 64 layers. The dark lines are the HDPE-graphene phase c) optical microscope image of the composite film's cross-section after 10 hrs annealing.

Annealing treatment is used to further alter this morphology. The films are annealed in the melt (T = 200 ^{o}C) for 10 hrs under nitrogen atmosphere. The resulting morphology is shown in Figure 9.2 c). Thin layers tend to break up while thicker layer are densified. The decrease in layer thickness is associated with a densification of the graphene rich phase. Such change in the local graphene concentration may increase the conductivity of the films similar to results reported for zinc particles in a similar multilayer extrusion process [5]. Here the loading is only 1 wt.% while percolation is usually reached for 20 to 30 wt.% in HDPE [6]. Therefore in our case, annealing had little effect on electrical conductivity.

Recently, freeze casting was also developed as a method to create highly organised nanocomposites [7, 8] (see also Chapter 3.5). For instance, freeze casting of pure GO results in a porous material with a "honey comb" microstructure due to the growth of the ice crystals, as seen in Figure 9.1.

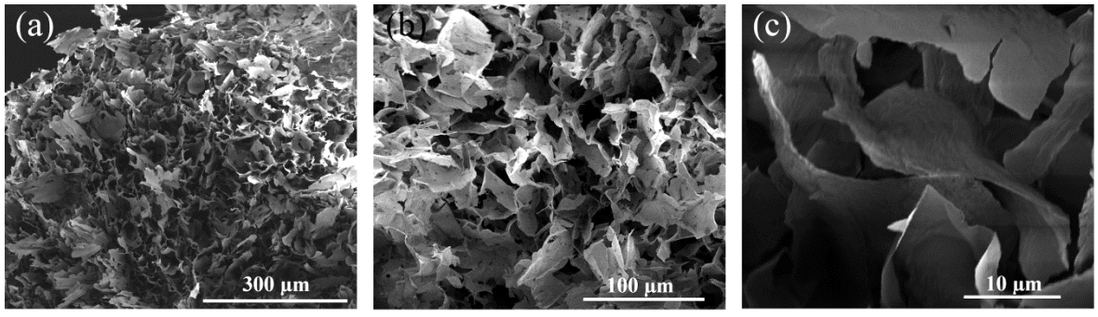

Figure 9.1: Cross section of freeze cast GO foam at different magnification. a) porous material, b) closer view, c) zoom on a wall made of GO particle.

As the ice crystal growth, the GO particles are expelled from the ice to create a porous GO foam after removing the water. The GO foam obtained presents a well organised structure with many holes along its cross section. The walls are made of GO particles with a thickness of 40 nm. This thechnique can lead to well organised nanocomposite after they are impregnated with a liquid polymer resin, with the potential of high GO loadings.

The most studied hierarchical nanocomposite in the literature is probably the layer-by-layer dip-coating process [9-11]. However, this method has limitations for large scale production of nanocomposites. In addition, a step to rinse the LbL is necessary for each layer deposited which implies long processing times and the use of extra water. In this regard, the LbL spraying method appears to have better potential for industrial applications since there is no extra step between the depositions of the layer. Moreover, the process can be adapted to any polymer and filler on any substrate, while spraying technology is already well known in the coating industry and can be relatively easily automated.

The developed spraying method has demonstrated great potential to deposit graphene and polymeric layers with a good control, while the LbL nanocomposites showed good mechanical reinforcement. In the current study, the LbL nanocomposites are composed of only 5.4 wt.% of GO. As previously discussed, increasing the GO loading would lead to a linear increase in the stiffness of the nanocomposites. In order to increase the loading, two options could be investigated: (1) to increase the thickness of the GO layers or (2) to the decrease the polymeric layer thickness. Decreasing the polymeric layer thickness can be achieved by absorbing the polymer chains onto the substrate using polyelectrolyte polymers or by using a polymer with lower molecular weight. In addition, since functionalisation strongly reduces the stiffness of graphene, LbL nanocomposites could be developed based on graphene instead of GO.

Industrial processes of nanocomposites are usually injection moulding and extrusion, which both involve polymer melt mixing. In this thesis, we observed that even thick GNP particles are folded after melt mixing. The need of post-processing that leads to improved levels of nanofiller organisation is necessary. Orientation of GO is possible after uni-axial stretching; however in order to fully align 2D graphene-like particles, bi-axial stretching is needed. In

addition, studies on clays nanocomposites showed that bi-axial stretching could also exfoliated these particles [12-14]. Finally, other industrial methods could be studied where 2D particles are oriented and exfoliated like the aforementioned multilayer extrusion process, calandering or 3 rolls milling.

9.3. References

1. J. Golebiewski, A. Rozanski, J. Dzwonkowski, and A. Galeski, European Polymer Journal, 2008. **44**(2): p. 270-286.
2. R.Y.F. Liu, A.P. Ranade, H.P. Wang, T.E. Bernal-Lara, A. Hiltner, and E. Baer, Macromolecules, 2005. **38**(26): p. 10721-10727.
3. M. Ponting, A. Hiltner, and E. Baer, in *Layered Nanostructures - Polymers with Improved Properties*, G.H. Michler and S. Henning, Editors. 2010, Wiley-V C H Verlag Gmbh: Weinheim. p. 19-32.
4. R.Y.F. Liu, Y. Jin, A. Hiltner, and E. Baer, Macromolecular Rapid Communications, 2003. **24**(16): p. 943-948.
5. S. Nazarenko, M. Dennison, T. Schuman, E.V. Stepanov, A. Hiltner, and E. Baer, Journal of Applied Polymer Science, 1999. **73**(14): p. 2877-2885.
6. X. Jiang and L.T. Drzal, Journal of Applied Polymer Science, 2012. **124**(1): p. 525-535.
7. S. Deville, E. Saiz, R.K. Nalla, and A.P. Tomsia, Science, 2006. **311**(5760): p. 515-518.
8. E. Munch, M.E. Launey, D.H. Alsem, E. Saiz, A.P. Tomsia, and R.O. Ritchie, Science, 2008. **322**(5907): p. 1516-1520.
9. J. Shen, Y. Hu, C. Li, C. Qin, M. Shi, and M. Ye, Langmuir, 2009. **25**(11): p. 6122-6128.
10. X. Zhao, Q. Zhang, Y. Hao, Y. Li, Y. Fang, and D. Chen, Macromolecules, 2010. **43**(22): p. 9411-9416.
11. J. Zhu, H. Zhang, and N.A. Kotov, ACS Nano, 2013. **7**(6): p. 4818-4829.
12. R.S. Rajeev, E. Harkin-Jones, K. Soon, T. McNally, G. Menary, C.G. Armstrong, and P.J. Martin, European Polymer Journal, 2009. **45**(2): p. 332-340.
13. R. Abu-Zurayk, E. Harkin-Jones, T. McNally, G. Menary, P. Martin, and C. Armstrong, Composites Science and Technology, 2009. **69**(10): p. 1644-1652.
14. R. Abu-Zurayk, E. Harkin-Jones, T. McNally, G. Menary, P. Martin, C. Armstrong, and M. McAfee, Composites Science and Technology, 2010. **70**(9): p. 1353-1359.